SURFACE EFFECTS ON THE MECHANICAL PROPERTIES OF FCC METAL NANOWIRES

By

Changjiang Ji

Dissertation

Submitted to the Faculty of the

Graduate School of Vanderbilt University

in partial fulfillment of the requirements

for the degree of

DOCTOR OF PHILOSOPHY

in

Civil Engineering

August, 2007

Nashville, Tennessee

Approved:

Professor Harold Park

Professor Prodyot K. Basu

Professor Luoyu Roy Xu

Professor Clare McCabe

To my parents

ACKNOWLEDGEMENTS

This work would have never been accomplished without the help from various people I met at Vanderbilt. They have given me countless positive influence and advices on my work and personal life experience during the past few years.

Of them, I would first like to thank my academic advisor, Prof. Harold S. Park, for his continuous support, encouragement, and invaluable help throughout my graduate studies. His insight and enthusiasm have left me a deep understanding and appreciation of this interdisciplinary research subject on nanomaterials.

I would like to thank Prof. Prodyot K. Basu for various kinds of support since the start of my Vanderbilt experience. His easy-going manner and meticulous working style are things I respect and will try to emulate in the future. I would also like to acknowledge Prof. Luoyu Roy Xu and Prof. Clare M. McCabe, who have contributed to my knowledge of solid mechanics and MD simulations.

A special acknowledgment goes to all of my current and previous professors, who have enriched my academic knowledge, both in class and in one-on-one communication. I would like to thank all the graduate students in the CEE department, especially my current and previous office-mates, who had made my life at Vanderbilt easier and more interesting. The research has been financially supported by the grants from CEE department and Vanderbilt University Discovery grant, which I really appreciate.

Finally, I am very thankful to my parents for their love, patience, and encouragement. They have always been with me and been supportive whatever I pursue. I am very proud of them.

TABLE OF CONTENTS

LIST OF TABLES

LIST OF FIGURES

CHAPTER I

INTRODUCTION

Nanotechnology, which has attracted intense research activities in the past several decades, is an interdisciplinary subject, cutting across the disciplines of engineering, chemistry, material science, and physical/biological sciences. It is a science dealing with the creation of new structural materials, functional devices, and machines on the order of nanometers scale, ranging from 1 nm to 100 nm. Research in nanotechnology involve three basic topics: nanomaterial synthesis, physical properties characterization, devices design and assembly. Two manufacturing methods, bottom-up and top-down, are commonly used in nanotechnology. Bottom-up is the approach where nanodevices are made from basic building blocks, which in turn are made of individual atoms with chemical synthesis technologies. Thus the botton-up offers the manipulation accuracy of devices at atomic level. Top-down is the traditional workshop or microfabrication approach where devices are shaped into desired configuration by cutting, carving, and etching.

The fundamentals in nanotechnology are the synthesis and property characterization of nanomaterials, including carbon nanotubes, nanowires, quantum dots and nanoparticles. During the past two decades, nanomaterials have become an exciting and rapidly expanding research area and much of this excitement has arisen from the discovering of new physical phenomena, increased functionality, and high integration density associated with nanomaterials. Of the present nanostructures, metallic and semiconducting nanowires have shown great promise as building blocks in future nanoscale structures due to their novel mechanical, electrical and optical properties [9–13].

As is shown in Figure (1), nanowires have been purposed as suitable intercon-

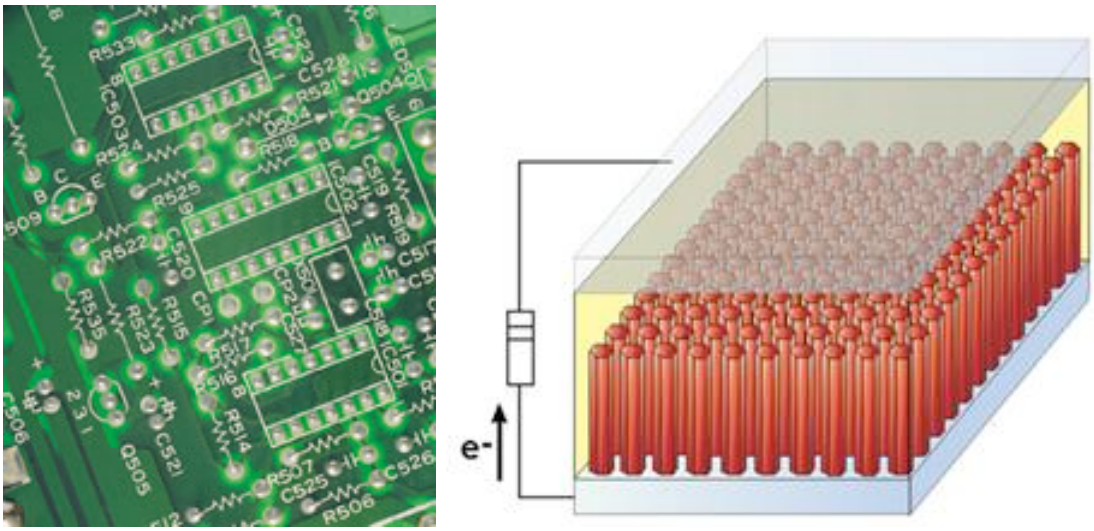

Figure 1: Examples to illustrate the possible applications of nanowires: Interconnects (left) and solar cells (right). Pictures are taken from [2, 3].

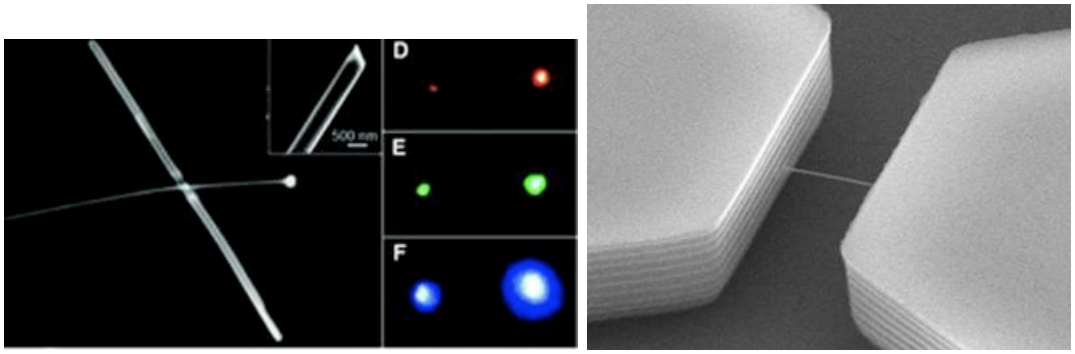

Figure 2: Examples to illustrate the possible applications of nanowires: Nanophotonics (left) and nanosensors (right) [2].

nects to assemble and integrate future electronic circuits [11, 14]. This technology is driven by the chip-manufacturing industries and is compatible with the current silicon technology used in microelectronics. Nanowires have been suggested to be used in solar cells, which are devices to convert optical energy into electrical energy. The introduction of nanowires to solar cells increases the rate of charge (electron) collection and thus improves the energy conversion efficiency of solar cells. Figure (2) has presented examples that nanowires can be used as nanophotonics [13, 15] and nanosensors [11,16]. The photonics is a science of generating, collecting and detecting photons. The smallness of nanowires offers the opportunity of manipulation and utilization of optical energy in integrated photonic nanodevices for communicating and sensing. For example, it has been demonstrated that metal nanowires are suitable for low-loss optical wave guiding and surface plasmon resonators, which might enable improved spatial resolution in plasmon-based photonic circuity. Due to the smallness of its mass and high stiffness, the nanowire has a very high natural frequency. So when biomolecules, such as virus or proteins, are attached to the nanowire, the mass will change dramatically and then will the frequency. Thus the nanowire can be used as a high resolution nanosensor in medicine.

Though nanowires have many attractive properties, this thesis will only focus on their mechanical properties. The interest in the mechanical properties arises from the following two facts: (1) Nanowires have exhibited superior mechanical properties compared to the corresponding bulk material, including high stiffness, large yield/fracture stress and strain, which are enabled by free surfaces at nanoscale; (2) The physical properties of nanowires are intricately coupled, i.e. electromechanical [17–19] and optomechanical [20–23], it is critical to understand the mechanical properties of deforming nanowires so that highly multifunctional NEMS can be designed.

These attractive properties of nanowires as compared to traditional bulk materials arise mainly from their structural size, which plays an important role in determining

the often superior physical properties in nanowires. At the nanoscale, the number of atoms on the surfaces is comparable to the number of bulk atoms, which leads to an substantial effect of surface atoms on material properties, known as surface stress effect. For example, the surface area to volume is 0.6 nm^{-1} for a cubic box with the edge length 10 nm; while the ratio is 0.006 nm^{-1} for the cubic box with the edge length 1000 nm. As the size goes larger, the ratio becomes even smaller, which represents a negligible effect of surface atoms. As is shown in Figure (3), a newly-formed nanowire which was created by cutting a system of atoms from the corresponding bulk material contracts in the axial direction while expanding in the lateral directions [24, 25]. The cross sectional edge length of the wire is around 2.5 nm and no applied force is involved in this contraction. The self-contraction behavior is negligible at macroscopic scale and is substantial at nanoscale, which is originated from the fact that the contraction is mainly driven by the surface stress that becomes critical only at nanoscale. Due to the surface stress and thus the self-contraction, the mechanical properties of nanomaterials are distinct from those of the corresponding bulk materials, including Young's modulus, yield stress, fracture strain, and resonance properties [26–28].

A fundamental understanding of the main surface property, surface energy / surface stress, can be traced back to the thermodynamics discussions on surfaces formulated by Gibbs [29]. According to this definition, surface energy, γ, is generally considered as the reversible work per unit area needed to create a new surface. The work, dW, required to create a new surface dA is

$$dW = \gamma dA \tag{1}$$

In the case of elastically stretched solids, another quantity, named surface stress, is commonly used. Surface stress is a second rank tensor, denoted as f_{ij}. It is defined as the work per unit area to elastically stretch a pre-existing solid surface and can be

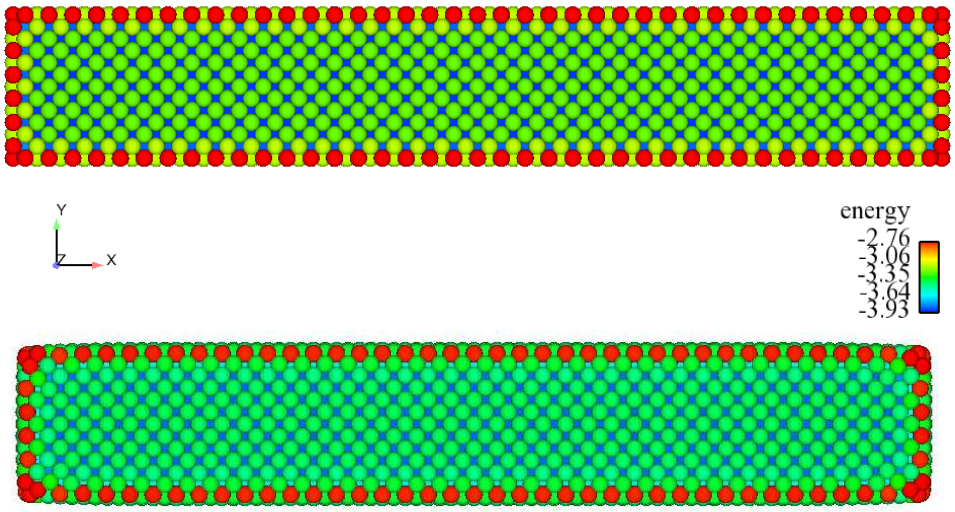

Figure 3: A schematic to illustrate the self-contraction with ⟨100⟩/{100} FCC gold nanowires. The contraction magnitude is 5%. The upper one is the newly-formed wire prior to contraction, while the lower one is the resulting wire after self-contraction.

related to surface energy as [4, 30, 31]

$$f_{ij} = \frac{1}{A}\frac{\partial(\gamma A)}{\partial \epsilon_{ij}} = \gamma\delta_{ij} + \partial\gamma/\partial\epsilon_{ij} \tag{2}$$

where ϵ_{ij} is the elastic strain of area A; δ_{ij} is Kronecker delta. Surface stress and surface energy have the same unit, representing the force per unit length. The relationship of surface stress and surface energy can be better represented in Figure (4), which gives two equivalent reversible paths of an elastically stretched solid. In this figure, γ is surface energy, A is surface area, and ϵ is elastic surface strain, $w1$, $w2$, $W1$, and $W2$ are the energies associated with the corresponding deformation process. From the figure, it can be found that $w2-w1$ equals to $W2-W1$, which are expressed as

$$w2 - w1 = 2\int A f_{ij} d\epsilon_{ij} \tag{3}$$

$$W2 - W1 = 2\gamma(\epsilon_{ij})A(\epsilon_{ij}) - \gamma_o A_o = 2\int d(\gamma A) \tag{4}$$

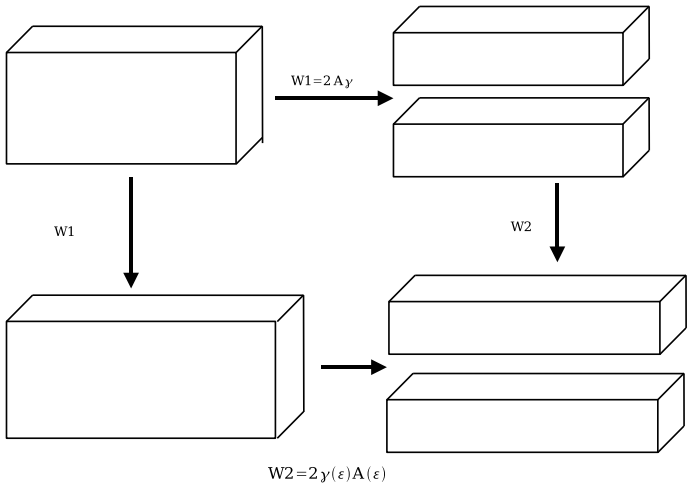

Figure 4: Schematic representation of two reversible paths to cut a stretched and unstretched solid, which illustrates the relationship between surface free energy and surface stress. This figure is taken from [4]

Thus,

$$Af_{ij}d\epsilon_{ij} = d(\gamma A) = \gamma A\delta_{ij}d\epsilon_{ij} + Ad\gamma \tag{5}$$

Then the equation (2) is derived.

The origin of surface stresses can be understood intuitively from the atomic scale perspective by considering the different local bonding environment of surface atoms and bulk atoms. Figure (5) displays a schematic of one 2-D {111} layer of face-centered-cubic (FCC) metal. A grey atom is taken to illustrate a surface atom and a green atom to represent a bulk atom. It can be seen from this figure that the number of nearest neighbors of the green atom, in this 2-D layer is six, and the nearest neighbor atoms are symmetric around the green atom; while for the grey atom, the number is only four and neighboring atoms are asymmetric. Thus, atoms at free surfaces, such as the grey atom, are not in equilibrium state due to the distinct bonding environment and will move and rearrange their relative atomic positions. This rearrangement maximizes the atom density at surfaces, lowers material surface energy, and causes

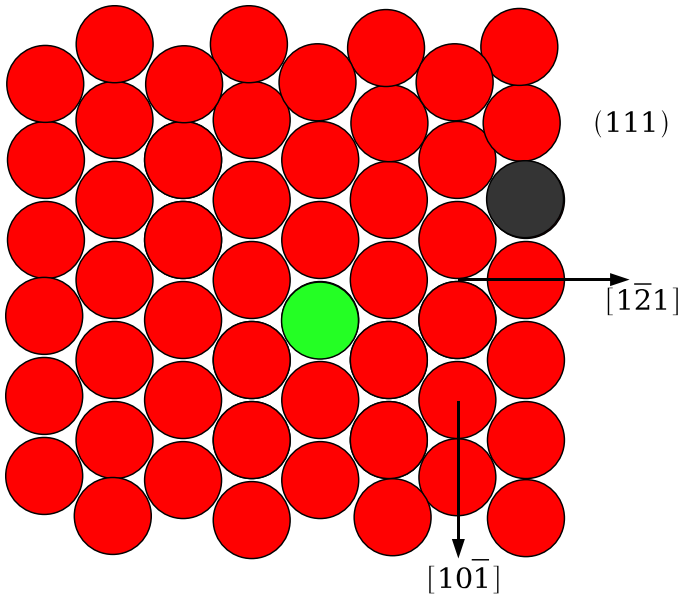

Figure 5: A schematic to illustrate the difference in bonding environment between surface atoms and bulk atoms. Note that only one single {111} layer in FCC crystals is taken for illustration. Real crystal are three dimensional structures.

the self-contraction as we mentioned previously. The rearrangement process can be treated as a result of surface effect induced by surface stress.

Additionally, the surface effect has a great influence on material mechanical properties, known as surface elasticity [5, 26]. Due to the different bonding environment of surface and bulk atoms, the elastic properties of surfaces differ from those of an idealized bulk material [5, 28]. This surface elasticity becomes magnified with the increase of surface to volume ratio, which can be achieved by decreasing the structural dimensions of materials. At the nanoscale, the surface elasticity becomes substantial. For example, mechanical resonance of a suspended silicon wires has exhibited a strong dependence on the wire surface to volume ratio and the resonant frequency becomes higher as the wire size goes smaller, which improves the sensitivity of the nanowire sensors [32]. The surface elasticity, or the size dependence of material mechanical properties, has been observed by many researchers [26, 27, 33–44], including elastic modulus [37, 39], yield stress [41], material ductile to brittle transition [42, 43], and

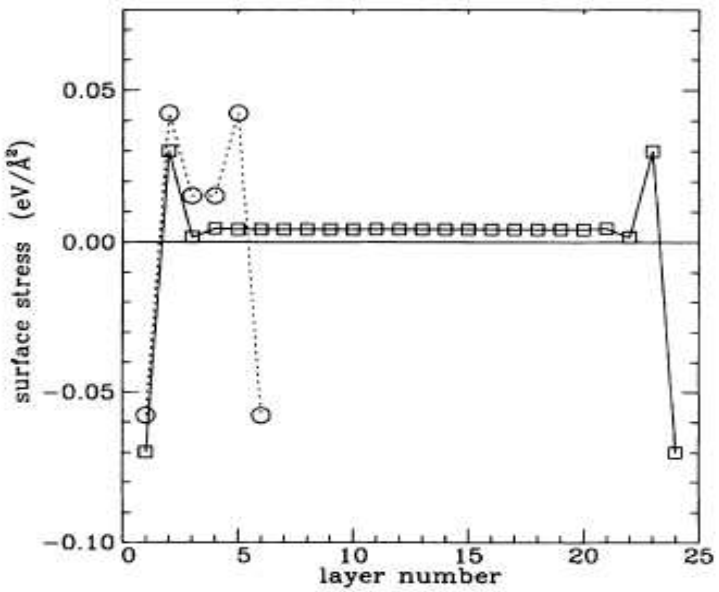

Figure 6: Surface stress as a function of layer number calculated using the method described by Ackland and Finnis. Note the six-layer sample has a substantially larger stress in the interior of the film. This figure is taken from [5].

the crystal nanoindentation [44].

The size dependence of material mechanical properties can be understood from the work by Mullins *et al.* [45]. According to their discussions, contributions to surface stress are not from the free surface layers only, but atomic layers near the free surfaces. Therefore the rearrangement of atoms should also appear several layers below free surfaces. Molecular dynamics (MD) simulations have revealed that for Al, Ni and their alloys, oscillatory surface relaxation decays exponentially into the bulk [46]. As shown in Figure (6), the free surface induced lattice distortion extends only about three layers of atoms into the bulk [5, 47]. So, it can be concluded that in bulk specimens, volume quantities dominate material properties over surface quantities and surface effects are neglected under most conditions.

The influence of surfaces on the size dependence property is easier to understand from the energy viewpoint. The total energy of a nanostructure, ϕ_T, comes from two

contributions, surface energy ϕ_S and bulk energy ϕ_B, and can be written as $\phi_T = \phi_S + \phi_B$. With the decrease of the structure size, the number of atoms in the bulk is decreasing more rapidly compared to the number of surface atoms, indicating an increase of in the area to volume ratio. So the weight or importance of ϕ_S as compared to the total energy ϕ_T is increasing with the decrease of specimen size. As specimen size enters into nanoscale, such as nanowires or nanofilms, the influence of free surfaces on material properties becomes substantial, leading to the rearrangement of interior atoms [48,49]. Thus due to surface effects, material properties become size-dependent and can be dramatically different at nanoscale.

In FCC metal nanowires, surface stresses play an important role in material properties. For example, driven purely by surface stresses, a $\langle 100 \rangle / \{100\}$ metal nanowire can reorient into a $\langle 110 \rangle$ wire with $\{111\}$ side surfaces if the cross sectional length of the wire is smaller than a critical value [50]. The reorientation compared to self-contraction is for even smaller nanowires. In this structural reorientation, the wire contracts in the longitudinal direction with a strain of -30% due to tensile surface stresses on the side surfaces of metal nanowires. After reorientation, nanowire surfaces have maximized bonding density and expose lower energy side surfaces, $\{111\}$. In the simulation of structural reorientation, the surface energy of gold on $\{111\}$ layers is 1.283 Jm^{-2}, and is 1.627 Jm^{-2} on $\{100\}$ surfaces [51]. It can be seen that the surface energy reduction is around 21% for the structural reorientation of gold nanowires. At the newly-formed configuration, atoms are arranged at current equillibrium positions and stresses, including the tensile surface stresses and intrinsic compressive stresses, balance each other. In the FCC metal nanowires, surface effects are substantial and responsible for various interesting phenomena, such as asymmetric yield strain [52], tetragonal phase transformation [25, 53] and surface reorientations [50, 54, 55].

The importance of free surfaces on the deformation behavior and mechanical properties of metal nanowires can be observed mainly from the two aspects: (1) it acts as

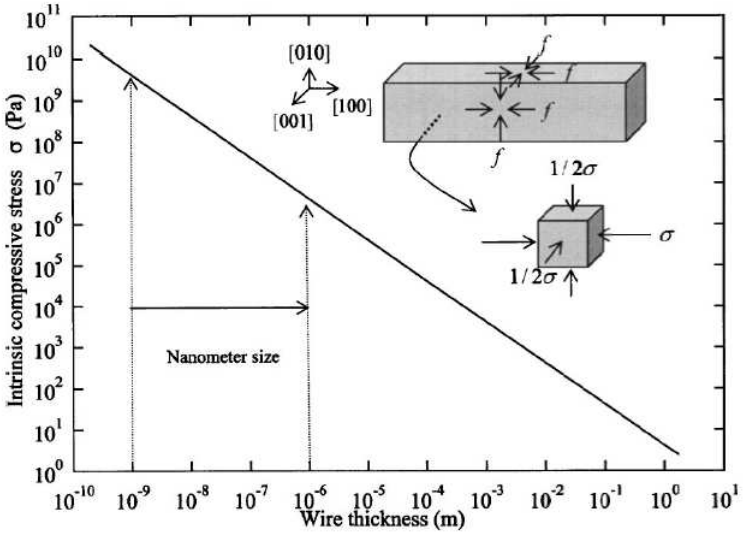

Figure 7: Tensile surface stresses, f, on the $\{100\}$ side surfaces of an fcc gold $\langle 100 \rangle$ wire and the magnitude of the intrinsic compressive stress, $|\sigma_f|$, in the wire as a function of wire thickness. This figure is taken from [6].

the defect nucleation sites due to the high energy of surface atoms; (2) tensile surface stresses existing on free surfaces induces substantial compressive intrinsic stresses inside the nanowire, which is responsible for asymmetry yield strain and stress, enhanced elastic properties, and many other interesting nanoscale behavior. Diao *et al.* [56] has provided approximate equations to evaluate the intrinsic compressive stress along the wire length direction. According to that formula, the magnitude of intrinsic stresses is correlated to the magnitude of surface stresses and the thickness of the nanowire. The intrinsic stress induced by stress effects is around zero at meter scale and can be on the order of MPa to GPa as the wire thickness shrinks to nanoscale. The variation of the magnitude of intrinsic stress as a function of wire thickness is illustrated in Figure (7).

This chapter will first present a literature review on the mechanical properties of nanowires and related interesting phenomena, followed by the motivation and an outline of this thesis.

I.1 Previous work illustrating the mechanical properties of nanowires

From a mechanical viewpoint, metal nanowires are of great interest because they can sustain extremely large stresses and strains, and because their electrical, thermal and optical properties are coupled to the mechanical deformations. For example, it has been demonstrated that the yield strength of nanowires increases with the decrease of wire cross section size, and the yield strength can be around 100 times larger than that of the corresponding bulk material [38]. Aside from the superior mechanical properties, coupled physics, including electrical-mechanical and optical-mechanical properties, has also been demonstrated by researchers [57, 58]. The coupled electrical-mechanical property has been purposed to be utilized in future nano electro mechanical systems (NEMS), where an external electric field is capable of inducing bending moment on freestanding nanowires. The deterioration of the nanowire optical properties has been correlated to its mechanical properties. The connection is rooted in the formation of cracks in nanowires, which simultaneously degrade the optical and mechanical properties of nanowires [57]. Besides, metal nanowires has shown many other exotic phenomena in the mechanical deformation, such as tensile loading induced atom-thick chain [59] and strain-rate induced amorphization [60].

The research work on the mechanical properties of nanowires thus far has mainly relied on atomistic simulations instead of on experiments. Due to the smallness of the nanowire structural size, the experimental requirements in handling, positioning, and gripping wires accurately are difficult to achieve, which leads to significant scatter in reported experimental mechanical properties [38, 61–64] and thus impedes the popularity of nanoscale experiments. Instead, due to the high accuracy, feasibility, and achievable computational cost, atomistic simulations are used widely in studying the mechanical properties of nanowires.

Using molecular dynamics simulations, two observations have been made by Mehrez *et al.* [59] : first, gold nanowires have exhibited the phenomenon of a single atom

chain at the neck area under tensile loading before breaking into two pieces; and second, conductance of nanowires is closely related to the morphology at the yield neck of nanowires. In that work, it was illustrated that conductance curves showed a staircase-like variation with loading steps on gold nanowires, which was attributed to the nucleation and interaction of defects in nanowires under tensile loading. A similar phenomenon has been observed in experiments in atom chains, showing the dependence of conductance on the wire structural variations [18, 65, 66]. To understand the tensile loading induced atom chain phenomenon, much effort has been devoted to analyzing its formation mechanism and stability through both experiments and atomistic simulations [67–74]. It has been demonstrated that this one atom chain phenomenon appears more frequently in nanowires with $\langle 111 \rangle$ and $\langle 100 \rangle$ orientations than $\langle 110 \rangle$ orientation [74], while $\langle 110 \rangle$ wires are prone to form stable nanobridges [73].

One interesting phenomenon observed is that nanowires exhibit a crystalline-to-amorphous structural change under extremely high loading rates, around 10^{10}s^{-1} [60]. With MD simulations, it has been illustrated that the crystalline structures of Ni and NiCu nanowires transform homogeneously into an amorphous state and there are no twins or dislocations in the subsequent loading process. Accordingly, amorphous nanowires exhibit fundamentally different stress-strain curves compared to crystalline materials and show an extremely high yield strength due to the avoidance of traditional crystalline defects, such as twins or dislocations. Similar phenomena on strain rate induced amorphizations in Ni nanowires have been observed by Branicio *et al.* [75].

Atomistic simulations of metal nanowires often focus on studying their fundamental deformation mechanisms. With a second-moment approximation of tight-binding (SMA-TB) potential, Kang *et al.* [76] simulated a $\langle 100 \rangle$ copper nanowire under tensile loading conditions. In that work, it was observed that the first yield point appeared at a strain of $\epsilon = 13.3\%$, and subsequent deformation alternated between quasi-elastic

and yielding stages. The first yield is due to an abrupt slip on {111} planes, while alternating elastic and yielding stages correspond to energy storing and atomic structure disordering period, respectively. This alternation process in stress-strain curves has also been observed in MD simulations by Mehrez *et al*. [59]. In addition, Kang *et al*. has revealed that the deformation of ⟨100⟩ copper nanowires is mainly attributed to two distinct slip mechanisms: the glide of a dislocation on {111} planes and the homogeneous slip of one plane over another. The crossover of the two slip events is responsible for a reduction of nanowire diameter, thus leading to necking. Discussions on metal nanowires under other mechanical loading forms, such as compression, torsion and shear, have been studied by researchers as well [52, 76, 77].

One interesting discovery concerning metal nanowires is that their mechanical properties are closely related to loading rates and cross-sectional sizes [69, 78–80]. Loading rate dependence is expressed with the magnitude of yield stresses and yield strains, which are distinct under different loading conditions. It is believed that metal nanowires exhibit largest strength under two conditions: one is with quasistatic loading and another one is with the loading rates above $10^{10}\mathrm{s}^{-1}$ [69]. The high strength, which appeared in quasistatic loading, is due to the fact that atoms can relax to their equilibrium positions after each loading increment, while the latter case is related to loading rate induced amorphization [60, 69]. Of the present accessible loading rates, $10^7 \sim 10^9 s^{-1}$, it is noticed that yield stresses and yield strains increase with the increase of loading rates, although the difference in magnitude is strong. The increase in the magnitude of yield strain indicates a strain rate hardening mechanism in nanowires. The dependence in yield stress is believed to be associated with phonon drag or dynamic wave effect [79], which inhibits the dislocation initiation or occurrence of slip in metal nanowires. The cases with even lower loading rates, below $10^6 s^{-1}$, are not readily available yet due to the confinement of current of computational power.

The dependence of the deformation behavior and mechanical property on the cross

sectional size has been documented by various researchers as well. For example, it has been found that if metal nanowires keep crystalline structure during the mechanical deformation, crystalline slip is the main deformation mechanism for wires with small cross sections; and cross slip is responsible for the plastic deformation of wires with relative large cross section area [79, 81]. This phenomenon is attributed to the enhanced opportunities for dislocation motion in the wire with a larger cross sectional size, which also explains the observed decrease in its magnitude of yield strain [69] and yield stress [38, 79, 82] with the increase of wire cross-section sizes. Besides the cross section size, the axial orientation does have a great influence on wire mechanical deformation mechanism and properties, and plenty of research work has been performed. Although most research on nanowires so far has been concentrated on $\langle 100 \rangle$ wires [60,67,69,72,75,76,79,83], deformation behavior of nanowires is crystallographic orientation related. For example, $\langle 110 \rangle$ wires can form long stable nanobridges under tensile loading, while $\langle 100 \rangle$ and $\langle 111 \rangle$ wires cannot [71,73,84]. Discussions concerning deformation mechanisms of wires with different orientations have been addressed by several researchers [74, 85].

Recently, an appealing feature has revealed that metal nanowires can show phase transformations and structural reorientations if their cross-section sizes are very small [6, 25, 50, 53, 86]. For example, gold nanowires can undergo a phase transformation from face-centered cubic (FCC) to body-centered tetragonal (BCT) when the cross sectional length of the wire is below about 2 nm [6, 25, 53]. This transformation process is driven purely by surface stresses and allows a reduction of the wire surface energy. This phenomenon is only possible at nanoscale and goes away at macroscopic scale because surface effects are size dependent and are substantial only at such small scale. Similar mechanisms apply to the observed structural reorientation, where a $\langle 100 \rangle$ wire can reorient into a $\langle 110 \rangle$ nanowire with $\{111\}$ side surfaces. Atomistic simulations have been performed to study this phenomenon by various researchers [6, 50, 85–89].

The energetic possiblities on the phase transformation and structural reorientation phenomena have been confirmed by recent calculations with density functional theory [90].

Of further interest, it has been revealed that these reoriented $\langle 110 \rangle / \{111\}$ nanowires can show shape memory and pseudoelastic behavior through reversible reorientations between $\langle 100 \rangle$ and $\langle 110 \rangle / \{111\}$ configurations [50, 87–89]. The pseudoelastic behavior has also been observed in NiAl nanowires, which is realized through martensitic phase transformation [91]. The ability to show the shape memory and self-healing behavior indicates that metal nanowires may fill a critical need as self-healing materials in next-generation nanodevices, as shape memory alloys (SMAs) do in today's applications. However, due to the novelty of nanowires, more fundamental research work needs to be carried out to understand their governing mechanisms and then to better utilize these shape memory effects in the future.

Recently, Park *et al.* [85] revealed that the mechanical deformation mechanism of metal nanowires depends not only on the wire axial orientation but also on the side surface facets. For example, a $\langle 100 \rangle / \{100\}$ nanowire exhibits twins in the post-yield period under compression, resulting in $\{111\}$ side surfaces; while a $\langle 100 \rangle / \{110\}$ wire under compression exhibits distributed stacking faults along the wire axial direction. Both types of wires are of the same, including the structural size and the axial orientation, except the side surface facets. This side surface impact is another phenomenon originated from surface effect and thus is only substantial at nanoscale. To gain a better understanding of the influence from side surfaces facets, fundamental research work has been performed to characterize the coupled effects of geometry and side surface orientation on the deformation behavior and mechanical properties of metal nanowires [81, 92, 93].

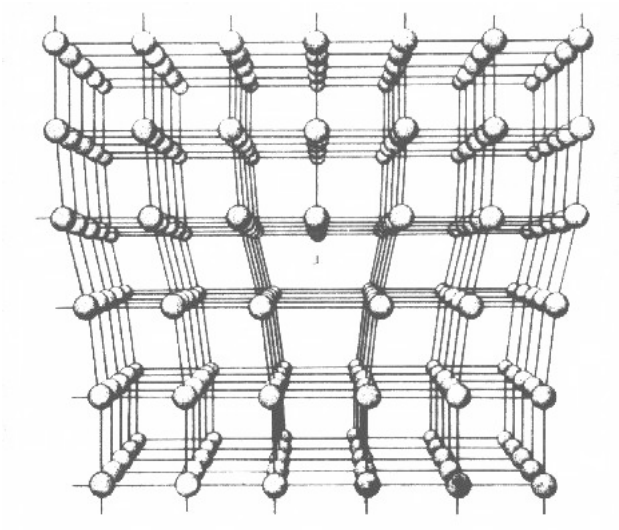

Figure 8: A perspective view of an edge dislocation. This figure is taken from [7].

I.2 A brief introduction to dislocations, stacking faults, and twins

The mechanical properties of FCC metal nanowires determined mainly by the material lattice defects, including dislocations, stacking faults, and twins. A brief introduction to these crystalline defects will be given in this section.

The concept of dislocations was first introduced by Orowan, Taylor and Polanyi [94] to explain the following two facts: (1). the stress required to plastically deform a crystal is much less than the theoretical shear strength of a perfect crystal; (2). strain hardening effect in crystals. Dislocation is a line defect, whose magnitude and moving direction are characterized with burgers vector. By making a loop around the dislocation core and going exactly the same in each direction, burgers vector is defined as the vector from the start atom to the end. When the dislocation line is parallel with burgers vector, it is a screw dislocation. When perpendicular, it is an edge dislocation. The commonly observed dislocations in crystals are in the format of curves, which are mixed dislocations. Figure (8) presents a schematic three-dimensional view of an edge dislocations in a cubic primitive lattice. Though the edge dislocation is a clear extra half plane in this Figure, dislocations in real crystals would look much

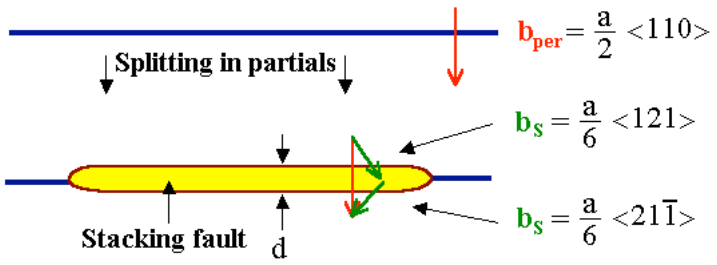

Figure 9: An illustration on the formation of stacking fault from partial dislocations $\frac{a}{6}\langle 121\rangle$ and $\frac{a}{6}\langle 21\bar{1}\rangle$, which in turn formed from a full dislocations $\frac{a}{2}\langle 110\rangle$. This figure is taken from [7].

more complicated.

A full dislocation has a higher energy and could be split into two partial dislocations reducing the total energy. The partial dislocations are associated with low-energy stacking faults and twin boundaries. For example, a full dislocation of $\frac{a}{2}[110]$ is formed by two partial dislocations, $\frac{a}{6}[121]$ and $\frac{a}{6}[21\bar{1}]$. Once the partials are created, they are forced to away from each other due to their interactions and thus a stacking fault is formed, as shown in Figure(9). In FCC crystals, the $\{111\}$ plane is the close-packed plane, and thus is the dislocation glide plane and the stacking fault plane. The normal stacking sequence of a perfect FCC crystal along $\langle 111\rangle$ directions is ABCABCABCABC, while with a stacking fault, the stacking sequence turns to ABCABABCABC, missing a 'C' layer. Twins correspond to to a mirror reflection in the $\{111\}$ layer in FCC crystal. For a twin, the previous stacking sequence becomes to ABCAB$\bar{C}$BACBA, where the middle C layer with a bar is the twin boundary.

Due to the high energy of full dislocations, the initiation of plastic deformation with full dislocations needs more work compared to those with stacking faults and twins. In FCC crystals, the twinning energy is around one half of the stacking fault energy [94]. Thus the material that shows plastic deformation with twins has a lower yield stress, which has also been confirmed with MD simulations in Chapter 5.

Since dislocations, stacking faults and twins are lattice defects, the distances

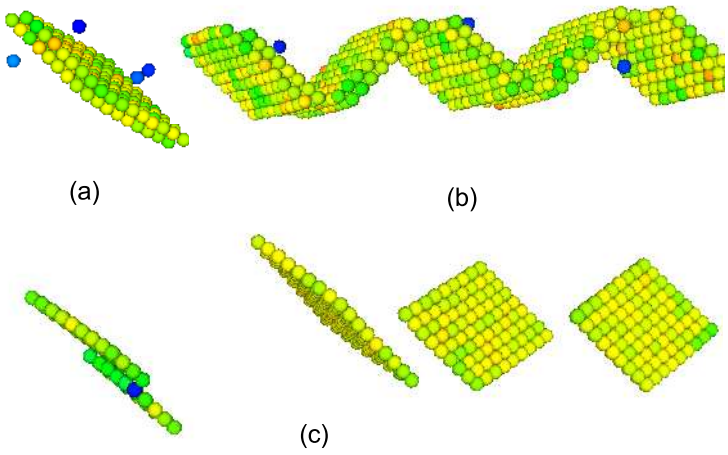

Figure 10: An illustration of stacking faults and twin boundaries observed in nanowires with centrosymmetry parameter. stacking faults are illustrated with (a) and (b); twin boundaries are represented with (c).

among atoms and thus the coordination near defects are different from those in a perfect crystal. So in this thesis, the crystal defects in nanowires are visualized using a centrosymmetry parameter [8], which is a measure of local atomic coordination; a value of zero indicates a bulk, fully-coordinated atom while values increasingly greater than zero indicate the presence of lattice defects, including dislocations, stacking faults, and twins. Figure (10) gives a example of observed stacking faults and twin boundaries in FCC nanowires with centrosymmetry parameter. As can be seen, the stacking faults in nanowires are represented as two {111} layers sticked together, while the twin boundary is represented as one single {111} layer. The reason that stacking faults are observed as two layers and twin boundary is only one layer can be explained with the stacking sequence showed earlier. In the case of stacking faults, both B and A layers in the middle are defective; while in the case of twinning, only one $\bar{C}$ layer is defective. In the thesis, dislocations in nanowires are observed in the format of surface steps and thus could not be shown clearly with centrosymmetry

parameter.

I.3 Research objectives and outlines of the thesis

The objective of this thesis is to study the impact of free surfaces on the mechanical behavior and properties of FCC metal nanowires, including shape memory behavior, surface elasticity, and coupled geometry effects. As indicated previously, the surface stress is an influential factor on nanowires properties, including the self-contraction, which can be substantial as the nanowire cross section reduces to tens of nanometers. The work presented here will use molecular dynamics (MD) and molecular statics (MS) to predict the mechanical properties of metal nanowires and analyze the influence of free surfaces. A brief introduction to the atomistic simulations and embedded atom method (EAM) will be given in Chapter 2. Some other concepts used in my MD simulations will also be clarified. The EAM potential is utilized to provide energetics and interaction forces of a system of atoms, which assures the accuracy of the atomistic simulation.

In Chapter 3, research will be performed to study the shape memory and pseudoelastic behavior of silver nanowires. The mechanical properties of these shape memory nanowires (SMNWs) will be presented and correlated to the shape memory deformation behavior and mechanism. This chapter will first focus on defect-free nanowires to understand the thermomechanical deformation modes, where emphasis is laid on the role of twin boundaries on the deformation behavior and the correlation between the twin boundary movement and the wire mechanical properties. It has been shown that the testing temperatures, straining loading rates, and heat transfer conditions have a great influence on the shape memory behavior and the mechanical properties. Comparisons to polycrystalline shape memory alloys are also made to reveal the exotic mechanical properties of metal nanowires. In the second part, this chapter will present the influence of initial defects on the resulting thermomechanical prop-

erties of metal nanowires and then continue to discuss the influence of initial defects on the resulting thermomechanical behavior. The emphasis in this part is laid on the investigation of the unique deformation mechanism as a result of initial defects under tensile loading, while correlating the deformation behavior to the measured mechanical properties. It has been shown that the defective nanowires, similar to defect-free nanowires, can show shape memory nanowire if the loading conditions are well controlled.

Chapter 4 will present my discussions on surface elasticity of hollow metal nanowires. These nanowires are created along two different axial orientations, $\langle 100 \rangle$ and $\langle 110 \rangle$. It has been shown that by hollowing out a metal nanowire, the elastic properties, including Young's modulus, yield stress, and yield strain, could be enhanced or reduced according to the wire axial direction. The $\langle 110 \rangle$ hollow nanowires exhibit enhanced elastic properties as compared to corresponding solid nanowires; while the $\langle 100 \rangle$ hollow nanowires show no improvement in elastic properties. The variation of mechanical properties depends on the amount of materials removed to create the hollow nanowires. Comparisons to the elastic properties of the corresponding solid nanowires has been made to illustrate the possibility to create future lightweight and strong nanostructures.

Chapter 5 will present the coupled effects of geometry and surface orientation on the mechanical properties of metal nanowires. This chapter will study the nanowires composed of two different axial directions, $\langle 100 \rangle$ and $\langle 110 \rangle$, and of several different side surface orientations. It has been illustrated that by varying the cross section from square to rectangular, nanowires could show distinct mechanical behavior and properties due to the different inelastic deformation mechanisms, which in turn is resulted from biased influence and the discrete nature of side surfaces at nanoscale. It has shown that non-square nanowires generally exhibit lower yield stresses and strains, elevated fracture strains, and a propensity to deform via twinning. It is

shown that the observed deformation mechanisms are resulted from the non-square cross section and the side surface orientations, illustrating possibility of the fact that geometry can be utilized to tailor the mechanical properties of nanowires.

Chapter 6 will present a summary of the main findings in this thesis, including deformation behavior of SMNWs, surface elasticity, and coupled effects of geometry and surface orientations. Then several research topics will be suggested as a continuation of the present research in this work.

CHAPTER II

ATOMISTIC SIMULATION METHODS

This chapter will present a brief introduction to the atomistic simulation methods utilized in this thesis. The main purpose of performing atomistic simulations is to estimate the equilibrium and dynamic properties of a collection of atoms. The atomistic simulations serve as numerical experiments, allowing to learn new properties of materials based on the atomic interaction forces derived from interatomic potentials or from a more realistic first principal/*ab initio* method. Here, the introduction to the molecular dynamics (MD) and molecular statics (MS) simulation methods will first be presented, followed by the explanations on the techniques used in atomistic simulations, including ensembles and virial stress. Finally, a brief description will be given on the embedded atom method (EAM) potential utilized in the atomistic simulations.

II.1 Molecular dynamics methods

Molecular dynamic simulation is a computational method commonly used to analyze material properties. Basically, it involves the processes of deriving a set of equations of motion for a system of atoms and solving these equations by discretization of time. The most straightforward governing equations in MD simulations are derived based on Newton's second law. It is believed that Newton's law is not suitable to characterize the motion of atoms involving coupled behavior of electrons and nuclei, whose motion obeys complicated quantum mechanical laws, such as Schrödinger equation. However, the foundation of using Newton's law in MD simulation is Born-Oppenheimer approximation, which claimed that nuclei are much heavier compared to electrons, and move on a time scale which is two order of magnitude longer than that of electrons. Thus the

movement of electrons is reasonably neglected and the movement of atoms involves the motion of nucleus only, which obeys classical Newton's equations. So Newton's equations are plausible and widely used in MD simulations [95].

Based on the Newton's law, the motion of the atom α is dictated as

$$F_i^\alpha = m_\alpha \ddot{x}_i^\alpha \tag{6}$$

where F_i^α denotes the force in the i^{th} direction acting on the particle α, m_α is the mass of this particle, and x_i^α is the i^{th} component of the α particle position. For a complicated system, hamiltonian dynamics is generally used to derive the equations of motion since it can get these equations more organized in different coordinate systems, such as cylinder and sphere coordinates. The hamiltonian is an expression of the total energy for a simulation system with variables of particle positions and momenta. For an isolated system, the Hamiltonian H is constant for a system of particles and can be expressed as

$$H = \sum_{\alpha=1}^{N} \frac{p_k^\alpha p_k^\alpha}{2m_\alpha} + U(x_i^N, x_j^N, x_k^N) \tag{7}$$

here, p_k^α denotes the momentum of particle α in the k^{th} direction; U is the potential energy of the system, which is a function of positions. x_i^N denotes the ith position of particles, N is the total number of particles. The force field can be derived from Hamiltonian by $F_i = -\frac{\partial H}{\partial x_i}$.

For a system of particles, it is difficult to get a closed form solution for the motion of atoms. Usually, the equations of motion are discretized in time, and finite difference method is used to integrate the equations in time. One commonly used finite difference method in molecular dynamics is the one developed by Verlet [96]. The Verlet algorithm was developed with Taylor series expansion at the time of $t + \delta t$ and

$t - \delta t$,

$$x_i^\alpha(t+\delta t) = x_i^\alpha(t) + \dot{x}_i^\alpha(t)\delta t + \frac{1}{2}\ddot{x(t)}_i^\alpha \delta t^2 + \frac{1}{6}\frac{d^3 x_i^{\alpha(t)}}{dt^3}\delta t^3 + O(\delta t^4) \tag{8}$$

$$x_i^\alpha(t-\delta t) = x_i^\alpha(t) - \dot{x}_i^\alpha(t)\delta t + \frac{1}{2}\ddot{x(t)}_i^\alpha \delta t^2 - \frac{1}{6}\frac{d^3 x_i^{\alpha(t)}}{dt^3}\delta t^3 + O(\delta t^4) \tag{9}$$

Combining equations (8) and (9) leads to the following equation,

$$x_i^\alpha(t+\delta t) = 2x_i^\alpha(t) - x_i^\alpha(t-\delta t) + \ddot{x}_i^\alpha(t)\delta t^2 + O(\delta t^4) \tag{10}$$

According to this equation, the position derived from Verlet algorithm has 4th order accuracy. Combining equations (6) and (10) gives

$$x_i^\alpha(t+\delta t) = 2x_i^\alpha(t) - x_i^\alpha(t-\delta t) + \frac{F_i^\alpha}{m_i}\delta t^2 + O(\delta t^4) \tag{11}$$

This Verlet algorithm predicts the next-step atom position by using the current and previous positions, along with the net force on the particle at current step. This algorithm has the virtues of high stability and high order accuracy and performs the iterative position calculations without using the velocities. However, velocities are necessary to calculate kinetic energy and temperature. A first order central difference method is used to estimate the velocities

$$\dot{x_i^\alpha}(t) = \frac{x_i^\alpha(t+\delta t) - x_i^\alpha(t-\delta t)}{2\delta t} \tag{12}$$

Here, the velocity in the Verlet algorithm has 2nd order accuracy and thus the accuracy of the Verlet algorithm is $O(\delta t^2)$.

A better Verlet algorithm is called velocity Verlet method, which incorporates explicit velocity of high accuracy. The simulations in this thesis are implemented

with velocity Verlet algorithm.

$$x_i^\alpha(t+\delta t) = x_i^\alpha(t) + \dot{x}_i^\alpha(t)\delta t + \frac{1}{2}\ddot{x}_i^\alpha(t)\delta t^2 \tag{13}$$

then, an intermediate velocity at time $t+\delta t$ is introduced and calculated as

$$\dot{x}_i^\alpha(t+\delta t/2) = \dot{x}_i^\alpha(t) + \frac{1}{2}\ddot{x}_i^\alpha(t)\delta t \tag{14}$$

The acceleration and velocity at the next step are calculated as

$$\ddot{x}_i^\alpha(t+\delta t) = -\frac{1}{m}\nabla V(r(t+\delta t)) \tag{15}$$

$$\dot{x}_i^\alpha(t+\delta t) = \dot{x}_i^\alpha(t+\delta t/2) + \frac{1}{2}\ddot{x}_i^\alpha(t+\delta t)\delta t \tag{16}$$

For the equations, it can be seen that the new velocity is calculated based on the previous and the current force on the atom i. The accuracy of velocity is improved and is on the order of $O(\delta t^4)$

In MD simulation, it is necessary to choose an appropriate time step size δt, which should be small enough to capture the detailed vibration of atoms and also should be large enough to overcome the limit of current computational power. A characteristic time is derived based on intrinsic material properties [97, 98]

$$\tau = \sigma\sqrt{\frac{m}{\epsilon}} \tag{17}$$

where the σ, m and ϵ represent bond length, atomic mass and cohesive energy of a bulk atom, respectively. For silver, $\sigma = 2.5$ $\mathring{A}$, $m = 107.87$a.m.u., and $\epsilon = 2.85$ eV. Then the characteristic time is 1.54×10^{-13}. Thus, the time step in Verlet algorithm is a non-dimensional term and the value is chosen to be around 0.005 τ.

To start a simulation, it is necessary to create a set of atoms with initial positions

and velocities. For metals, the initial positions are defined on a lattice based on a certain type of crystal structure, while the initial velocities are assigned according to a Boltzmann distribution at a certain temperature.

II.2 Energy minimization method (Molecular static method)

The molecular dynamics simulation gives the physical motion of atoms, including velocities and positions at each time step. However, the MD simulation is relatively computationally expensive and its feasibility is limited by the time scale. Some phenomena such as diffusion occur over time scales which are beyond the current computational capability. In addition, there are some instances in which it is desirable to learn the energetically favorable configuration. For these cases, energy minimization method (molecular static method) is commonly employed, which is also known as molecular mechanics method. With the energy minimization method, the configuration of a system of atoms with the minimum potential energy can be found by searching the energy landscape globally, which is irrelevant to the time scale. Thus no atomic velocity (temperature) is involved in the molecular static simulations.

Conjugate gradient method is one of the most commonly used energy minimization methods. The conjugate gradient method is designed to solve the linear equations $Ax = b$ by searching for the minimization of the corresponding quadratic equation $f(x) = \frac{1}{2}x^T Ax - b^T x + c$. Here A is a positive-definite and symmetric matrix, x and b are vectors, c is scalar constant. Since A is positive-definite, the surface defined by the function $f(x)$ is like a paraboloid bowl, whose minimum is at the bowl bottom and its derivative can be expressed as $f'(x) = Ax - b$. The error at step i is expressed as $e_i = x_i - x$, which is a vector indicating how far the current solution x_i is from the exact solution x. The residual $r_i = b - Ax_i$ can be treated as the error e_i transformed by matrix A into to the b space. In addition, the residual r_i equals to $-f'(x_i)$ and is the direction of steepest descent. The steepest descent method, an alternative method to conjugate gradient method, uses a line search procedure to minimize the

$f(x)$ along the steepest descent direction. The searching step size is defined by α, $x_{i+1} = x_i + \alpha r_{(o)}$, which is determined by the derivative $\frac{d}{d\alpha} f(x_{i+1})$. Thus it introduces the orthogonal of residual r_i and r_{i+1}. By using this iterative approach, a solution can be found for the linear equations, $Ax = b$, once the error e_i is small enough.

However, in using the method described above, it is usually noticed that the search takes steps in the same direction as some earlier steps. It would be computational efficient that the search takes exactly one step in one direction in the whole energy minimization process. This problem has been solved cleverly by using Gram-Schmidt Conjugation [99], with which the searching directions d_0, d_1, ... , d_N are selected and utilized only once in the whole energy minimization process. The searching directions are A-orthogonal to each other. The A-orthogonal means the vectors are orthogonal to each other in A space and is denoted as $d_i^T A d_j = \delta_{ij}$. The search step size α can be obtained in the same way as the steepest decent method. The conjugate gradient method is not only useful for the quadratic equations, but for any continuous function $f(x)$ for which the gradient $f'(x)$ can be found. Detailed discussions on conjugate gradient method including the convergence analysis and canned algorithms can be found in the work by Shewchuk [99]

II.3 Canonical ensemble

In atomistic simulations, the constraints applied on the simulation systems are of equal importance compared to the equations of motion and numerical methods used to solve those equations. These constraints to control a MD simulation system involve two topics, ensemble types and boundary conditions. In atomistic simulations, periodic boundary condition is commonly utilized to overcome the size limitation confined by computational power. Detailed discussion on periodic boundary conditions can be found in [95]. In this thesis, no periodic boundary conditions are used in order to capture the surface effects of metal nanowires. Thus the following paragraphs will

focus on the introduction to ensembles.

The results of atomistic simulations are a collection of velocities and positions of atoms, which could be related to macroscopic measurable quantities by utilizing statistical mechanics method. The collection of atoms is generally referred to as an ensemble and the macroscopic quantities as ensemble averages. Usually, an atomistic simulation is constrained to ensure certain ensemble averages remain constant, which determines the ensemble type. Thus an ensemble is a collection of atoms which have different microscopic states, but have one identical macroscopic or thermodynamic property.

A general definition of ensemble average is defined as

$$\langle A \rangle_{ensemble} = \int \int dp_N dr_N A(p_N, r_N) \rho(p_N, r_N) \tag{18}$$

where

$$A(p_N, r_N) \tag{19}$$

is the desired macroscopic quantity, which is a function of momenta p and position r. N is total number of atoms in this ensemble. The probability density of the ensemble is given by

$$\rho(p_N, r_N) = \frac{1}{Q} exp[-H(p_N, r_N)/k_B T] \tag{20}$$

where H is Hamiltonian energy, T is the temperature, k_B is Boltzmann's constant and Q is partition function, which is defined as

$$Q = \int \int dp_N dr_N exp[-H(p_N, r_N)/k_B T] \tag{21}$$

Thus to calculate an ensemble average, the simulation must pass through all possible states corresponding to the particular thermodynamic constraints. In MD simulation, it is easier to measure a time average of physical quantity A, which is defined

as

$$\langle A\rangle_{time} = \lim_{\tau\to\infty}\frac{1}{\tau}\int_{t=0}^{\tau} A(p_N(t), r_N(t))dt \approx \frac{1}{M}\sum_{t=1}^{M} A(p_N, r_N) \tag{22}$$

According to ergodic hypothesis in statistical mechanics, the time average equals to the ensemble average, $\langle A\rangle_{time} = \langle A\rangle_{ensemble}$. Thus we can obtain the ensemble averages of desired physical quantities through the time averages with MD simulations. For example, the average kinetic energy is given as

$$K = \langle K\rangle_{time} = \frac{1}{M}\sum_{j=1}^{M}\{\sum_{i=1}^{N}\frac{m_i}{2}v_i v_i\}_j \tag{23}$$

where M is the number of configurations, N is the number of atoms, m_i and v_i are the mass and velocity of the particle i, respectively. While the commonly used quantity temperature is directly related to kinetic energy by the equipartition formula, with an average kinetic energy $k_BT/2$ per degree of freedom.

$$T = 2K/3Nk_B \tag{24}$$

In this thesis, one commonly used ensemble is canonical ensemble, which was developed by Nosé-Hoover [100–103]. This ensemble reproduces the constant temperature for a system of atoms during the experimental process, known as constant NVT ensemble. Here N is number of particles, V is volume, and T is temperature. The construction of Nosé-Hoover ensemble is based on an extended Lagrangian, which contains additional coordinates and velocities. In the constant temperature ensemble, the Lagrangian is defined as

$$L_{Nose} = \sum_{i=1}^{N}\frac{m_i}{2}s^2\dot{r}_i^2 - U(r^N) + \frac{Q}{2}\dot{s}^2 - \frac{L}{\beta}lns \tag{25}$$

where s is the introduced additional degree of freedom, L is a fixed parameter rep-

resenting the number of degrees of freedom in the system, Q is an effective mass associated to s. β is a thermodynamic coefficient, which is related to Boltzmann's constant and externally set temperature, $\beta = 1/(k_B T_{eq})$. The parameter s works like a heat reservoir, which acts as friction coefficient to draw back the current temperature to desired temperature. The logarithmic term is needed for correct scaling of time to keep canonical ensemble. In this extended lagrangian system, the Hamiltonian is given as

$$H_{Nose} = \sum_{i=1}^{N} \frac{p_i^2}{2m_i s^2} + U(r^N) + \frac{p_s^2}{2Q} + L\frac{lns}{\beta} \tag{26}$$

where the p_i and p_s are momenta conjugate to r_i and s. With the choice $L = 3N + 1$, the ensemble average of the extended system coincides with the canonical ensemble average [101].

Hoover [103] has shown that the equations in canonical ensemble can be simplified, where only one thermodynamic friction coefficient $\varsigma = s' p_s'/Q$ is used. The equations of motion in canonical ensemble are given as

$$\dot{r}_i = \frac{p_i}{m_i} \tag{27}$$

$$\dot{p_i} = -\frac{\partial U(r_N)}{\partial r_i} - \varsigma p_i \tag{28}$$

$$\dot{\varsigma} = (\sum_i p_i^2/m_i - \frac{L}{\beta})/Q \tag{29}$$

$$\dot{s} = s\frac{dlns}{dt} = s\varsigma \tag{30}$$

where the dots denote time derivatives. Equations (27) and (eq:ensemble12) are the velocity and accelation of real coordinates; while equations (29) and (eq:ensemble14) are for the additional coordinate. The choice of s, or ς, has a great influence on the detailed nature of dynamics. A large value implies a low inertia of the heat bath

and leads to rapid temperature fluctuations; a small value makes the thermalization process slow. In general, Q is selected to be proportional to L/β and the integration of the system is performed fairly accurately to keep energy conserved [95].

II.4 Embedded atom method (EAM) potentials

One important issue in atomistic simulations is the accuracy and efficiency in the assessment of interatomic forces. The quality of interatomic forces in simulations is determined by the selection of the underlying interatomic potential. Of the present atomistic simulations, first principles MD (*ab initio* MD) is believed to be the most accurate method, which calculates interatomic forces directly from electronic structures. However, this method is computational expensive and the computation cost scales as $O(N^3)$, where N is the number of atoms in the simulation system. Thus, the simulations with *ab initio* MD method is restricted to small collection of atoms. Pair potential model, including Lennard-Jones and Morse potential, is a computationally efficient method. However, it fails to capture the essential physics of metallic bonding, such as surface effects and local bond order.

To keep a balance between results accuracy and computational efficiency, many semi-empirical potentials have been proposed to evaluate the interatomic forces. The force computation based on the semi-empirical potentials is efficient and the cost is on the same order as pair potential, O(N), where N is the number of atoms in the simulation system. These semi-empirical potentials are generally derived by fitting their parameters to the data from experiments or from first principles/*ab initio* MD simulations.

Of these various semi-empirical potentials, the potential provided with embedded atom method (EAM) is commonly used in modeling FCC metals. The parameters of EAM potential are generally obtained by fitting cohesive energy, equilibrium lattice constant, cubic elastic constants, unrelaxed vacancy formation energy, bond

length and bond strength of the diatomic molecule. Since first introduced by Daw *et al.* [104–107], the ability and viability of EAM in modelling metals have been discussed and testified by various researchers [1, 105, 106, 108]. However, the classical EAM method is not suitable for covalent bonding materials [108], such as silicon, due to the fact that chemical bonds in EAM are not angularly dependent. In that case, modified embedded atom methods (MEAM) have been proposed to deal with angular interactions [109].

For a system of metal atoms, the total energy U that comes from EAM can be written as

$$U = \sum_{i}^{N} \left(F_i(\bar{\rho}_i) + \frac{1}{2} \sum_{j \neq i}^{N} \phi_{ij}(R_{ij}) \right) \tag{31}$$

where the summation extends over the total number of atoms N in the system, ϕ_{ij} is pairwise interaction term which is related to interatomic distance R_{ij} of atom i and atom j. ϕ_{ij}, the pairwise interaction term, corresponds to the electrostatic interaction between atom i and j; while F_i, the embedding term, is the quantum mechanical energy involving the influence of electron density. This embedding term can be considered as the energy to embed an atom into an electron gas with a density ρ_i, which comes from the contributions of neighboring atoms. The embedding term, which includes the contribution of electron density, is the key to EAM, and provides a many-body contribution to the energy. ρ_i is electron density term and can be put as

$$\bar{\rho}_i = \sum_{j}^{N} \rho(R_{ij}) \tag{32}$$

where ρ_i depends only on the distance between two atoms. For a system of atoms in equilibrium state, the force that comes from embedding term is balanced with the force derived from pairwise interaction term. A simple way to understand the many-

body effect of the embedding term, $F_i(\bar{\rho}_i)$ is from the variation of bond strength. In EAM, as an atom makes more bonds, the each bond strength becomes weaker; making a new bond decreases the average energy per bond although it increases the total bonding energy. This is consistent with the traditional chemical bonding, which can not be captured in pair potential. Thus the $F_i(\bar{\rho}_i)$ has a positive curvature ($\partial^2 F/\partial^2 \rho > 0$).

In this thesis, the EAM potential utilized for silver SMNWs was developed by Voter and Chen [1, 110]. In this EAM potential, the pairwise interaction term takes Morse potential

$$\phi(r) = D_M[1 - e^{\alpha_M(r-R_M)}]_2 - D_M \tag{33}$$

where the three parameters, D_M, R_M, and α_M define the depth, position of the minimum, and a measure of the curvature at the minimum, respectively. The electron density is taken the form of

$$\rho(r) = r_6[e^{-\beta r} + 2^9 e^{-2\beta r}] \tag{34}$$

where β is an adjustable parameter. To reduce the computational cost and ensure a continuous potential, both $\phi(r)$ and $\rho(r)$ are smoothly cut off at $r = r_{cut}$ by using

$$h_{smooth}(r) = h(r) - h(r_{cut}) + (\frac{r_{cut}}{m})[1 - (\frac{r}{r_{cut}})](\frac{dh}{dr})_{r=r_{cut}} \tag{35}$$

where $h(r) = \phi(r)$ or $\rho(r)$, m =20. Thus in the EAM potential development by Voter and Chen, the five parameters defining pairwise potential and electron density, including (D_M, R_M, α_M, β, and r_{cut}), are optimized by minimizing the standard deviation between the calculated and reference properties of the material. Details can be found in the work by Voter and Chen [1, 110].

In modeling copper nanowires, the EAM potential developed by mishin *et al.* [111] is used in this thesis. This EAM potential was constructed with Morse potential and

a slight different electron density function as compared to that used in Voter-Chen potential. In the parameter fitting process, the potential was optimized by minimizing the mean squared deviation with more parameters than usual and the short-range parts of potential functions are fit to reproduce *ab initio* energies of the copper, which has repaired the common shortcoming existed in EAM potentials. More importantly, the EAM potential by mishin *et al.* has accurately reproduced the intrinsic stacking fault and twinning energies, which are crucial in modeling the inelastic deformation behavior and mechanical properties of metals [69, 112]. Details on this potential can be found in [111].

II.5 The virial theorem

In atomistic simulations, continuum mechanical properties are generally obtained as a function of coordinates and velocities of atoms, which are directly obtained from simulations. Of the mechanical properties, cauchy stress, σ_{ij}, is a commonly used continuum property and is derived based on virial theorem [113]. The basic idea of virial theorem is to relate the kinetic energy of a system of atoms to the forces acting on them. For a system of atoms, the kinetic energy $\bar{K}$ is given as [97, 114]

$$2\bar{K} = \overline{\sum_{\alpha=1}^{N} m_\alpha \dot{x}_i^\alpha \dot{x}_j^\alpha} = -\overline{\sum_{\alpha=1}^{N} x_j^\alpha F_j^\alpha} \tag{36}$$

where N is the total number of atoms, $\dot{x}_i^\alpha$ is the i th component velocity for atom α, m_α is the mass of atom α, F_j^α is the total force on atom α, the overline denotes time average.

The total force F_j^α can be divided into two terms, $F_{j,int}^\alpha$ which comes from interactions among atoms and $F_{j,ext}^\alpha$ provided by interactions against boundaries. For the

atoms within a box of surface area S and volume V, the $F^{\alpha}_{j,ext}$ is

$$\sum_{\alpha=1}^{N} x^{\alpha}_{j} F^{\alpha}_{j,ext} = \oint_{S} x_i \sigma_{ji} n_i da = \int_{V} \frac{\partial}{\partial x_i}(x_i \sigma_{ji}) dv = \int_{V} \{\sigma_{ij} + x_i \frac{\partial \sigma_{ji}}{\partial x_i}\} dv \tag{37}$$

For a fairly long time, the simulation system is in equilibrium state, so $\sigma_{ij,j}$=0. Thus,

$$\sum_{\alpha=1}^{N} x^{\alpha}_{j} F^{\alpha}_{j,ext} = \int_{V} \sigma_{ij} dv \tag{38}$$

Combining (36) and (38), an average stress value of a system of atoms can be written as

$$\sigma_{ij} = \frac{-1}{V} \left(\overline{\sum_{\alpha=1}^{N} x^{\alpha}_{i} F^{\alpha}_{j,int}} + \overline{\sum_{\alpha=1}^{N} m_{\alpha} \dot{x}^{\alpha}_{i} \dot{x}^{\alpha}_{j}} \right) \tag{39}$$

Since the internal force, $F^{\alpha}_{j,int}$, is a spatial derivative of potential, the virial stress takes the form

$$\sigma_{ij} = \frac{1}{V} \left(\frac{1}{2} \sum_{\alpha=1}^{N} \sum_{\beta \neq \alpha}^{N} U'(r^{\alpha\beta}) \frac{\Delta x^{\alpha\beta}_{i} \Delta x^{\alpha\beta}_{j}}{r^{\alpha\beta}} - \sum_{\alpha=1}^{N} m_{\alpha} \dot{x}^{\alpha}_{i} \dot{x}^{\alpha}_{j} \right) \tag{40}$$

where $r^{\alpha\beta}$ is the distance between two atoms α and β, $r^{\alpha\beta} = \|\Delta x^{\alpha\beta}_{j}\|$, $\Delta x^{\alpha\beta}_{j} = x^{\alpha}_{j} - x^{\beta}_{j}$ and U is the potential energy function. From the definition, it can be noticed that the virial stress is defined at equilibrium state and the stress is averaged over a volume instead of a specific area. Recent discussions on methods of obtaining continuum stresses from atomistic simulations were detailed in [115, 116].

CHAPTER III

ON THE THERMOMECHANICAL DEFORMATION BEHAVIOR OF DEFECT-FREE AND DEFECTIVE SILVER SHAPE MEMORY NANOWIRES

In this chapter, atomistic simulations are performed to study the thermomechanical behavior of silver shape memory nanowires (SMNWs), including defect-free and defective nanowires. This chapter will first illustrate the tensile deformation behavior of defect-free silver nanowires under various loading conditions. It is observed that the inelastic deformation behavior of silver nanowires is accompanied with the nucleation and propagation of twin boundaries. The influence of loading boundary conditions, including strain rates, deformation temperatures and heat transfer conditions, are discussed on the mechanical properties of nanowires. In the second part, particular attention is paid to the role of pre-existing defects on the mechanical properties and deformation behavior of silver nanowires. Compared to defect-free nanowires, defective wires are of more use in practice since crystalline defects may be easily introduced by interacting with surroundings in working environments or even in manufacturing processes. A comparison to defect-free wires and polycrystalline SMAs will also be presented. The contents in this chapter are based on the work of Ji and Park [88, 89].

III.1 On the thermomechanical deformation of silver shape memory nanowires

III.1.1 Overview and objectives

Recently, it was demonstrated with molecular dynamics (MD) simulations that certain single crystal FCC metal nanowires can exhibit both shape memory [50] and pseudoelastic behavior [50, 86, 87] that is typically found in exotic alloys such as nickel titanium (NiTi). The shape memory and pseudoelastic behavior is a distinctly

nanoscale phenomena that is not observed in bulk metals, and indicates that metal nanowires may be used in future nano- and micro- scale structures as self-healing materials. Shape memory nanowires (SMNWs) would constitute an improvement over bulk shape memory alloys (SMAs) in multiple respects, including the ability to sustain larger tensile stresses on the order of gigapascals (GPa), having reversible strains that can exceed 40 percent [50, 86, 87] as compared to about 10 percent for bulk, polycrystalline SMAs [117–125], and also because it is experimentally easier to synthesize single crystal materials than complex, multi-material alloys.

The ability of metal nanowires to show shape memory behavior indicates that they may fill the critical need for nanoscale self-healing materials to utilize in future nanomachines, devices, structures, sensors and actuators. While it is exciting that metal nanowires have such potential, much fundamental research needs to be performed to understand their shape memory characteristics. In particular, the basic thermomechanical properties resulting from the uniaxial deformation of SMNWs must be quantified and understood. This behavior is critical as shape memory materials are typically utilized as self-healing materials in situations where the loading and subsequent healing/unloading paths are essentially one-dimensional [125].

Therefore, the goal of this section is to utilize MD simulations to quantify and elucidate the uniaxial thermomechanical deformation characteristics of SMNWs. The MD simulations allow a detailed investigation into the operant deformation mechanisms in the SMNWs while correlating those mechanisms to the concurrent mechanical and thermal response. This chapter first demonstrates that silver nanowires can show shape memory and pseudoelastic behavior. Once these phenomena have been illustrated, the attention will be focused on the uniaxial tensile deformation of the SMNWs. Particular attention is paid to the effects that have been shown to strongly influence the behavior of polycrystalline SMAs [117, 124–126], such as loading strain rate, temperature and ambient heat transfer conditions; the behavior of SMNWs and

Table 1: Properties of Voter-Chen potential for silver compared to experimental data, including lattice parameter (a_0), cohesive energy (E_{coh}), bulk modulus (B), elastic constants (C_{11}, C_{12}, C_{44}), vacancy formation energy (E_{vf}); bond strength (D_e) and bond length (R_e) are values for the diatomic molecule. References for experimental data from [1].

Property	Voter-Chen	Experiment
a_0 (Å)	4.09	4.09
E_{coh} (eV)	2.85	2.85
B (10^{12} erg/cm^3)	1.04	1.04
C_{11} (10^{12} erg/cm^3)	1.24	1.24
C_{12} (10^{12} erg/cm^3)	0.93	0.934
C_{44} (10^{12} erg/cm^3)	0.46	0.461
E_{vf} (eV)	1.1	1.1
D_e (eV)	1.66	1.66
R_e (Å)	2.5	2.5

polycrystalline SMAs are also compared and contrasted when relevant.

III.1.2 Simulation methods

In this work, silver nanowires are considered modeled using the EAM potential developed by Voter and Chen [1,110], which was fit to cohesive energy, equilibrium lattice constant, bulk modulus, cubic elastic constants, unrelaxed vacancy formation energy and the bond length and bond strength of the diatomic molecule. A complete listing of the fitting parameters used for the Voter-Chen potential is given in Table (1).

Square cross section silver $\langle 100 \rangle$ nanowires were created out of a bulk FCC crystal with initial $\{100\}$ surface orientations. The wires were all 20.45 nm long in the z-direction, with cross sectional lengths of 2.045 nm in the x and y-directions. The wires were first thermally relaxed by fixing the ends of the wires to move only in the z-direction, then heating to 500 K using a Nosé-Hoover thermostat [100, 102] with a time step of 0.001 ps. The Nosé-Hoover thermostat introduces an additional degree of freedom into the MD equations of motion; this additional degree of freedom represents a dynamic friction coefficient, which evolves in time according to a first

order differential equation that is based upon the difference between the simultaneous and target kinetic energies of the system. The friction coefficient is utilized to bring the system temperature back to the desired temperature as the difference between current and target temperatures increases.

If the nanowire temperature exceeds a critical temperature T_c, the initially $\langle 100 \rangle$ wires will reorient to a $\langle 110 \rangle$ orientation with four $\{111\}$ side surfaces, which is driven by the ability of the nanowire to reduce its potential energy by reorienting to a configuration with lower energy $\{111\}$ side surfaces [6, 50, 85, 86]. Upon reorienting to the $\langle 110 \rangle / \{111\}$ orientation, the nanowires were further annealed using the Nosé-Hoover thermostat to three different temperatures: 10 K, 200 K and 400 K. These values were chosen to give a range of temperatures less than or equal to the critical reorientation temperature $T_c = 400$ K. The critical reorientation temperature T_c is a function of nanowire cross sectional area; in particular, T_c increases with increasing wire cross section as the magnitude of the surface stresses driving the reorientation decreases with increasing wire cross section [25, 50, 86].

The uniaxial tensile loading that is the focus of this work was performed on the reoriented $\langle 110 \rangle / \{111\}$ nanowires by the application of various tensile strain rates at the three temperatures stated above. The applied strain rates for each nanowire were $\dot{\epsilon} = 2 \times 10^8$, 2×10^9, 2×10^{10}, and were applied in the z-direction by fixing one end of the wire, creating a ramp velocity profile which went from zero at the fixed end to a maximum value at the free end, then pulling the free end at the maximum value. It will be assumed that all references to strain rate in this work will be in units of s^{-1}, while only referring to the strain rate order of magnitude. As with any MD simulation, the strain rates imposed during loading are higher than are generally observed experimentally; this is because the vibrational period of an atom is on the order of femtoseconds (10^{-15} s). For the MD simulation to accurately resolve the atomic vibrational period, the stable time step in the MD calculation must be

smaller than the vibrational period of an individual atom, and thus large strain rates are necessary in order to simulate interesting material phenomena within a computationally accessible time frame. Three decades of applied strain rates were utilized in this work to determine the characteristic material behavior and its variations due to applied loading rate. The computational cost, or simulation time, is around 24 hours for one 10^8 case on a PowerMac 2.4GHz processor; while it is around 2 hours for one 10^9 case.

The ramp velocity profile was utilized to avoid the emission of shock waves from the loading end of the wire. The equations of motion were integrated in time using a velocity Verlet algorithm, and all simulations were performed using the Sandia-developed code Warp [127–129]. For each temperature and strain rate, the uniaxial deformation of the reoriented $\langle 110 \rangle / \{111\}$ nanowires was performed both with and without Nosé-Hoover thermostatting; the thermostatting is utilized to model isothermal deformation by idealized heat transfer to a surrounding medium, while simulations without thermostatting model adiabatic deformation. In the remainder of this section, thermostatted simulations will be referred as isothermal, while the non-thermostatted simulations will be referred as adiabatic.

III.1.3 Shape memory and pseudoelasticity in silver nanowires

This section will first illustrate that silver nanowires can exhibit both shape memory and pseudoelastic behavior. A schematic of the shape memory and pseudoelastic behavior in nanowires is given in Figure (11). As discussed by various researchers [6, 25, 50, 85–87], the reorientation between the $\langle 100 \rangle$ and the $\langle 110 \rangle / \{111\}$ orientations is driven by the ability of the nanowire to reduce its overall potential energy by exposing low energy $\{111\}$ side surfaces. This reorientation is demonstrated in Figure (12) for an initial $\langle 100 \rangle$ silver nanowire at 500 K.

A higher temperature than is needed to reorient the wire is used in order to create

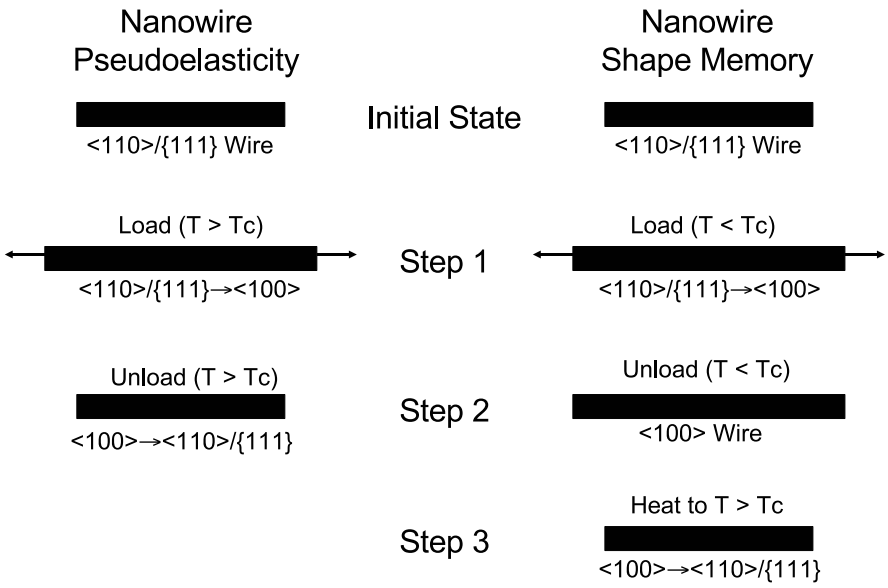

Figure 11: Schematic of shape memory and pseudoelasticity in FCC metal nanowires. T_c is the critical temperature for an initially $\langle 100 \rangle$ nanowire to reorient to a $\langle 110 \rangle$ nanowire with $\{111\}$ side surfaces for a given wire cross sectional length.

a reoriented $\langle 110 \rangle / \{111\}$ wire without surface defects or interior stacking faults; the deleterious effects of such defects on the thermomechanical behavior of SMNWs will be explored in the next section based on the work of Ji and Park [89]. The addition of thermal energy initially causes expansion of the nanowire; however, the expansion of the nanowire also increases the disorder of the nanowire surfaces, thus increasing the surface stresses. This increase in surface stress is then sufficient to drive the reorientation of the nanowire from the initial $\langle 100 \rangle$ orientation with square cross section to a lower energy $\langle 110 \rangle / \{111\}$ orientation with a rhombic cross section. The fact that the lower energy $\langle 110 \rangle / \{111\}$ orientation is observed through MD simulations is in agreement with experimental results reported by Liu *et al.* [130], who showed that the $\langle 110 \rangle$ orientation is preferred for copper nanowire growth and synthesis.

The pseudoelastic behavior is illustrated in Figure (13). The $\langle 110 \rangle / \{111\}$ wire in Figure (13a) is obtained by the heating the initially $\langle 100 \rangle$ nanowire at 500 K, and corresponds to the reoriented wire shown in Figure (12c). Upon loading the reoriented

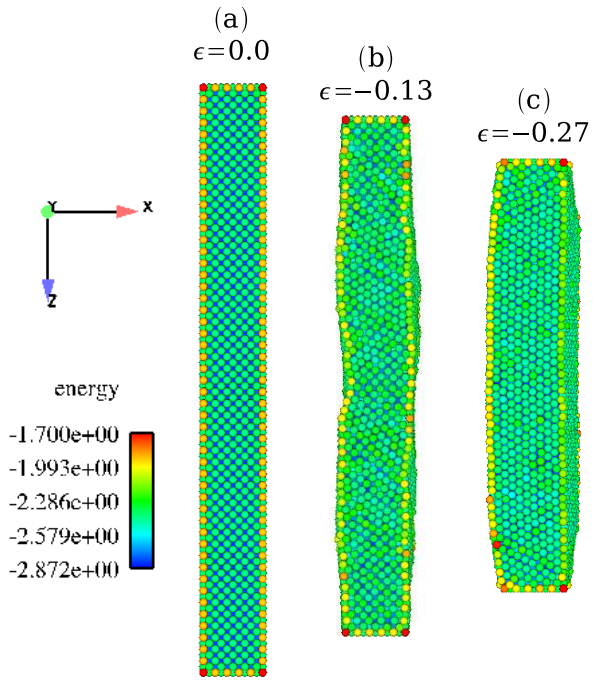

Figure 12: Reorientation of an initially ⟨100⟩ silver nanowire to a ⟨110⟩/{111} nanowire at 500 K.

⟨110⟩/{111} wire isothermally at 500 K at a strain rate of 10^8, the initial ⟨100⟩ orientation is reached at a strain of $\epsilon = 0.43$ in Figure (13c). Because the deformation has occurred at a temperature higher than the critical reorientation temperature T_c, the nanowire is unstable in this new orientation, and reorients back to the ⟨110⟩/{111} configuration in Figures (13d-e). Note that the amount of recoverable strain in the SMNWs is on the order of 40 percent, which is significantly higher than the 10 percent typically seen in polycrystalline SMAs [125].

The shape memory behavior of the silver nanowires is illustrated in Figure (14) when the reoriented ⟨110⟩/{111} nanowire is loaded isothermally at 10 K at a strain rate of 10^8. As shown in Figures (14a-d), the new ⟨100⟩ nanowire was gradually heated in increments of 100 K, while running the simulation for 100 ps at each new elevated temperature. The same figure illustrates that the ⟨100⟩ nanowire is stable until heated above the critical reorientation temperature T_c=400 K. At that temperature,

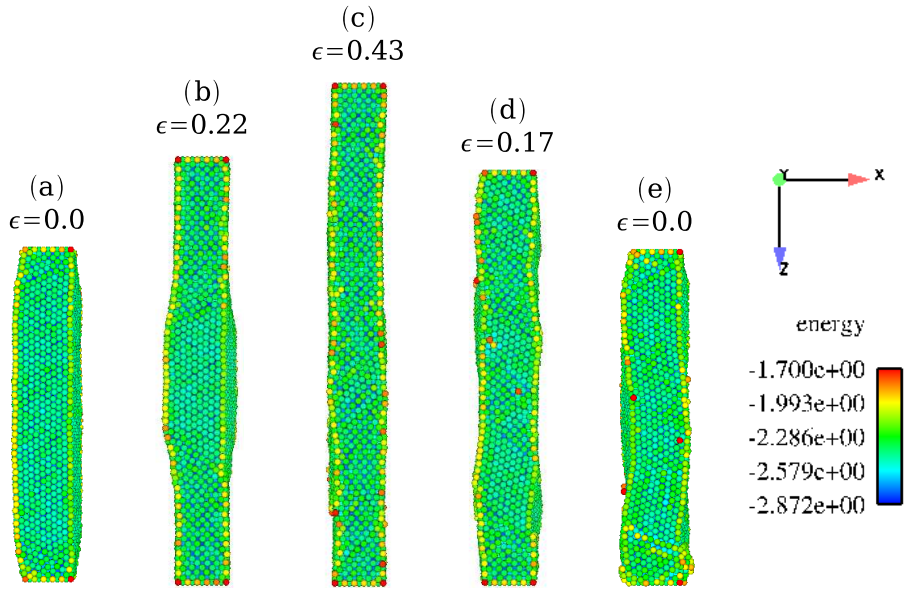

Figure 13: Illustration of pseudoelasticity in silver nanowires at 500 K. Steps (a)-(c) indicate stress-induced reorientation from $\langle 110 \rangle / \{111\}$ to $\langle 100 \rangle$ at 500 K. Steps (d)-(e) show subsequent reorientation back to $\langle 110 \rangle / \{111\}$ because 500 K $> T_c$.

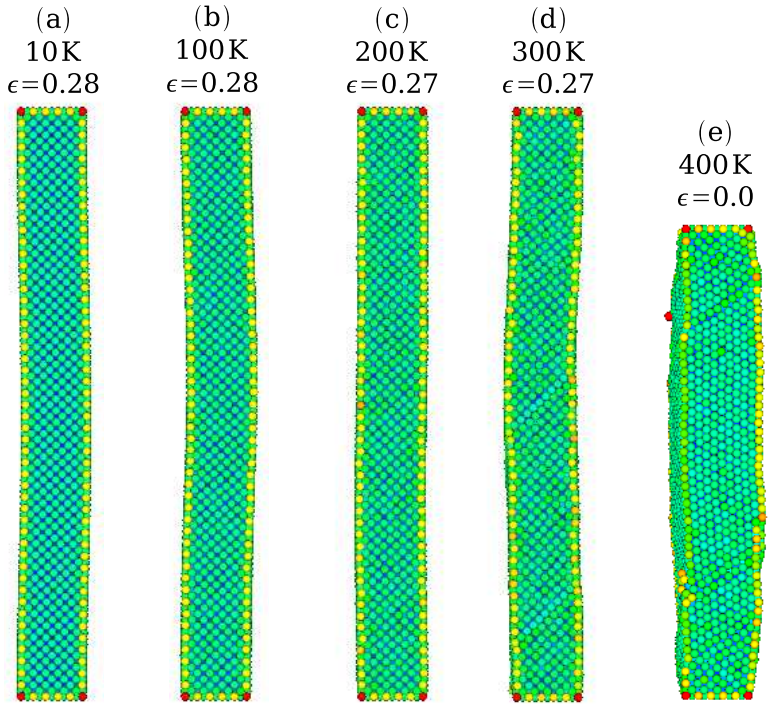

Figure 14: Illustration of shape memory in silver nanowires. Steps (a)-(d) show stable $\langle 100 \rangle$ nanowire heated between 10 K and 300 K. Step (e) illustrates reorientation to $\langle 110 \rangle / \{111\}$ that occurs when heating to T_c, or 400 K occurs.

the ⟨100⟩ nanowire is unstable, and reorients back to the ⟨110⟩/{111} configuration as shown in Figure (14e), thus showing shape memory behavior. Further details on the mechanisms controlling shape memory and pseudoelasticity in metal nanowires can be found in Park *et al.* [50].

This section is concluded by emphasizing that the shape memory and pseudoelastic behavior in metal nanowires is a nanoscale phenomena that is made possible by the fact that significant surface stresses that continuously drive the reorientation from the high energy ⟨100⟩ orientation to the lower energy ⟨110⟩/{111} orientation exist at the nanoscale. Because the effects of surface stresses rapidly diminish as the size scale of materials increases, the shape memory and pseudoelastic behavior is not seen in the corresponding bulk metals [6, 25, 50, 85–87].

III.1.4 Uniaxial thermomechanical deformation of silver SMNWs

This section will summarize the thermomechanical behavior under uniaxial tensile deformation for the silver SMNWs as obtained via atomistic simulations over three decades of strain rates, various deformation temperatures and heat transfer conditions. Strain is defined as $\epsilon = \frac{l-l_0}{l_0}$, where l is the current wire length and l_0 is the reoriented ⟨110⟩/{111} wire length. The stresses reported in this thesis are calculated using the virial theorem. The validity of virial stress was testified by calculating stresses both with and without the second, or kinetic term, and report values using the full virial stress is given in Chapter 2. While the stress values tend to increase when neglecting the kinetic portion of the virial, the major trends reported in this work are the same regardless of the virial stress definition utilized.

The stress-induced reorientation at 10 K at a strain rate of 10^8 from ⟨110⟩/{111} back to the initial ⟨100⟩ orientation for an isothermally loaded wire is detailed in Figure (15). This particular example is shown as it illustrates the mechanisms required to reorient a nanowire between the ⟨110⟩/{111} and ⟨100⟩ orientations. As illustrated

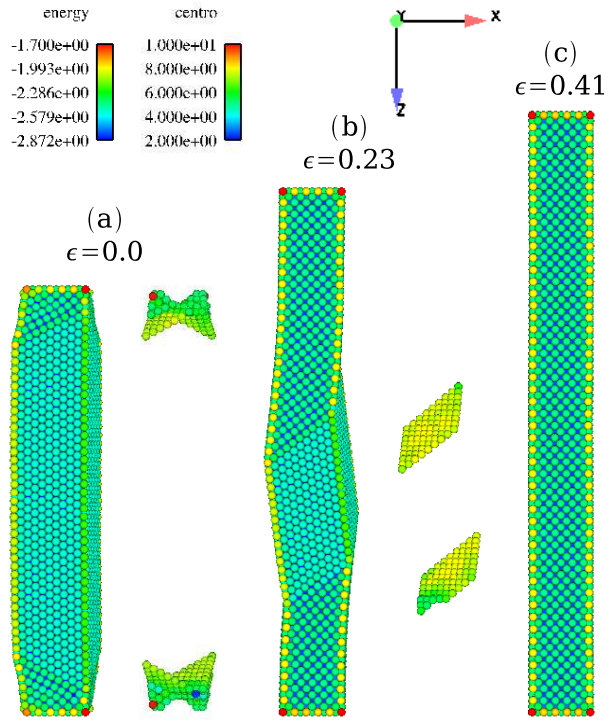

Figure 15: Stress-induced reorientation from $\langle 110 \rangle / \{111\}$ at zero strain to initial $\langle 100 \rangle$ orientation at about 41 percent strain for SMNW isothermally loaded at $\dot{\epsilon} \approx 10^8$. Values of potential energy are in eV, centrosymmetry is defined in [8].

in Figure (15a), the reoriented $\langle 110 \rangle / \{111\}$ wire initially contains twin-like defects near the wire ends, though the interior is defect free [50, 85–87]. Upon application of tensile loading, the twins begin to propagate from the ends of the wire towards the wire center, as illustrated for the snapshot at $\epsilon = 0.23$ in Figure (15b). The propagation of the twin boundaries is well visualized using the centrosymmetry parameter [8], which is a measure of local atomic coordination; a value of zero indicates a bulk, fully-coordinated atom while values increasingly greater than zero indicate the presence of lattice defects such as stacking faults and twins. At a strain of $\epsilon = 0.41$ with respect to the reoriented $\langle 110 \rangle / \{111\}$ configuration as shown in Figure (15c), the wire regains its initial $\langle 100 \rangle$ orientation after the twins meet and annihilate each other near the wire center.

Figure (16) gives the stress-strain curves for the both adiabatically and isother-

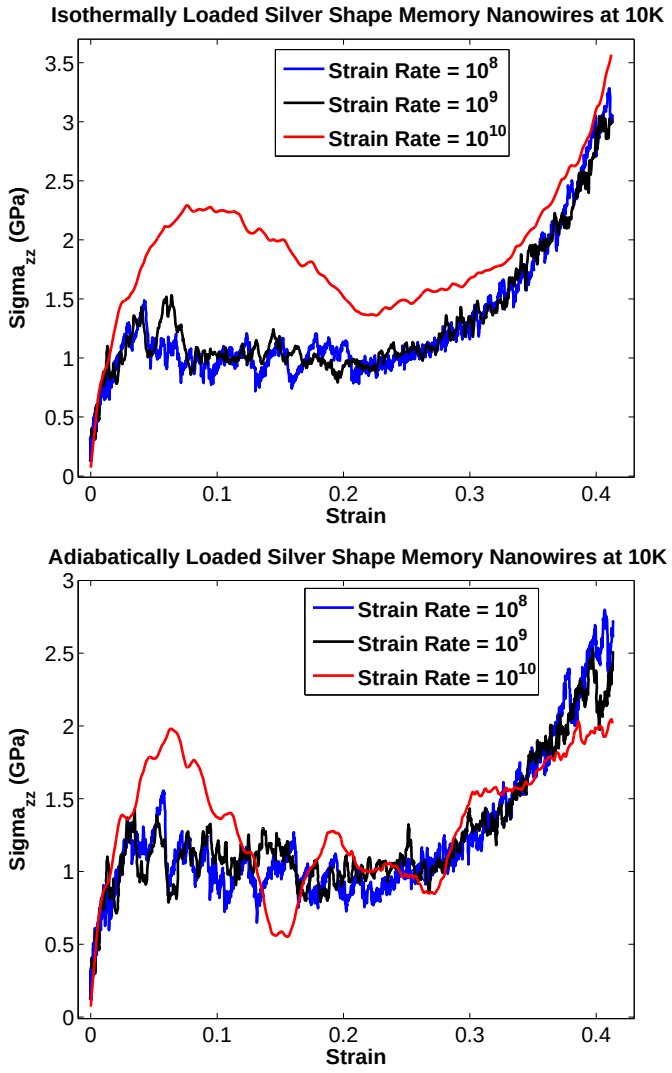

Figure 16: Uniaxial stress-strain response for silver SMNWs at 10 K over three decades of applied strain rates. (a): isothermal. (b): adiabatic.

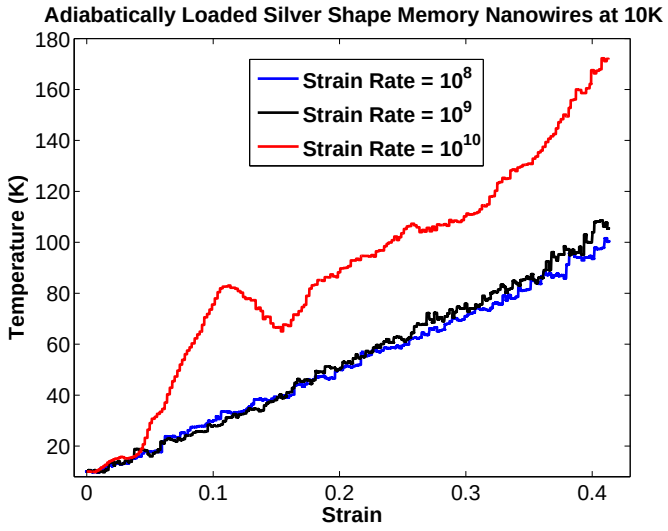

Figure 17: Evolution of temperature for three decades of applied strain rates in adiabatically loaded SMNWs initially at 10 K.

mally loaded SMNWs at 10 K over three decades of strain rates. As can be seen, the transformation stress, or the stress at which linear elastic deformation stops prior to a period where the stress remains approximately constant as a function of strain, is about 1.3 GPa in both cases. In single crystal SMNWs, the transformation stress corresponds to the stress at which the twins that are present at the ends of the reoriented $\langle 110 \rangle / \{111\}$ nanowires in Figure (15a) begin to propagate towards each other upon application of uniaxial loading. The stress plateau between $\epsilon = 0.04$ and $\epsilon = 0.25$ in Figures (16a) and (16b) occurs while the twins propagate towards each other due to the applied external loading. During this period, the reoriented $\langle 110 \rangle / \{111\}$ and initial $\langle 100 \rangle$ orientations co-exist in the nanowire while separated by the propagating twin boundaries, and is best illustrated by the snapshot at $\epsilon = 0.23$ in Figure (15b).

Modeling an isothermal deformation via thermostatting appears to have a large effect on the stress state when the initial $\langle 100 \rangle$ configuration is reached. For the isothermal case, the stress when the $\langle 100 \rangle$ orientation is reached is at least 3 GPa for all strain rates considered for the initially 10 K $\langle 110 \rangle / \{111\}$ nanowires as shown in

Figure (16a). In contrast, under adiabatic loading the stress when the $\langle 100 \rangle$ orientation is reached is at most 2.5 GPa as shown in Figure (16b). The reason for this can be ascertained by tracking the temperature of the initially 10 K nanowires as a function of strain in the adiabatically loaded cases. As shown in Figure (17), the temperature of the nanowires loaded at strain rates of 10^8 and 10^9 rises about 90 K during the stress-induced reorientation back to $\langle 100 \rangle$.

In metal nanowires, an increase in temperature generally leads to a decrease in observable strength. For example, nanowires have been seen to show their highest strength levels under quasistatic loading [69]. The quasistatic loading allows for elevated strength because the atoms can maintain a regular, crystalline structure during loading as they are allowed to relax back to energy minimizing positions after each load increment. In the dynamic, finite temperature loading utilized in this work, such relaxation back to energy minimizing positions cannot occur due to inertia along with the high loading rates, and thus thermal softening is observed in the stress-strain response.

Under very high strain rate loading ($\dot{\epsilon} \approx 10^{10}$), the SMNWs exhibit distinct, thermomechanically-dependent behavior, which will be discussed in detail. This section will first analyze the SMNWs at 10 K, for both the isothermal and adiabatic cases. As seen in Figure (16a) for the isothermal nanowires, the transformation stress, the magnitude of the resulting stress plateau, and the stress when the original $\langle 100 \rangle$ orientation is reached are all higher at the strain rate of 10^{10} than the stresses obtained at lower strain rates. At the strain rate of 10^{10}, the observed elevated stress response in SMNWs is similar to the amorphization phenomena previously reported for nanowires by Ikeda *et al.* [60], in which loading at strain rates above $\dot{\epsilon} \approx 10^{10}$ causes fluid-like behavior in the nanowires, thus suppressing traditional crystalline deformation modes such as slip, and increasing the resulting strength. The specific deformation mechanisms occurring at the elevated strain rates leading to the increased

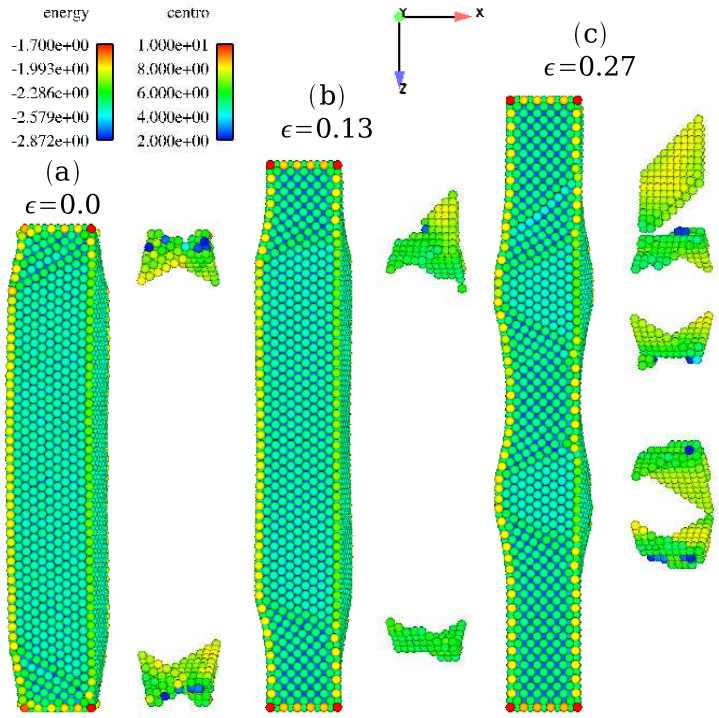

Figure 18: Stress-induced reorientation from $\langle 110 \rangle / \{111\}$ to initially $\langle 100 \rangle$ orientation for isothermal silver nanowire at 10 K loaded at strain rate of $\dot{\epsilon} \approx 10^{10}$. Note the multiple twin boundaries propagating along the nanowire length. Values of potential energy are in eV, centrosymmetry is defined in [8].

strength are discussed below.

At the strain rate of 10^{10} under adiabatic loading, the nanowire temperature rises by 160 K, which is significantly greater than the 80 K at the lower strain rates; this can be explained by the significantly higher atomic velocities at that elevated strain rate. Furthermore as shown in Figure (16b), the SMNWs loaded adiabatically at strain rates of 10^{10} at 10 K show deviations in stress when the $\langle 100 \rangle$ orientation is reached as the high strain rate deformation in conjunction with the nanowire temperature rise causes thermal softening and premature yielding of the nanowires before the $\langle 100 \rangle$ orientation is reached.

The stress response after the transformation stress is reached also diverges dramatically depending on whether isothermal or adiabatic loading is considered. The

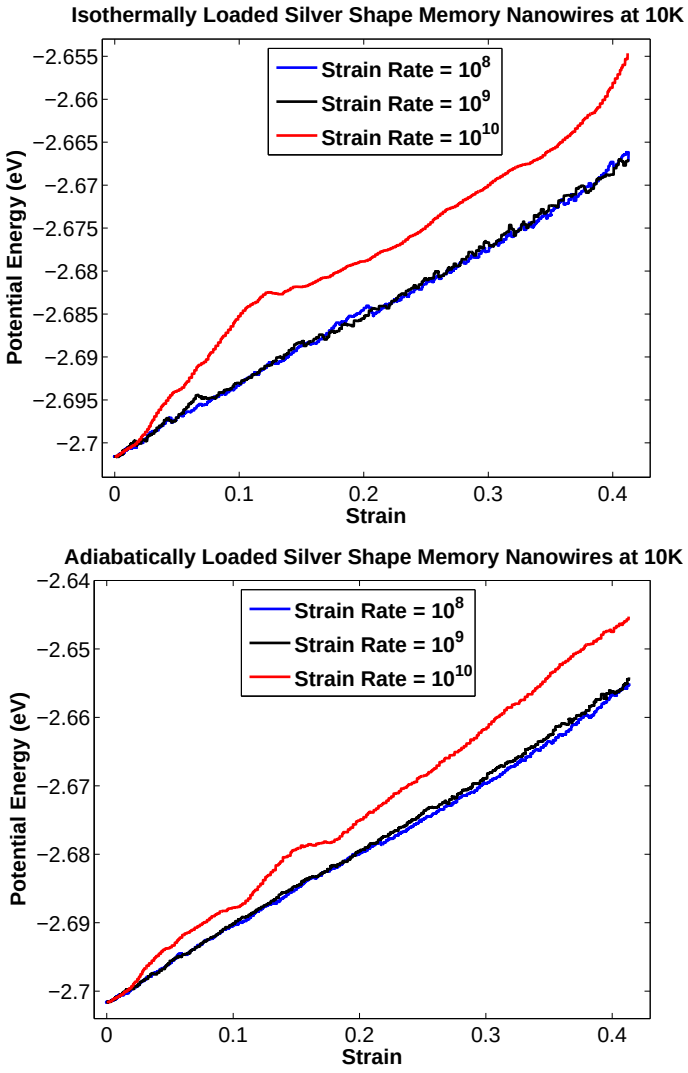

Figure 19: Potential energy vs. strain for silver shape memory nanowire under uniaxial tension at 10 K. (a): isothermal. (b): adiabatic.

impact of performing the tensile loading under isothermal conditions is illustrated by the stress-strain response for $\dot{\epsilon} \approx 10^{10}$ in Figure (16a), where it is shown that following the transformation stress, the tensile strength plateau of the isothermal wire at 10 K at the elevated strain rate of 10^{10} remained greater than at the lower strain rates, while the adiabatic wire did not. The reason for this is because the high loading rates in conjunction with the isothermal loading appears to stabilize the deformation; a similar phenomenon was observed in polycrystalline NiTi wires by Shaw and Kyriakides [117]. In that work, high strain rate loading caused local heating in NiTi wires along with an increase in stress. Eventually, the high local stress levels caused the initiation and propagation of martensitic twins in cooler regions of the wire; the propagation of multiple fronts resulted in lower propagation velocities, which then improved cooling by the ambient fluid.

In SMNWs, the stabilization also takes the form of multiple twins initiating and propagating along the nanowire length, as illustrated in Figure (18c). In addition, analysis of the nanowire potential energy during the deformation illustrates the nature of stabilization as seen in Figure (19a). For the strain rate of 10^{10} for the isothermal wire, it is visible that around a strain of $\epsilon = 0.12$, the slope of the potential energy suddenly decreases, corresponding to a more stable deformation path. In addition, the stress during the twin boundary propagation in Figure (16a) is higher than the plateaus at the lower strain rates. The stress is correspondingly greater in this situation because more stress is needed to continue the deformation if multiple twinning systems are activated.

For the adiabatically loaded SMNW at 10 K and $\dot{\epsilon} \approx 10^{10}$, the difference in deformation can be obtained by a combination of the stress-strain response, potential energy and temperature plots. As seen in Figure (16b), the stress that the SMNW can sustain at a strain rate of 10^{10} drops below the sustainable stresses at lower strain rates after the transformation stress is reached. In addition, the temperature

in the nanowire decreases suddenly at a strain level of about $\epsilon = 0.12$ in Figure (17), just as the stress drops below that of the lower strain rates in Figure (16b). The temperature drop indicates a drop in nanowire velocities, while the stress drop indicates that less work is necessary to continue deformation in the SMNW. These facts, when combined with visual inspection of the propagating twins, showed that only one end of the twin boundary was propagating in the strain range between $\epsilon = 0.12$ and $\epsilon = 0.15$ for the adiabatically loaded nanowire. The propagation of only one of end of the twin boundaries explains both the drop in temperature (since one twin boundary is stagnant), and also the resulting drop in stress (since less effort is needed to continue loading if only one twin boundary is propagating).

The reason this occurs is due to the large temperature increase (80 K) before the transformation stress is reached at $\epsilon = 0.12$, as seen in Figure (17). The high local heating thus serves to impede the twin boundary motion in the SMNWs; similar effects on dislocation propagation that are generally attributed to viscous drag at high loading rates have been reported [97,131,132]. Thus, this effect is different from what has been seen in polycrystalline SMAs [117], where high local heating due to high strain rate loading promotes initiation and propagation of twin fronts in other areas within the NiTi wire.

Examining the stress-strain response of the nanowires at elevated temperatures reinforces some of the findings discussed earlier in this section. Indeed, the stress-strain response of both isothermal and adiabatically loaded SMNWs at a temperature of 200 K is shown in Figure (20), while the stress-strain response at 400 K is shown in Figure (21). An important trend to note is that the transformation stress decreases with increasing deformation temperature. At 200 K, the transformation stress appears to be about 1 GPa, while at 400 K, the transformation stress drops further to about 0.85 GPa. The plateau stress following the transformation stress also decreases with increasing temperature, and finally the stress at the reoriented $\langle 100 \rangle$ orientation also

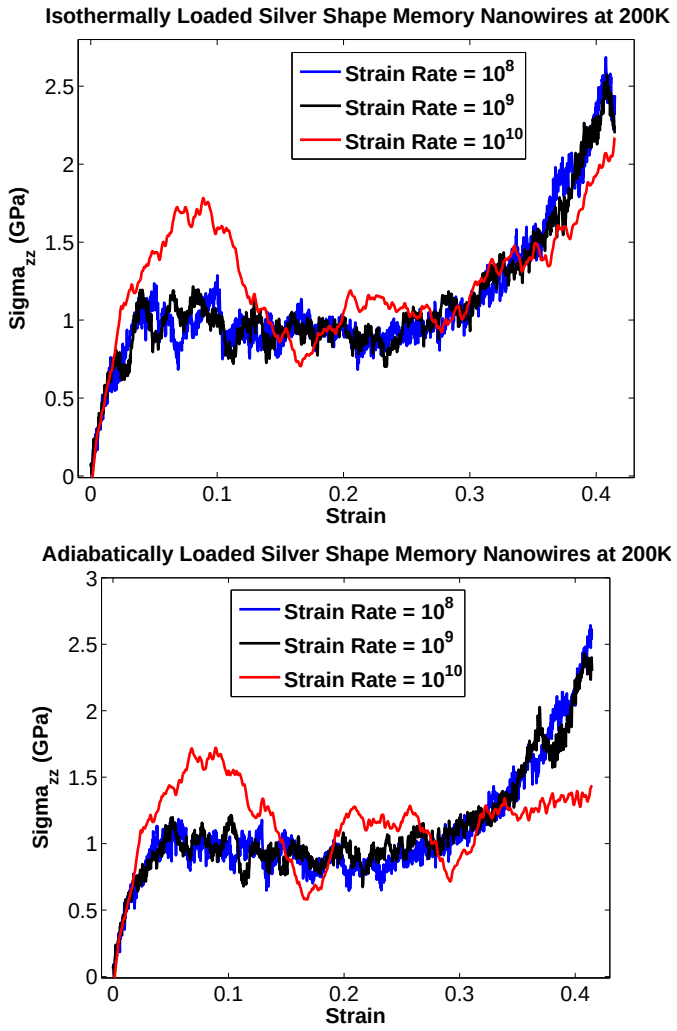

Figure 20: Uniaxial stress-strain response for silver SMNWs at 200 K over three decades of applied strain rates. (a) isothermal. (b): adiabatic.

drops, from about 3 GPa at 10 K to about 2.5 GPa at 200 K down to about 2 GPa at 400 K. In comparison, NiTi at 283 K as reported by Shaw and Kyriakides [117] had a transformation stress of about 0.2 GPa, with a maximum tensile stress of about 1.2 GPa.

The fact that the transformation stress decreases in SMNWs with increasing temperature contrasts the behavior typically seen in bulk, polycrystalline SMAs [117], where the transformation stress generally increases with increasing temperature. The reason for the stress decrease with increasing temperature in SMNWs is the same as why the $\langle 100 \rangle$ reorientation stress decreases with increasing temperature. That is, in the dynamic, finite temperature loading utilized in this work, while the lattice remains crystalline, relaxation back to idealized energy minimizing positions cannot occur due inertia and the high loading rates, and thus thermal softening is observed in the stress-strain response.

In comparing the temperature profiles for the adiabatically loaded SMNWs at 200 K and 400 K in Figure (22) with that at 10 K in Figure (17), we note that the amount of temperature increase during uniaxial loading decreases with increasing deformation temperature. The smaller temperature increase at higher temperatures implies that the velocities of the propagating twins is lower at the elevated temperatures; we again mention the effects of viscous drag as being relevant for the present situation [97,131, 132]. In the present case, additional complications in the form of surface stresses due to the small sizes of the wires may also be critical, so the effect of phonon drag within confined geometries should be investigated further.

The reductions in temperature increase during deformation at higher temperatures also leads to greater similarity in the mechanical response between isothermal and adiabatic loading conditions. For example, at 10 K, the difference in stress when the $\langle 100 \rangle$ orientation is reached is about 15 percent between isothermal and adiabatic loading at a strain rate of 10^8. In contrast, at 400 K, the difference is reduced to

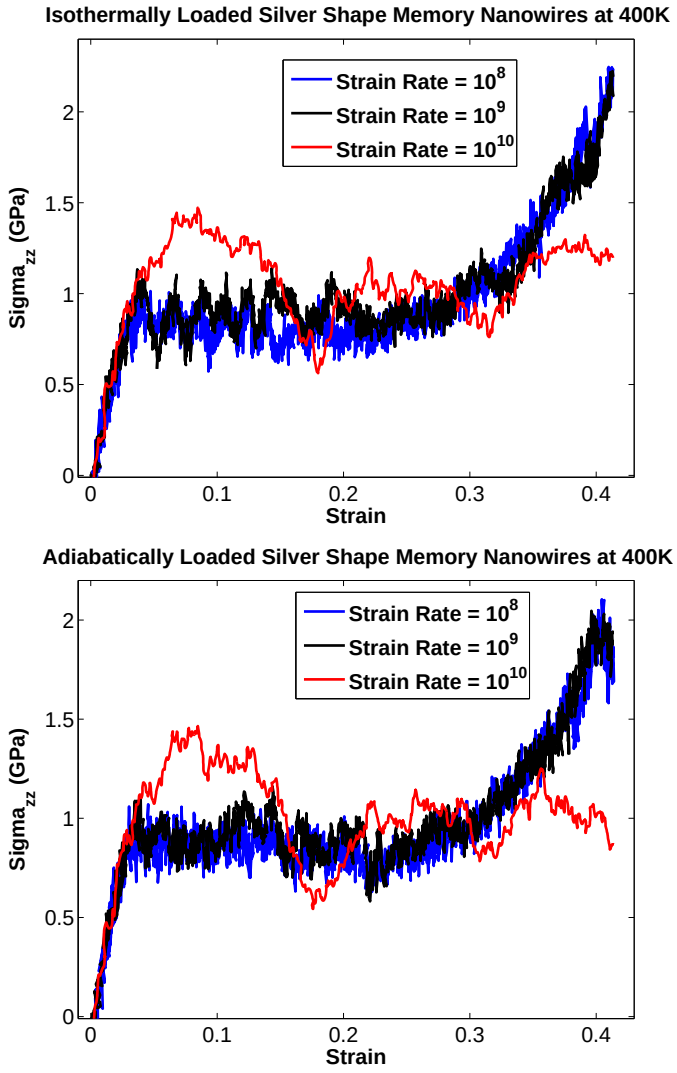

Figure 21: Uniaxial stress-strain response for silver SMNWs at 400 K over three decades of applied strain rates. (a): isothermal. (b): adiabatic.

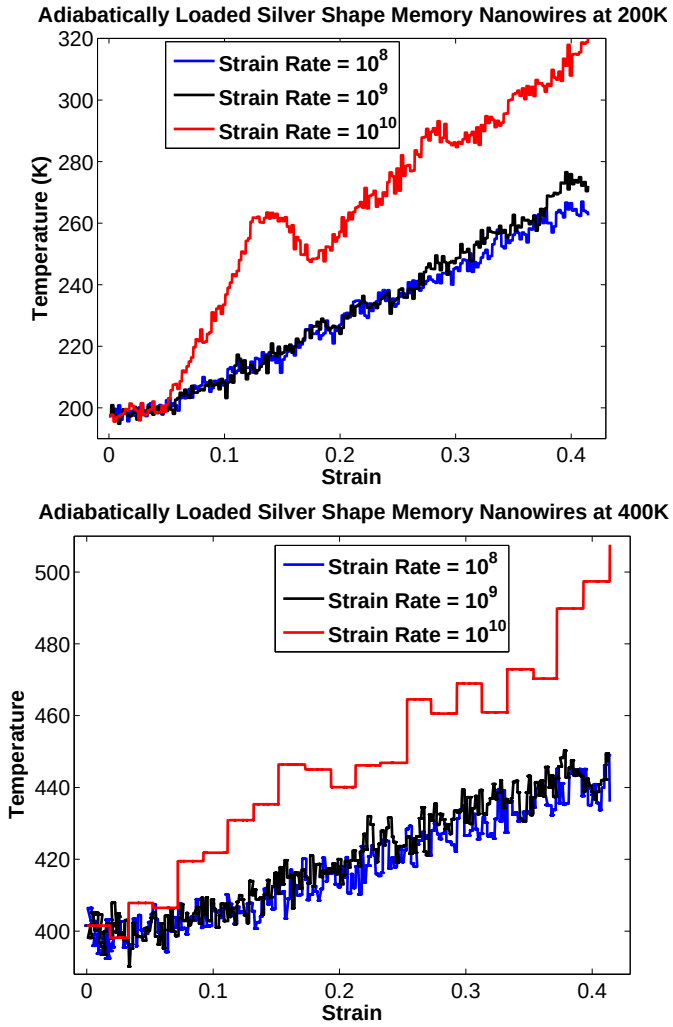

Figure 22: Evolution of temperature for three decades of applied strain rates in silver SMNWs. (a): initially 200 K nanowire. (b): initially 400 K nanowire.

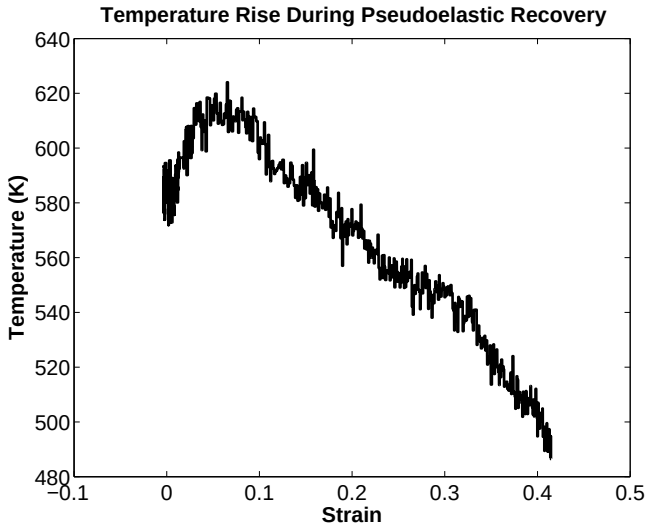

Figure 23: Temperature rise during pseudoelastic recovery of a shape memory silver nanowire initially at 500 K.

about 6 percent due to the smaller temperature increase. Also noteworthy is the fact that the deformation stabilization seen at lower temperatures at the strain rate of $\dot{\epsilon} \approx 10^{10}$ is not seen at the elevated temperatures; at elevated temperatures at these strain rates, premature yielding is observed before the $\langle 100 \rangle$ orientation is reached, producing reduced strength as compared to the lower loading rates.

A key difference between the behavior of single crystal SMNWs and polycrystalline SMAs is in the thermal signature that occurs during forward and reverse reorientation. As was illustrated earlier in this section, in the absence of thermostatting to mimic an isothermal deformation, the temperature in the nanowires increases substantially during the stress-induced reorientation from $\langle 110 \rangle / \{111\}$ to the initial $\langle 100 \rangle$ orientation. Similarly, during the pseudoelastic recovery of inelastic strain once the $\langle 100 \rangle$ orientation is reached, the pseudoelastic process is again exothermal, as shown in Figure (23).

In polycrystalline SMAs, the stress-induced phase transformation going from austenite to martensite is typically exothermic, while the unloading from martensite to

austenite is generally endothermic. In particular, in polycrystalline SMAs, it is possible to cycle between the austenite and martensite phases simply by sufficiently cooling or heating the SMA. However, SMNWs are fundamentally different in that reorientation occurs between the higher energy $\langle 100 \rangle$ and lower energy $\langle 110 \rangle / \{111\}$ orientations; no phase transformation occurs between the two configurations, which are simply different FCC crystallographic orientations. Thus, while heating a $\langle 100 \rangle$ nanowire above a critical temperature T_c will cause reorientation to $\langle 110 \rangle / \{111\}$, cooling the subsequent $\langle 110 \rangle / \{111\}$ oriented wire will not cause reorientation back to the initial $\langle 100 \rangle$ orientation; this is only possible by the application of tensile stress to the $\langle 110 \rangle / \{111\}$ nanowire.

III.2 The effect of defects on the mechanical behavior of silver shape memory nanowires

III.2.1 Objectives

The purpose of this section is to characterize the influence of pre-existing lattice defects on the thermomechanical behavior and properties of silver shape memory nanowires. Due to the likelihood of future difficulty in synthesizing defect-free nanowires, and due to the fact that individual lattice or surface imperfections can dramatically degrade the mechanical strength of nanoscale materials, such investigations are necessary in order to assess the practical potentials of these novel shape memory materials. By performing atomistic simulations of the tensile deformation of $\langle 110 \rangle / \{111\}$ nanowires with initial defects, it has been demonstrated that lower loading rates and lower temperatures are conducive to producing optimal shape memory behavior in the nanowires. This section have also quantified the effects of the pre-existing defects on the mechanical properties of shape memory nanowires and have compared to defect-free nanowires and polycrystalline shape memory alloys for further insight.

III.2.2 Simulation methods

Classical molecular dynamics [98, 133, 134] simulations were performed modeling the atomic interactions using the embedded atom method (EAM) [105, 108] as the underlying atomic interaction model. The specific potential utilized in this work for silver was developed by Voter and Chen [1, 110], which was fit to cohesive energy, equilibrium lattice constant, bulk modulus, cubic elastic constants and the unrelaxed vacancy formation energy, bond length and bond strength of the diatomic molecule. Detailed parameters of this potential is given in Table (1).

Square cross section silver $\langle 100 \rangle$ nanowires were created out of a bulk FCC crystal with $\langle 100 \rangle$ surface orientations. The wires were all 20.45 nm long in the z-direction, with a cross sectional lengths of 2.045 nm in the x and y-directions. Because the shape memory effect is obtained in nanowires through reversibility between $\langle 100 \rangle$ and $\langle 110 \rangle / \{111\}$ orientations, the $\langle 100 \rangle$ to $\langle 110 \rangle / \{111\}$ reorientation was achieved by fixing the ends of the wires to move only in the z-direction, then heating to 500 K using a Nosé-Hoover thermostat [100, 102] with a time step of 0.001 ps. The computational cost is around 24 hours for one 10^8 case on a PowerMac 2.4GHz processor; while it is around 2 hours for one 10^9 case.

As was illustrated by multiple researchers [6, 50, 86–88], there exists a critical reorientation temperature T_c which is directly proportional to the wire cross sectional length; as the wire cross sectional length increases, the amount of thermal energy needed to assist the intrinsic surface stresses in driving the $\langle 100 \rangle$ to $\langle 110 \rangle / \{111\}$ reorientation increases accordingly. Previous studies have shown that the shape memory effects are achieved by stress-inducing a reorientation from $\langle 110 \rangle / \{111\}$ to $\langle 100 \rangle / \{100\}$ at a temperature less than T_c. By subsequently heating the stress-induced $\langle 100 \rangle / \{100\}$ wire above T_c, reorientation back to $\langle 110 \rangle / \{111\}$ occurs thus illustrating the shape memory effect.

The focus of this section will therefore be on the uniaxial tensile deformation of the $\langle 110 \rangle / \{111\}$ nanowires with initial defects. The $\langle 110 \rangle / \{111\}$ nanowires that were tensile loaded were obtained by annealing the reoriented $\langle 110 \rangle / \{111\}$ nanowires to three different temperatures using the Nosé-Hoover thermostat: 30K, 200K, 400K. These temperatures were chosen as representative values that are less than or equal to the critical reorientation temperature of 400 K for the wire size chosen for this paper. The annealed wires were then loaded in tension in the z-direction at the three temperatures and strain rates of $\dot{\epsilon} = 1 \times 10^8$, 1×10^9, 1×10^{10} by fixing one end of the wire, creating a ramp velocity profile which went from zero at the fixed end to a maximum value at the free end, then pulling the free end at the maximum value. All references to strain rate in this section will be in units of s^{-1}. As with any MD simulation, the strain rates imposed during loading are higher than are generally observed experimentally. Thus, simulations are performed on the material response of the $\langle 110 \rangle / \{111\}$ nanowires across three decades range of accessible MD loading rates to isolate the characteristic mechanical properties. The equations of motion were integrated in time using a velocity Verlet algorithm, and all simulations were performed using the Sandia-developed code Warp [127–129].

For each temperature and strain rate, the uniaxial deformation of the reoriented $\langle 110 \rangle / \{111\}$ nanowires was performed both with and without Nosé-Hoover thermostatting; the thermostatting is utilized to model isothermal deformation by idealized heat transfer to a surrounding medium, while simulations without thermostatting model adiabatic deformation. These heat transfer conditions were chosen to as transient heat transfer effects have been shown to have a significant effect on the pseudoelastic behavior of polycrystalline SMAs [117, 126]. For the remainder of the paper, the thermostatted simulations will be referred as isothermal, while the non-thermostatted simulations will be referred to as adiabatic.

III.2.3 Simulation results and discussions

$\langle 100 \rangle$ to $\langle 110 \rangle / \{111\}$ reorientation

The section will first illustrate the $\langle 100 \rangle$ to $\langle 110 \rangle / \{111\}$ reorientation at 500 K. While this reorientation has been documented by many researchers [6, 50, 85–88], illustration here will be on the process leading to the formation of the $\langle 110 \rangle / \{111\}$ nanowires with interior defects. This reorientation process is driven by intrinsic surface stresses that allow the $\langle 100 \rangle$ nanowire to reduce its surface energy by reorienting to a $\langle 110 \rangle$ orientation with low energy $\{111\}$ side surfaces. The reorientation process from $\langle 100 \rangle$ to $\langle 110 \rangle / \{111\}$ configuration is illustrated in Figures (24) and (25), which illustrate the reorientation process leading to $\langle 110 \rangle / \{111\}$ nanowires that do and do not contain interior defects. Both figures show side by side snapshots of the nanowire potential energy along with the atoms visualized using the centrosymmetry parameter [8], which is a measure of local atomic coordination; a value of zero indicates a bulk, full-coordinated atom while values increasingly greater than zero indicate the presence of lattice defects such as dislocations, stacking faults and twins.

The reorientation process leading to the $\langle 110 \rangle / \{111\}$ silver nanowire with parallel interior $\{111\}$ stacking faults is shown in Figure (24). As illustrated in Figure (24b), the reorientation occurs by spatially distributed twinning on different crystallographic variants. The interactions of the different twin boundaries results in the formation of parallel $\{111\}$ stacking in the interior of the wire as shown in Figure (24c). Upon completion of the reorientation in Figure (24d), the parallel $\{111\}$ stacking faults remain in the wire center, while additional twin-like defects exist at the ends of the wire. These defects exist due to the fact that the ends of the wire are constrained to move only in the z-direction during reorientation in order to assure a clean tensile loading plane, and have been in previous simulations to propagate as twin boundaries to allow reversibility upon tensile loading to the initial, undeformed $\langle 100 \rangle$ orientation [88].

The reorientation process leading to the $\langle 110 \rangle / \{111\}$ silver nanowire containing

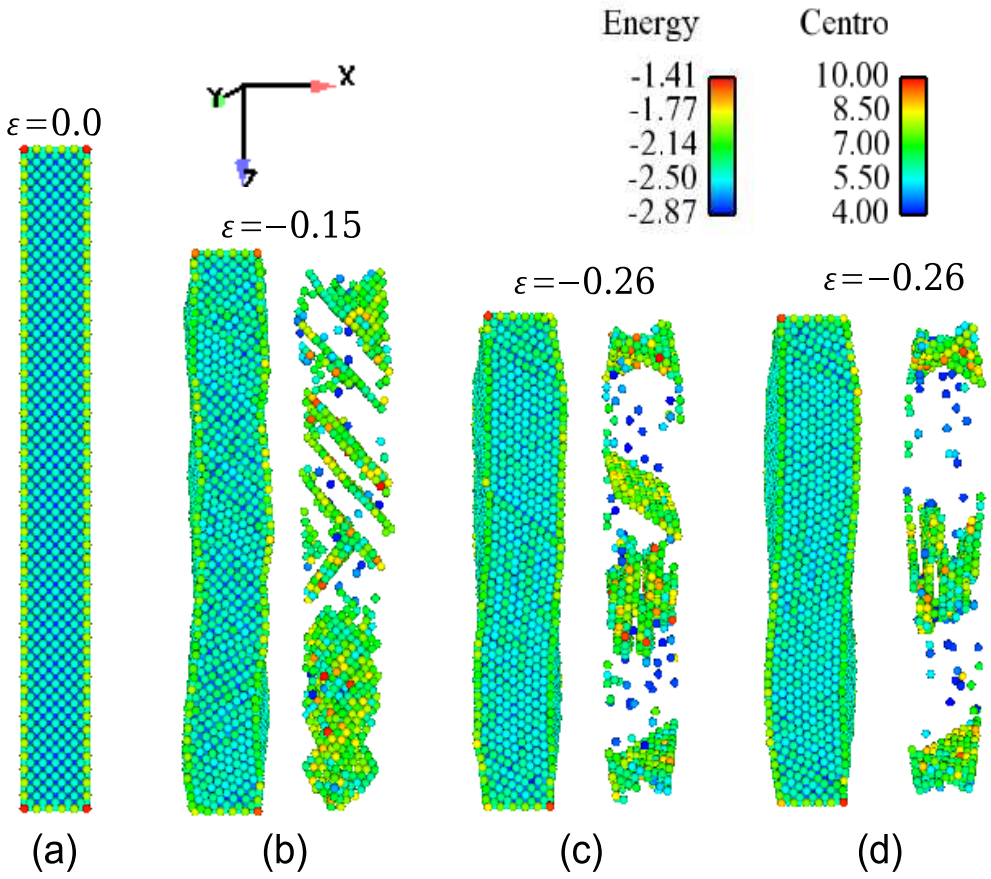

Figure 24: The reorientation of an initially defect-free ⟨100⟩ silver nanowire to a ⟨110⟩/{111} orientation containing interior parallel {111} stacking faults at 500K. Potential energy units are in eV, while centrosymmetry is defined in [8].

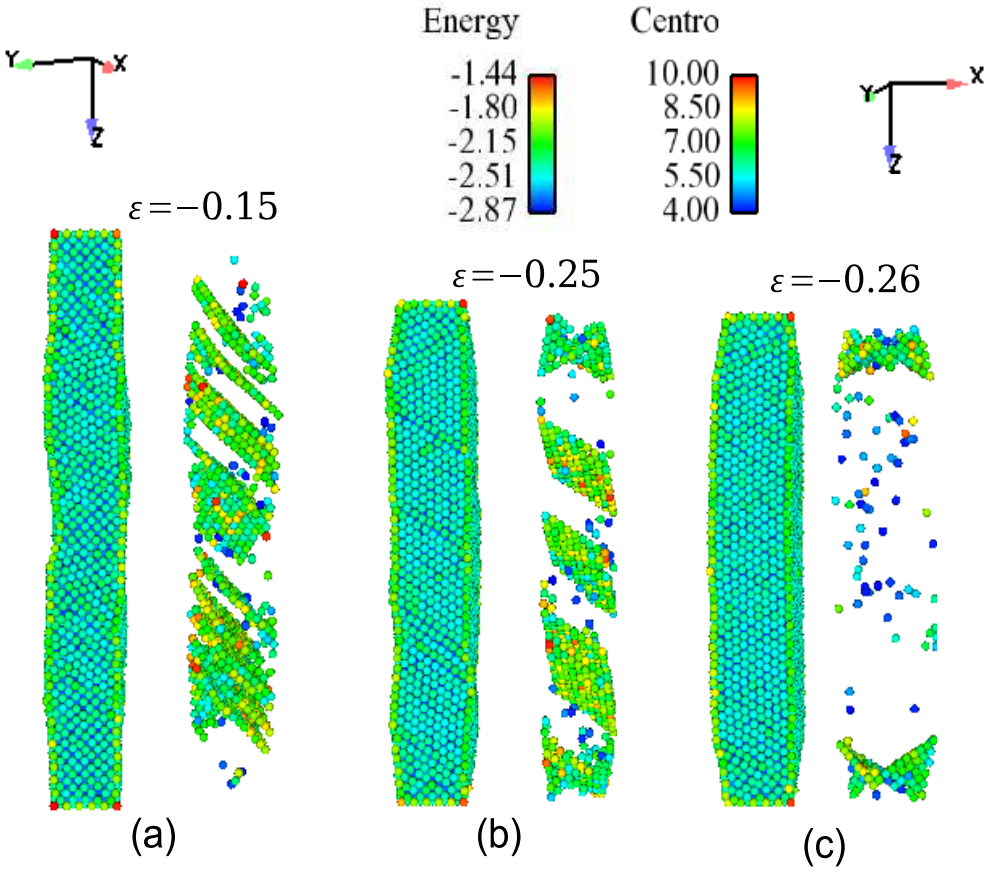

Figure 25: The reorientation of an initially defect-free ⟨100⟩ silver nanowire to a ⟨110⟩/{111} orientation free of interior defects at 500K. Potential energy units are in eV, while centrosymmetry is defined in [8].

only the twin boundaries at the ends of the wire is illustrated in Figure (25). Again, the compressive motion induced by the tensile surface stresses causes reorientation via spatially distributed twinning, though on the same crystallographic variants as illustrated in Figures (25a) and (25b). Of note in both reorientation processes illustrated in Figures (24) and (25) is that the interior of the twins are largely defect-free; this confirms earlier investigations [50] indicating that the formation of defect-free twins is key to allowing reversibility between $\langle 110 \rangle / \{111\}$ and $\langle 100 \rangle$ orientations. The final step in the reorientation is illustrated in Figures (25b) and (25c), which show that the remaining twin boundaries are removed by creation of ideal $\{111\}$ surfaces, resulting in a $\langle 110 \rangle / \{111\}$ wire without interior stacking faults.

A comparison between the defective and defect-free reoriented $\langle 110 \rangle / \{111\}$ nanowires after further annealing to 30K is shown in Figure (26). As can be seen, the defective $\langle 110 \rangle / \{111\}$ nanowire shows individual surface defects along with the interior $\{111\}$ stacking faults. It is noted that in the present examples, the defective and defect-free $\langle 110 \rangle / \{111\}$ nanowires were obtained simply by small variations in the Nosé-Hoover frequency parameter, which caused the variations in twinning leading to the formation of interior $\{111\}$ stacking faults seen in Figure (24).

While the differences in the $\langle 110 \rangle / \{111\}$ nanowires were generated through small variations in numerical modeling, there are many practical situations in which variations in applied heat or energy could cause initial defects as shown in Figure (24). For example, if reorientation from $\langle 100 \rangle$ to $\langle 110 \rangle / \{111\}$ is initiated by application of heat, a non-uniform application of the heat source could activate different twin planes and systems along the nanowire. In addition, if the shape memory nanowires are utilized as reinforcing materials within a nanocomposite, surface defects due to interactions with the matrix material could also adversely affect an idealized reorientation to a defect-free $\langle 110 \rangle / \{111\}$ orientation. Because these shape memory nanowires are therefore likely to be utilized in situations where they are not completely defect-free,

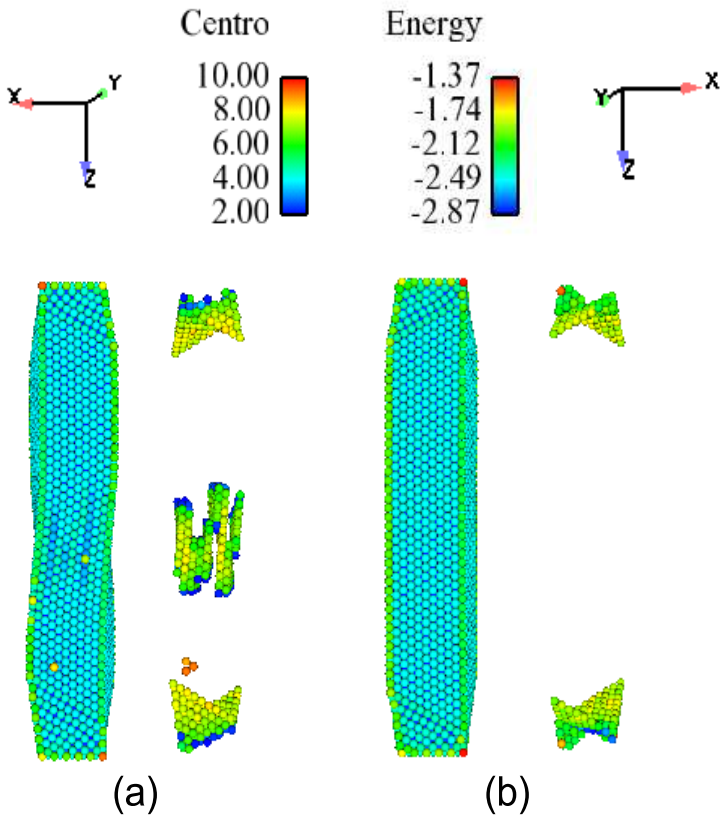

Figure 26: The comparison of defected and defect-free nanowires at $\langle 110 \rangle / \{111\}$ orientation at 30K, which is the initial configuration prior to uniaxial loading. Units of potential energy is eV, centrosymmetry is defined in [8].

the next section will proceed to investigate the potentially deleterious effects existing defects have on their mechanical performance.

Uniaxial tensile deformation of defective $\langle 110\rangle/\{111\}$ silver nanowires

Uniaxial deformation at 30K

In this section, the results of the MD simulations of the uniaxial tensile loading for the defective silver nanowires are discussed. The loading was performed across three decades of applied strain rates for three different temperatures considering both idealized adiabatic and isothermal heat transfer conditions. Strain is defined as $\epsilon = \frac{l-l_0}{l}$, where l_0 is the length of reoriented $\langle 110\rangle/\{111\}$ defected silver nanowire, l is current length of the nanowire during loading. Stresses reported in the simulation are based on virial theorem, which takes the form

$$\sigma_{ij} = \frac{1}{V}\left(\frac{1}{2}\sum_{\alpha=1}^{N}\sum_{\beta\neq\alpha}^{N} U'(r^{\alpha\beta})\frac{\Delta x_i^{\alpha\beta}\Delta x_j^{\alpha\beta}}{r^{\alpha\beta}} - \sum_{\alpha=1}^{N} m_\alpha \dot{x}_i^\alpha \dot{x}_j^\alpha\right) \tag{41}$$

where V is the current volume of silver nanowires, N is the total number of atoms, $\dot{x}_i^\alpha$ is the i th component velocity for atom α, m_α is the mass of atom α, $r^{\alpha\beta}$ is the distance between two atoms α and β, $\Delta x_j^{\alpha\beta} = x_j^\alpha - x_j^\beta$, U is the potential energy function and $r^{\alpha\beta} = \|\Delta x_j^{\alpha\beta}\|$. The average over the current volume in (43) implies that the stresses discussed in this work are global values based on the entire nanowire length. Recent discussions on methods of obtaining continuum stresses from atomistic data were detailed in [115, 116].

Figure (27) is presented as an illustration of the stress-induced reorientation from $\langle 110\rangle/\{111\}$ to $\langle 100\rangle$ that is possible even if the $\langle 110\rangle/\{111\}$ nanowire is initially defective. The applied strain rate is $\dot{\epsilon} = 10^8$ and the wire is loaded adiabatically at 30K. Upon application of tensile loading, the $\{111\}$ stacking fault in the middle of the wire first reorients into two separate twin boundaries as illustrated in Figure(27b). Concurrently, the twin-like defects at the wire ends reorient into two distinct twin boundaries and propagate towards the newly formed twin boundaries from stacking

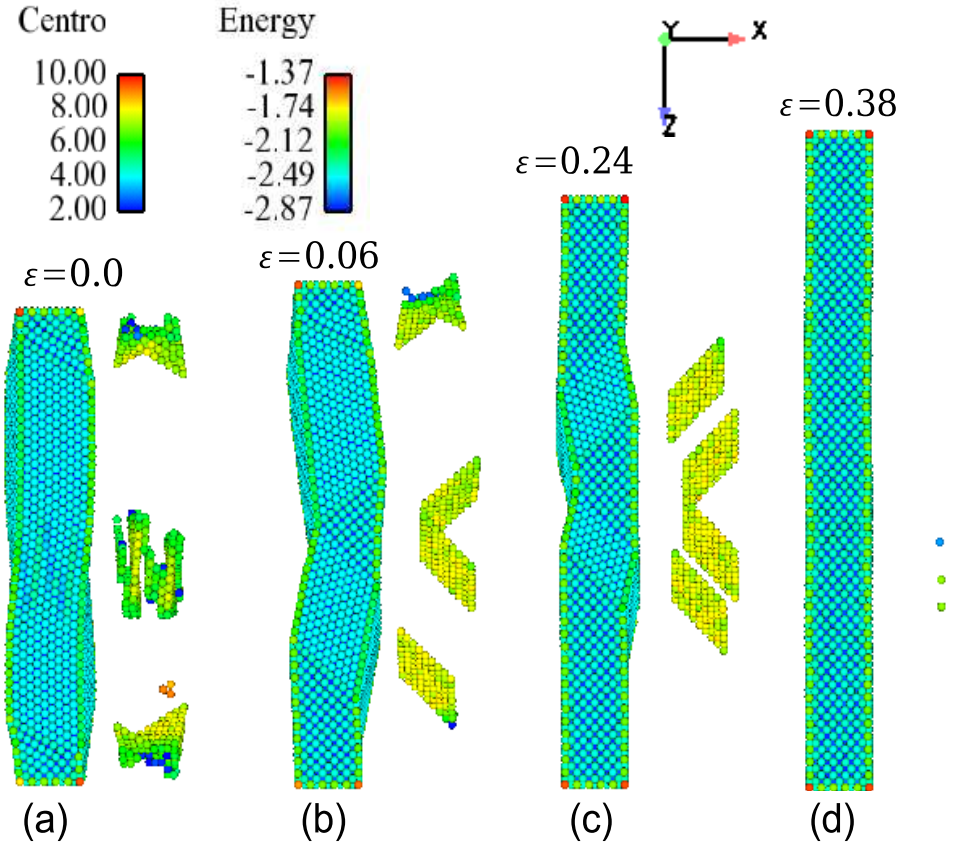

Figure 27: Stress-induced reorientation from ⟨110⟩/{111} at zero strain to initial ⟨100⟩ orientation at about 38 percent strain for adiabatically loaded silver nanowire at $\dot{\epsilon} = 10^8$. Units of potential energy are in eV, centrosymmetry is defined in [8]

.

fault as shown in Figure (27c). At this point in the deformation, the interior of the twins have a ⟨110⟩ orientation with {111} side surfaces; outside the twin boundaries, the wire has its initial ⟨100⟩ orientation with {100} side surfaces. At a strain of ϵ=0.38 with respect to initial ⟨110⟩/{111} nanowire, the two sets of twins annihilate each other and the nanowire regains its initial, defect-free ⟨100⟩ orientation as seen in Figure (27d).

A unique feature of the deformation in this defective nanowire seen in Figure (27) is the formation and propagation of two distinct twins within the nanowire inte-

rior, which is in contrast to the single twin boundary propagation seen in defect-free nanowires. Previous investigations into the uniaxial deformation of defect-free silver nanowires found that the propagation of multiple twins was seen only in extremely high strain-rate loading conditions at low temperatures [88], indicating that such deformation performs as a way of relieving the local material instability. In addition, the propagation of multiple twins in defect-free wires was seen to result in higher transformation stresses and subsequent plateau stresses driven by the increased stress necessary to propagate the multiple twin boundaries.

In this work, the transformation stress is defined as the maximum stress during the initial period of linear elastic deformation, while the plateau stress is defined as the stress state present in the wire immediately following the transformation stress as the reorientation from $\langle 110 \rangle / \{111\}$ to $\langle 100 \rangle$ proceeds via the propagation of the twin boundaries. Due to the non-constant plateau stresses seen in this work, the plateau period is loosely defined as ending at about $\epsilon = 0.30$. In terms of the active deformation mechanisms illustrated in this work, the transformation stress corresponds to the stress level at which the initial $\{111\}$ stacking faults in the defective nanowires orient themselves favorably under the applied uniaxial loading to form the appropriate twin boundaries.

The stress curves for the defective nanowire at 30 K under both adiabatic and isothermal loading conditions across three decades of strain rates are shown in Figure(28). The curves illustrate many interesting features particular to the tensile deformation of the $\langle 110 \rangle / \{111\}$ nanowires with initial $\{111\}$ stacking faults, which will be discussed next.

The first phenomena that we will discuss deals with the fact that, for both adiabatic and isothermal deformation, we do not observe a flat stress plateau following the transformation stress as typically exists in polycrystalline SMAs [117, 135], and was observed in the uniaxial tensile deformation of defect-free $\langle 110 \rangle / \{111\}$ shape

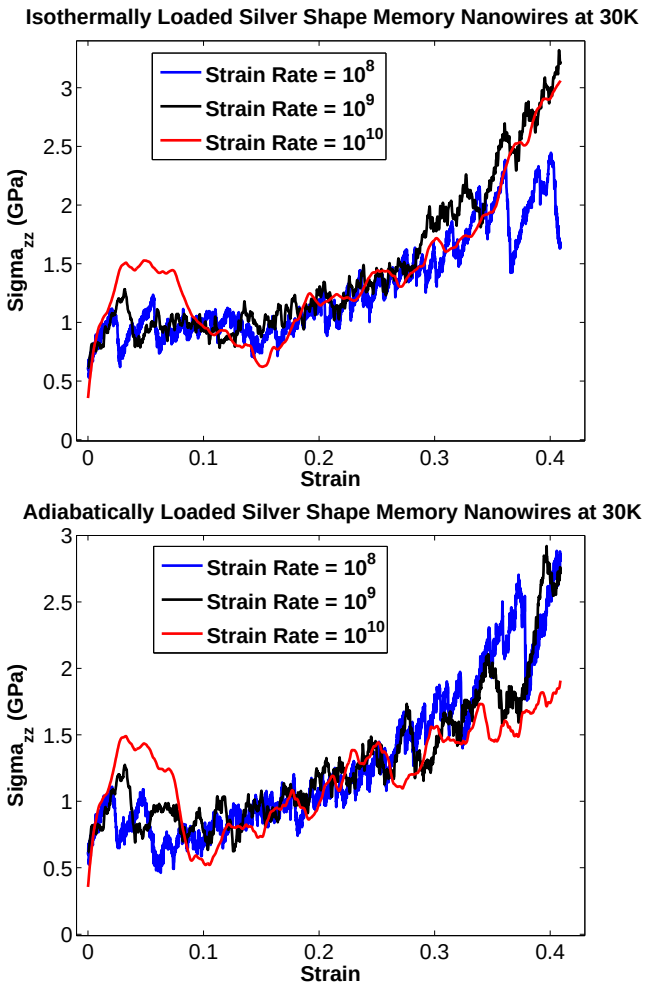

Figure 28: The uniaxial stress-strain relationship under various loading rates for silver shape memory nanowires at 30 K. (a) Isothermal. (b) Adiabatic.

memory nanowires [88]. In polycrystalline SMAs, the flat stress plateau following the transformation stress occurs while favorably oriented austenite grains transform under applied loading to martensite. In defect-free shape memory nanowires, the flat stress plateau occurs after a sufficiently high stress state (the transformation stress) is reached whereby the twin boundaries at the ends of the wire as illustrated in Figure (25) begin to propagate.

In the $\langle 110 \rangle / \{111\}$ nanowires with initial $\{111\}$ stacking faults, multiple twins initiate and propagate as seen in Figure (27b-c). Due to the presence of the twin boundaries, long-ranged stress fields exist in the nanowire. The propagation of the multiple twin boundaries causes interaction of the stress fields, and results in a non-constant and increasing stress level necessary to propagate the multiple twin boundaries. This is observed in Figure (28), which illustrates that from a strain level of about $\epsilon = 0.1$, the plateau stress is non-constant and increasing for the adiabatically loaded wires, while a similar transition occurs at a strain level of about $\epsilon = 0.15$ in the isothermally loaded wires. The later increase in plateau stress in the isothermal case is due to difficulties in untangling the $\{111\}$ stacking fault structure in the wire interior. The slope of the stress-strain curve increases markedly at higher strains due to the stress needed to annihilate and drive together the twin boundaries; this is most evident for the isothermally loaded nanowires beginning at a strain level of about $\epsilon = 0.30$ in Figure (28a).

This conclusion has been drawn by comparing the present results to stress-strain curves of the tensile deformation of defect-free $\langle 110 \rangle / \{111\}$ shape memory nanowires, in which the plateau stress remains constant across a range of deformation temperatures and heat transfer conditions to strain levels of 25 to 30 percent while the single twin boundaries propagate towards each other [88]. The stress in the defect-free wires begins to increase once the stress fields due to the boundaries of the single propagating twin begin to interact. The interaction culminates with the annihilation of the

twin boundaries, and the twin boundary interaction/annihilation process results in a nearly monotonically increasing stress strain-response. Because of the single twin system propagating in the defect-free wires, the plateau stress remains constant for a larger duration of time, thus explaining the difference in observed stress-strain response between defective and defect-free $\langle 110 \rangle / \{111\}$ shape memory nanowires loaded under tension.

A second point of interest is related to one of the major purposes for initiating this work, which is to determine whether the existence of initial defects within the $\langle 110 \rangle / \{111\}$ nanowires prevents complete reorientation back to the original $\langle 100 \rangle$ orientation. As can be seen in Figure (28) for the 30 K cases, most wires considered were able to reorient back to the defect-free $\langle 100 \rangle$ orientation. Two exceptions were seen: the wire loaded isothermally at a strain rate of $\dot{\epsilon} = 10^8$ and the wire loaded adiabatically at a strain rate of $\dot{\epsilon} = 10^{10}$. As will be shown later in this work, the wires loaded at lower temperatures and strain rates are more likely to reorient back to the $\langle 100 \rangle$ configuration at lower temperatures.

For those $\langle 110 \rangle / \{111\}$ nanowires with initial defects that were able to reorient back to the defect-free $\langle 100 \rangle$ orientation, the mechanical properties are nearly identical to those seen in the defect-free $\langle 110 \rangle / \{111\}$ case. For example, the stress in the wires when the $\langle 100 \rangle$ orientation is reached exceeds 3 GPa in the isothermal cases at 30 K, and is slightly below 3 GPa in the adiabatic cases, similar to what was previously observed for defect-free wires [88]. The transformation stresses and strains are reduced for the initially defective wires; this will be discussed in detail in the next section.

The thermal softening observed in the tangent moduli in Figure (28) after the plateau stress raises an interesting and enlightening comparison of nanowire shape memory behavior and bulk, polycrystalline shape memory behavior. In polycrystalline SMAs, the shape memory effect occurs due to a phase transformation between the low temperature martensite phase and the high temperature austenite phase.

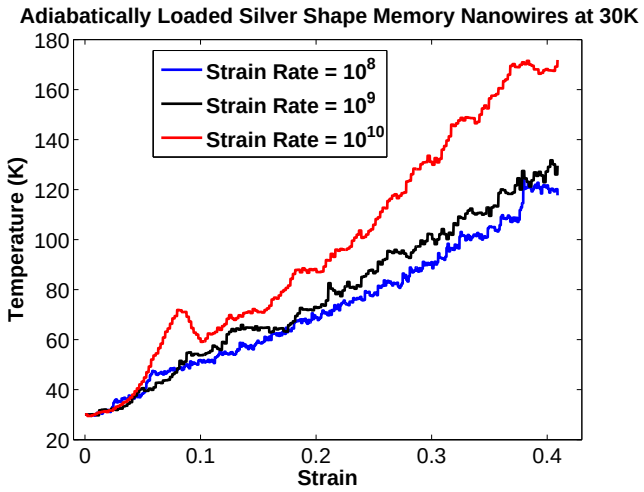

Figure 29: Evolution of temperature for three decades of applied strain rates in adiabatically loaded silver shape memory nanowires at an initial temperature of 30 K.

Because the austenite phase is stable at high temperatures, raising the deformation temperature requires more stress to induce and propagate the martensitic phase transformation due to the fact that the material is closer to stability in the austenite phase.

For the adiabatic loading shown here, the temperature increases dramatically during the deformation as illustrated in Figure (29). In addition, it has been documented that a critical temperature T_c is required to reorient the $\langle 100 \rangle$ nanowire to the $\langle 110 \rangle / \{111\}$ wires that are uniaxially loaded in this work. Thus, it would appear that shape memory nanowires should behave similarly to polycrystalline SMAs in that at the higher nanowire temperatures that result due to the adiabatic loading conditions, the stresses in the nanowires should increase to offset the increased tendency of the nanowire to revert back to the lower energy $\langle 110 \rangle / \{111\}$ orientation. However, as shown in Figure (28), the stress when the initial $\langle 100 \rangle$ orientation is reached is still lower than when the nanowire is loaded isothermally. It thus appears that at the nanoscale, thermal fluctuations which draw the lattice structure away from an idealized crystalline state have a much stronger effect on the resulting nanowire me-

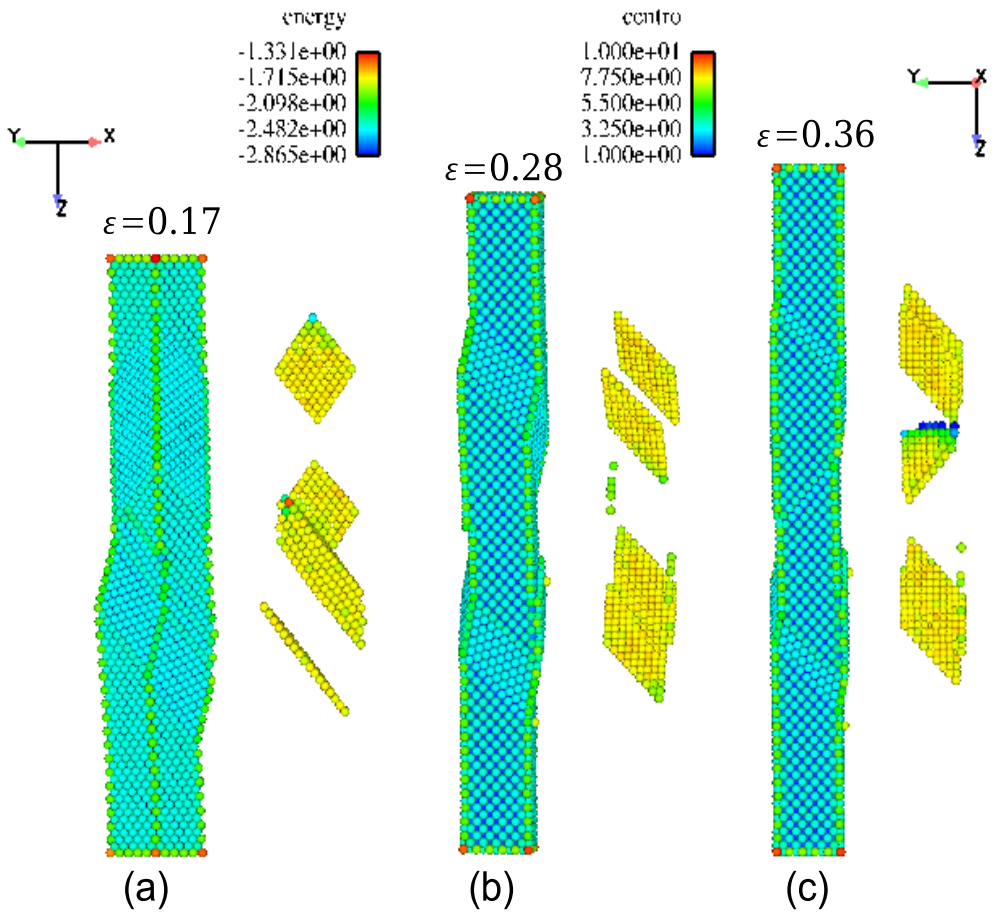

Figure 30: Stress-induced reorientation from $\langle 110 \rangle / \{111\}$ at zero strain to $\langle 100 \rangle$ orientation at 30 K for isothermally loaded silver nanowires at $\dot{\epsilon} = 10^8$. Units of potential energy are in eV, centrosymmetry is defined in [8].

chanical strength and properties than energetic considerations drawing the nanowire to various crystallographic orientations.

For completeness, an example will be illustrated and discussed on the deformation history for one of the $\langle 110 \rangle / \{111\}$ nanowires with initial defects that did not completely reorient back to the $\langle 100 \rangle$ configuration. As shown in Figure (28a), the isothermally loaded nanowire at a strain rate of $\dot{\epsilon} = 10^8$ experiences a sharp drop in stress at a strain of ϵ=0.37 just prior to reorienting back to the $\langle 100 \rangle$ configuration. The mechanisms controlling this stress drop is detailed by showing snapshots of the deformation in Figure (30).

The first noticeable variation in deformation mechanism is seen in Figure (30a), which illustrates that one of the twin boundaries has anomalously formed with multiple parallel stacking faults, instead of a single faulted boundary as was seen in Figure (27). Upon continued tensile deformation, two of the parallel stacking faults comprising the twin boundary have been annihilated as seen in Figure (30b). However, the result of this annihilation is a surface step due to a full dislocation, also seen in the middle of the nanowire in Figure (30b). While the twin boundaries continue to be pushed together at higher levels of strain, the full dislocation constitutes an irreversible lattice defect which prevents a defect-free reorientation back to the $\langle 100 \rangle$ configuration. Upon further loading, the surface step serves as a preferred nucleation site for partial $\{111\}/\langle 112 \rangle$ dislocations, thus causing irreversibility and preventing complete reorientation back to the initial $\langle 100 \rangle$ orientation.

At the highest loading rates of $\dot{\epsilon} = 10^{10}$, the adiabatically nanowires at 30 K show deviations in the stress response before the $\langle 100 \rangle$ orientation is reached, while no such deviations occur under isothermal loading. Under adiabatic deformation, the two sets of twins propagate towards each other under applied loading. However, just before defect-free reorientation back to $\langle 100 \rangle$ can occur, stacking faults on different variants appear surrounding the twin boundaries. The appearance of the stacking faults reduces the load carrying capability of the nanowires, and prevents defect-free reorientation back to the $\langle 100 \rangle$ configuration.

Uniaxial deformation at elevated temperatures

In this section, the response of defective $\langle 110 \rangle/\{111\}$ nanowires under uniaxial tension at elevated temperatures is discussed in comparison to the 30 K cases. Similar to the nanowires at 30 K, these nanowires were tested under various loading rates and heat transfer conditions for a given deformation temperature. The similarities and differences between the thermomechanical behavior of the $\langle 110 \rangle/\{111\}$ nanowires with initial defects at elevated temperatures as compared to lower temperatures are

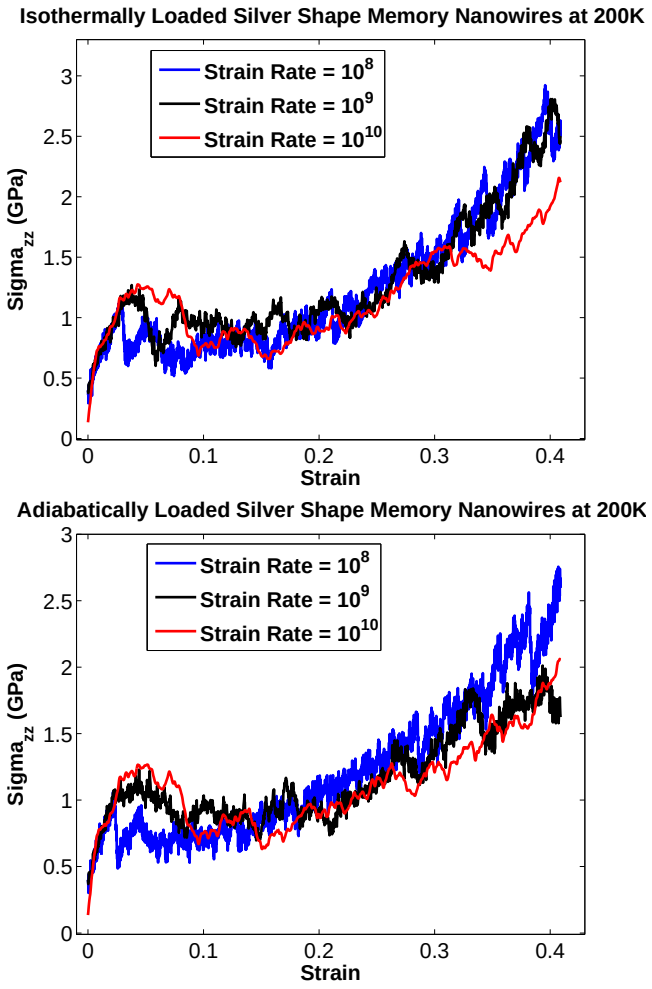

Figure 31: The uniaxial stress-strain relationship under various loading rates for silver shape memory nanowires at 200 K. (a) Isothermal. (b) Adiabatic.

best illustrated by considering the stress-strain responses, which are shown in Figures (31) and (32).

The major similarities as compared to the mechanical behavior at lower temperatures are the increasing and non-constant plateau stress as a function of strain, and the thermally-induced softening of the reorientation stress, or the stress level in the nanowires after the reorientation to the $\langle 100 \rangle$ configuration has been completed. The increasing plateau stress occurs for the same reason as previously discussed, i.e. due to the propagation and interaction of multiple twins within the nanowire. The re-

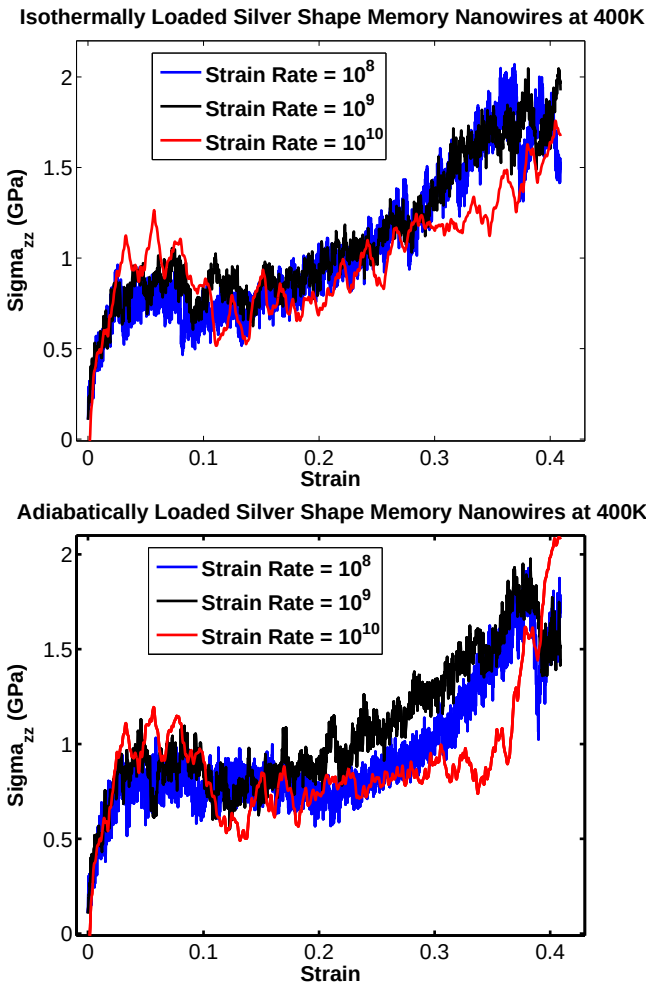

Figure 32: The uniaxial stress-strain relationship under various loading rates for silver shape memory nanowires at 400 K. (a) Isothermal. (b) Adiabatic.

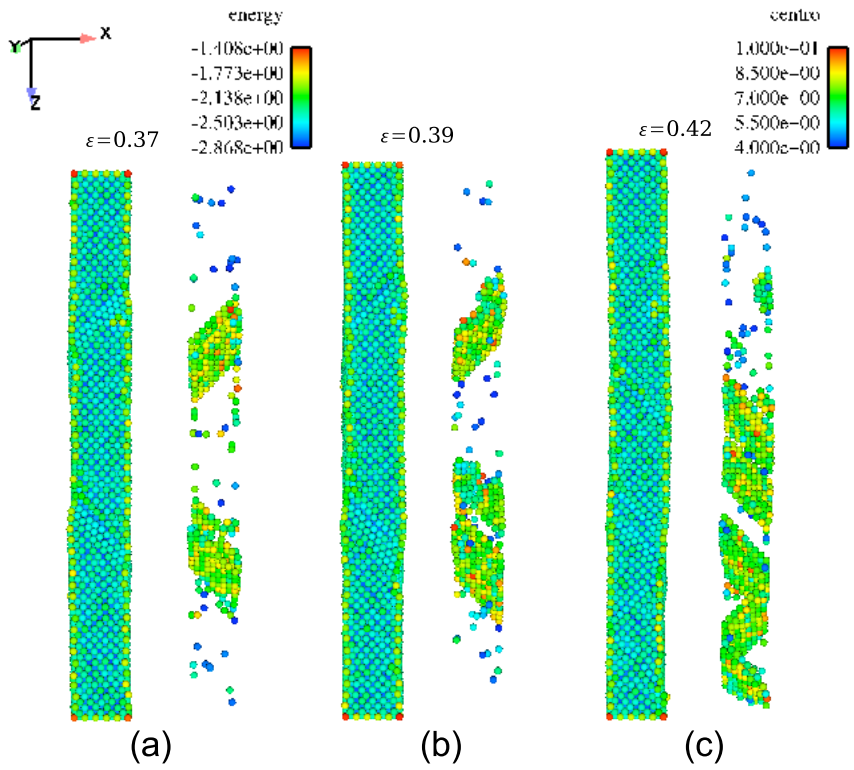

Figure 33: Adiabatic tensile loading of an initially defective $\langle 110 \rangle / \{111\}$ nanowire at 400 K and a strain rate of $\dot{\epsilon} = 10^9$ in which defect-free reorientation to $\langle 100 \rangle$ does not occur. Units of potential energy are in eV, centrosymmetry is defined in [8].

duced reorientation stress occurs similarly due to thermal softening effects on the overall mechanical strength.

One important difference at 400 K is that none of the initially defective $\langle 110 \rangle / \{111\}$ nanowires, regardless of applied strain rate or heat transfer condition, are able to complete a defect-free stress-induced reorientation back to the initial $\langle 100 \rangle$ configuration. The cause for this is illustrated in Figure (33). At 400 K, the reorientation generally proceeds with multiple twin boundaries propagating under applied uniaxial loading, and reaches a state just before twin boundary annihilation should occur, as illustrated in Figure (33a). At this point, partial dislocations propagate through the wire leaving trailing stacking faults, as observed in Figure (33b). One of the twins may eventually annihilate, as does the upper twin in Figure (33c), but the other remains

and additional partial dislocations propagate through the wire, preventing defect-free reorientation back to the initial ⟨100⟩ configuration. Because this occurs more frequently at elevated temperatures and strain rates, it is likely that reduced energetic barriers to defect nucleation in conjunction with surface defects are the cause for premature yielding before defect-free reorientation can occur.

Another difference is observed in the transformation stresses and strains at elevated temperatures versus those at lower temperatures, and also in comparison to the transformation stresses and strains observed in the defect-free wires; these are quantified graphically in Figures (34) and (35) for isothermally loaded defect-free and defective ⟨110⟩/{111} nanowires. Similar trends are seen in the adiabatically loaded wires. The first observable trend is that the transformation stresses and strains both tend to increase with increasing temperature for the initially defective ⟨110⟩/{111} nanowires. The reason for this is tied to the initial stress state in the wires due to the presence of the initial defects. As illustrated in Figures (28), (31) and (32), the stress in the initially defective ⟨110⟩/{111} wires is nonzero after thermal annealing. With increasing temperature, the initial stress in the wires gradually approaches zero. Therefore, while the transformation stress itself decreases with increasing temperature, the difference between the initial stress state and the transformation stress increases with temperature.

This fact also explains the increase in transformation strain with increasing temperature. That is, the increase in initial temperature allows the wire to accommodate the initial {111} stacking faults by thermally-induced expansion. Upon application of tensile loading, the wire is then allowed to deform elastically for a longer period of time before the stress state in the wire reaches the critical transformation value, causing the initial stacking faults to reorient into propagating twin boundaries. In this sense, the behavior of the ⟨110⟩/{111} nanowires with initial defects is similar to that observed in polycrystalline SMAs, in which the transformation stresses and strains

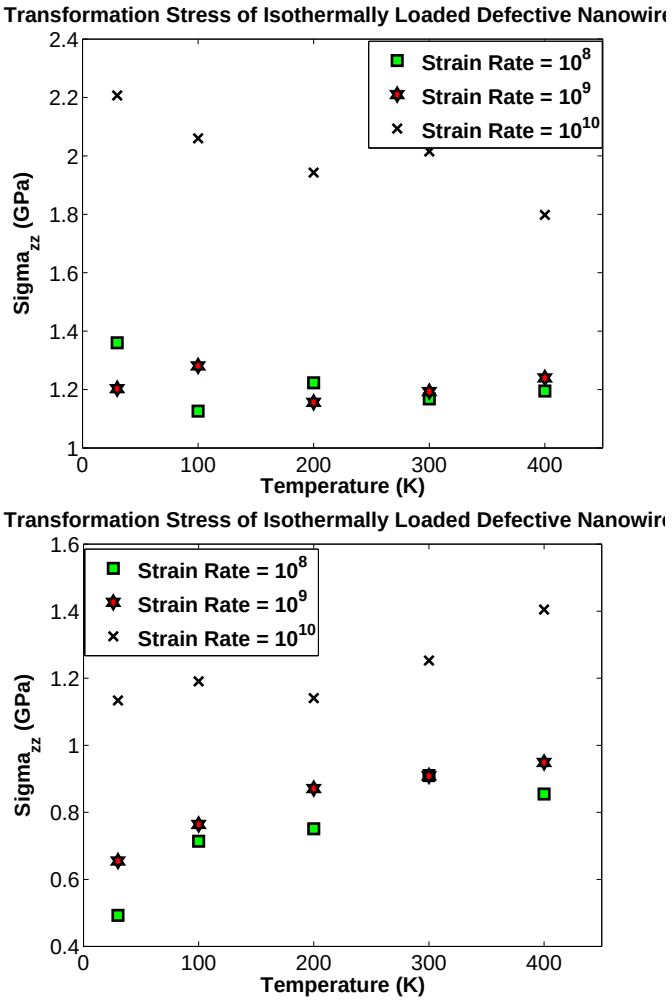

Figure 34: Summary of transformation stresses as a function of temperature for: (a) Defect-free $\langle 110 \rangle / \{111\}$ nanowires. (b) $\langle 110 \rangle / \{111\}$ nanowires with initial $\{111\}$ stacking faults.

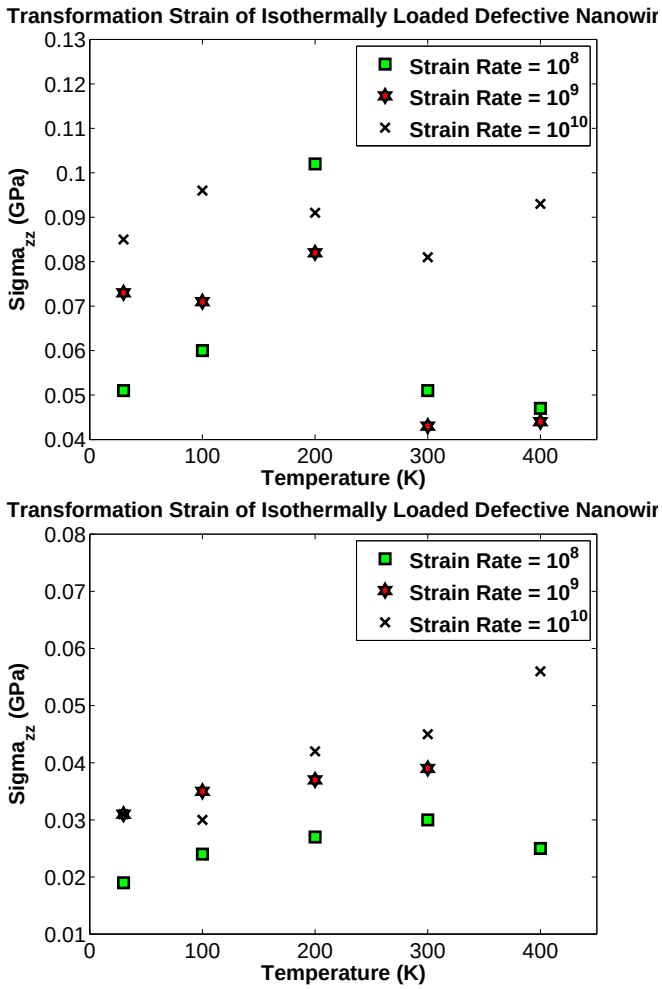

Figure 35: Summary of transformation strains as a function of temperature for: (a) Defect-free $\langle 110 \rangle / \{111\}$ nanowires. (b) $\langle 110 \rangle / \{111\}$ nanowires with initial $\{111\}$ stacking faults.

are observed to increase with increasing temperature. The initial stacking faults then serve as idealized grain boundaries, which require additional work to transform into propagating twins to initiate the stress-induced reorientation.

In contrast, as illustrated in Figure (34a), the transformation stress for the defect-free $\langle 110 \rangle / \{111\}$ nanowires appears to decrease or remain constant with temperature for most cases, again indicating thermal softening effects on reducing the amount of idealized deformation that is supportable in the nanowires. The transformation strains for the defect-free wires also show patterns of inconsistency, particularly at temperatures approaching the critical temperature for the $\langle 100 \rangle$ to $\langle 110 \rangle / \{111\}$ reorientation; see Figure (35a). Despite these trends, we note that for a given temperature and strain rate, the transformation stresses and strains for the defect-free wires were in all cases larger than those for the initially defective wires, indicating the effects of the initial defects in reducing these values.

Two unique situations are illustrated that were observed in the simulations, both at the critical reorientation temperature of 400 K. For the adiabatic nanowire with a loading rate of $\dot{\epsilon}$=10^8, the plateau period of the stress-strain curve shown in Figure (32b) exhibits a distinct difference from that of the $\dot{\epsilon}$=10^9 case. In particular, the plateau stress remains relatively constant until more than 20 percent strain, which is in stark contrast to the non-constant plateau stresses observed in the other defective nanowires. The reason for this is illustrated in Figure (36), which shows that upon application of tensile loading, the $\{111\}$ stacking faults do not reorient to form multiple twin boundaries. Instead, the stacking faults glide towards the fixed end of the nanowire, eventually interacting with the twin boundary at the fixed end and annihilating, resulting in the configuration seen in Figure (36d). Thus, this initially defective $\langle 110 \rangle / \{111\}$ nanowire instead behaves effectively as a defect-free nanowire.

The second unusual phenomenon is observed in the stress-strain curve for the adiabatic case with a loading rate of $\dot{\epsilon} = 10^{10}$. As shown in Figure (32b), the stress

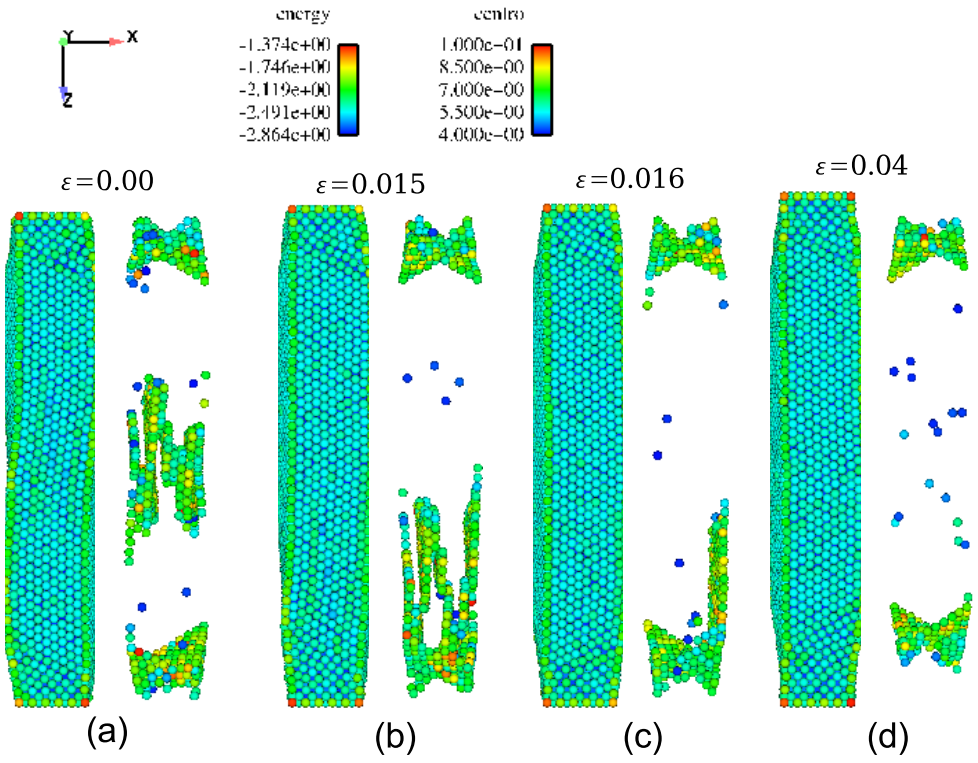

Figure 36: Stress-induced reorientation from $\langle 110 \rangle / \{111\}$ at zero strain to initial $\langle 100 \rangle$ orientation at 400 K for adiabatically loaded silver nanowires at a strain rate of $\dot{\epsilon} = 10^8$. Units of potential energy are in eV, centrosymmetry is defined in [8].

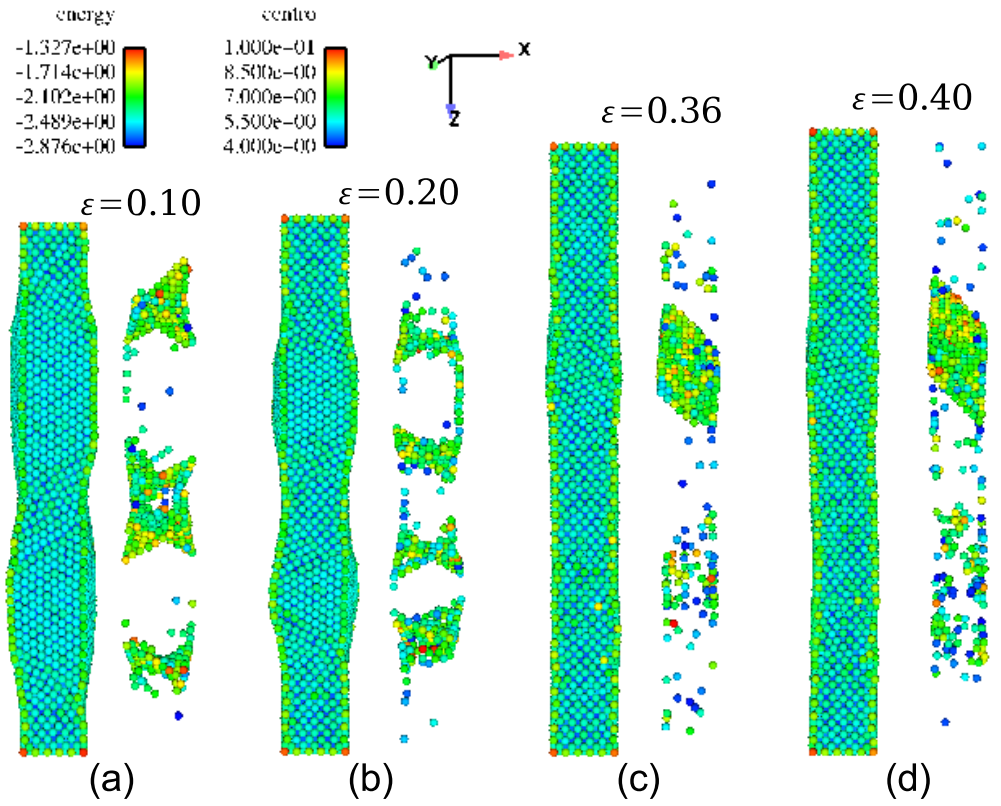

Figure 37: Stress-induced reorientation from $\langle 110 \rangle / \{111\}$ at zero strain to $\langle 100 \rangle$ orientation at 400 K for adiabatically loaded silver nanowires at a strain rate of $\dot{\epsilon} = 10^{10}$. Units of potential energy are in eV, centrosymmetry is defined in [8].

for the $\dot{\epsilon} = 10^{10}$ case has an extended flat stress plateau as compared to the cases with lower loading rates; the stress then increases sharply starting at a strain level of $\epsilon = 0.35$. Snapshots of the corresponding deformation are shown in Figure (37). In this case, the initial $\{111\}$ stacking faults do reorient to form the two twin boundaries, as seen in Figure (37b). However, at a strain level of $\epsilon = 0.36$ as seen in Figure (37c), one twin boundary has been annihilated while the other has formed a complex, multi-layered stacking fault structure. It is found that additional stacking faults form within the upper twin boundary, thus reducing the overall stress in the nanowire and contributing to the elongated plateau stress seen in Figure (32b). The subsequent sharp increase in stress at $\epsilon = 0.35$ can be attributed to the increase in stress necessary to propagate the multi-layered stacking fault. This stacking fault structure eventually precludes a defect-free reorientation to the $\langle 100 \rangle$ configuration.

III.2.4 Discussion: overall impact of initial defects

The numerical results presented thus far concentrated on characterizing the thermomechanical properties of silver shape memory nanowires due to uniaxial tensile loading initiated from a $\langle 110 \rangle / \{111\}$ orientation with interior $\{111\}$ stacking faults. The simulation results can at this stage be generalized to state that at high strain rates such as $\dot{\epsilon} = 10^{10}$ and elevated temperatures nearing the critical reorientation temperature T_c, the nanowires are less likely to show complete reversibility under tensile loading between the $\langle 110 \rangle / \{111\}$ and $\langle 100 \rangle$ orientations.

Another interesting aspect of the deformation is that the stress state during the uniaxial tensile deformation when multiple twins propagate in the nanowires, as was observed throughout this work for the initially defective wires, is not higher than the stress observed in the uniaxial tensile deformation of the defect-free wires. The reason for this can be tied to the reduced velocities at which multiple twins propagate in a wire of the same length as compared to the velocity of a single propagating twin. As was eloquently explained by Shaw and Kyriakides [117], if more twins are propagating

in a material of a given length, the velocities of each set of twins must be reduced accordingly to accommodate the same amount of deformation. Therefore, while a larger stress is presumably required to propagate multiple twins as compared to the a single twin, the fact that the velocities of the propagating twins are reduced accounts for the non-elevated stress response for initially defective shape memory nanowires as compared to initially defect-free wires.

The simulation results have also revealed both similarities and differences in the tensile stress-strain responses of the initially defective and defect-free $\langle 110 \rangle / \{111\}$ nanowires. For example, the transformation stresses and strains were lower for all temperatures and loading rates for the initially defective wires. However, once the stress state in the wire had increased enough to initiate the propagation of multiple twins, the plateau stresses and the stress state in the wires when the original $\langle 100 \rangle$ orientation was reached is similar between initially defective and defect-free $\langle 110 \rangle / \{111\}$ nanowires. In addition, when irreversible deformation was observed to occur in the wires due to the formation of complex stacking fault structures at twin boundaries or full dislocations, the irreversibility occurred late in the reorientation process, typically after strains of 30 percent or larger with respect to the original $\langle 110 \rangle / \{111\}$ configuration. This result is quite encouraging, as most polycrystalline SMAs have reversible inelastic strains approaching about 10 percent [125].

This section will be closed with the discussion on two key issues which were not considered in this work. First, an issue not considered in this work, but which can be inferred from the results herein is the importance of stochastic effects in predicting the resulting mechanical properties of defective shape memory nanowires. The configuration chosen in this work, i.e. that of the reoriented $\langle 110 \rangle / \{111\}$ nanowire with internal $\{111\}$ stacking faults, was analyzed after considerable work studying the $\langle 100 \rangle$ to $\langle 110 \rangle / \{111\}$ reorientation, and finding the most typical configuration with defects to be that with interior $\{111\}$ stacking faults. Clearly, this single situation

does not account for all possible scenarios involving combinations of initial defects both within the nanowire and on the nanowire surfaces. However, it does serve to illustrate that with judicious selections of deformation temperature and applied strain rate, nanowires with initial defects can still reorient completely between the low energy $\langle 110 \rangle / \{111\}$ and higher energy $\langle 100 \rangle$ orientations, thus paving the way for shape memory behavior and relevant applications at the nanoscale.

Finally, another key issue which was not considered in the present work but has important implications for practical usage of metal nanowires is that of oxidation. In the future, it will be important to investigate, perhaps using first principles techniques for accuracy, the effects of oxidation layers on the deformation behavior and properties of metallic nanowires and nanostructures.

CHAPTER IV

GEOMETRIC EFFECTS ON THE ELASTICITY OF HOLLOW METAL NANOWIRES

The purpose of this chapter is to characterize the elastic properties of hollow metal nanowires (nanoboxes) and to relate the variation in the Young's modulus, yield stress, and yield strain to the amount of bulk material that is removed to create the nanoboxes. With atomistic simulations, it has been found that, while $\langle 100 \rangle$ nanoboxes show no improvement in elastic properties as compared to the corresponding solid $\langle 100 \rangle$ nanowires, $\langle 110 \rangle$ nanoboxes show enhanced elastic properties as compared to solid $\langle 110 \rangle$ nanowires. The simulations reveal that the elastic properties of the nanoboxes are strongly dependent on the relative strength of the bulk material that has been removed, as well as the total surface area of the nanoboxes, and indicate the potential of ultralight, high-strength nanomaterials such as nanoboxes. The discussions in this chapter are based upon the work of Ji and Park [92].

IV.1 Introduction

Most of the research on mechanical properties that has been performed on nanowires has concentrated on analysing the elastic and inelastic deformation and properties of solid wires with regular geometries, i.e. $\langle 100 \rangle$ wires with square cross sections. These efforts have resulted in a large collection of information quantifying nanowire mechanical properties for various loading conditions [25–27, 50, 52, 59, 60, 67, 69, 72, 74–76, 78, 79, 82, 85, 87, 91, 136, 137]; highlights include size-dependent elasticity [26, 27], phase transformations, shape memory and pseudoelastic behavior [25, 50, 87, 91], orientation-dependent deformation [74,82,85], amorphization at large strain rates [60,

75, 137], and many others.

However, as the ability to control the synthesis of nanostructures has increased in recent years, researchers have found that nanowires typically form in geometries that deviate from those previous studied [138]. In particular, many researchers have found that non-square cross section wires may be energetically favourable [73,139–146]; others have utilized novel techniques to synthesize hollow nanowires, or nanoboxes [140, 147, 148].

While the ability to synthesize nanostructures of varying size and shape is itself important and interesting, these nanostructures of novel geometry have attracted much interest as researchers have discovered that their geometry can be utilized to engineer unique behavior and properties. For example, geometry is known to have a large effect on the optical properties of metal nanoparticles [149]. More recent work has analyzed the optical properties of hollow metallic nanostructures [140,150]; it was found that the optical properties can be altered by hollowing out the nanostructure. From a perspective of mechanical behavior [151], recent atomistic simulations have indicated that both surface orientation [85] and the geometry of the nanowires [81] can have a first order effect on the mechanical behavior of FCC metal nanowires. Furthermore, $\langle 110 \rangle$ nanowires with non-square cross sections similar to those synthesized experimentally were found to have distinct deformation modes and mechanical properties as compared to square cross section wires [152].

In this work, atomistic calculations will be utilized to study the elastic properties of hollow metal nanowires, which is called nanoboxes. In doing so, it is found that while $\langle 100 \rangle$ nanoboxes are weaker than the corresponding $\langle 100 \rangle$ solid wires, $\langle 110 \rangle$ nanoboxes with a $\langle 110 \rangle$ orientation, which is the orientation that is most frequently observed experimentally [150], are stronger than the corresponding solid $\langle 110 \rangle$ wires. This chapter will also characterize yield stresses and strains for the nanoboxes, and compare those to the values of the corresponding solid wires. These results are con-

sistent with previous studies on solid nanowires [26, 27] that indicate that the bulk material can be either weaker or stronger depending on the orientation. In particular, the present results indicate that geometric considerations may lead to the development of lightweight nanomaterials that offer, in certain respects, superior elastic properties that may be beneficial for future nanoengineering applications.

IV.2 Simulation details

In this section, molecular statics simulations are performed on copper nanowires using the embedded atom method (EAM) [105, 108] as the underlying interatomic interaction model. In the EAM, the total energy U for a system of atoms is written as

$$U = \sum_{i}^{N} \left(F_i(\bar{\rho}_i) + \frac{1}{2} \sum_{j \neq i}^{N} \phi_{ij}(R_{ij}) \right), \tag{42}$$

where the summations in (42) extend over the total number of atoms N in the system, F_i is the embedding function, $\bar{\rho}_i$ is the electron density at atom i, ϕ_{ij} is a pair interaction function and R_{ij} is the distance between atoms i and j. In this work, copper nanowires are modeled with the EAM potential developed by Mishin *et al.* [111], which accurately represents the elastic properties and surface energies of copper.

The nanoboxes were created through a top-down approach by extracting them from a bulk copper FCC crystal. First, a solid wire was extracted, followed by removing atoms (the *bulk*) from the center of the wire leaving a square hole and thus a hollow nanobox. As illustrated in Figure (38), all nanowires and nanoboxes had the same length of 50 cubic lattice units (CLU), where 1 CLU=0.3615 nm for copper, while both $\langle 100 \rangle$ and $\langle 110 \rangle$ longitudinal orientations were considered. The nanobox cross section can be characterized with two parameters, the outer edge length l_o and

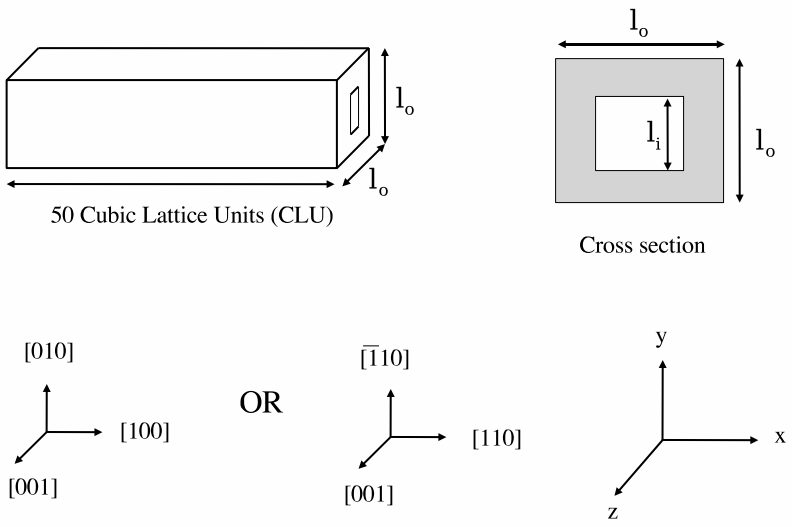

Figure 38: Schematic of the dimensions and axial orientations of the nanoboxes. Solid nanowires with square cross sectional length l_o and same axial orientations were also considered for comparative purposes.

Table 2: Cross sectional dimensions in terms of $l_o \times l_i$ for $\langle 100 \rangle$ copper nanoboxes of length 50 CLU. All dimensions are in CLU, where 1 CLU=0.3615 nm for copper. Equivalent solid wires of square cross sectional length l_o were also considered for comparative purposes.

	1	2	3	4	5
Constant $(l_o - l_i)/2$	12×2	14×4	18×8	20×10	25×15
Constant l_o	20×2	20×5	20×8	20×10	20×13
Constant l_i	14×5	16×5	20×5	22×5	24×5

Table 3: Cross sectional dimensions in terms of $l_o \times l_i$ for $\langle 110 \rangle$ copper nanoboxes of length 50 CLU. All dimensions are in CLU, where 1 CLU=0.3615 nm for copper. Equivalent solid wires of square cross sectional length l_o were also considered for comparative purposes.

	1	2	3	4	5
Constant $(l_o - l_i)/2$	13× 3	15×5	17×7	19×9	21×11
Constant l_o	17×3	17×5	17×7	17×9	17×10
Constant l_i	13×5	15×5	17×5	19×5	21×5

the inner edge length l_i as shown in Figure (38), while the nanobox wall thickness can be defined as $(l_o - l_i)/2$. The $\langle 100 \rangle$ nanoboxes contained only $\{100\}$ transverse surfaces, while the $\langle 110 \rangle$ nanoboxes contained both $\{100\}$ and $\{110\}$ transverse surfaces.

Solid $\langle 100 \rangle$ and $\langle 110 \rangle$ nanowires with the same length of 50 CLU square cross sections of length l_o were also studied for comparative purposes; by studying both nanoboxes and solid nanowires, the effects of removing the bulk material on the nanobox elastic properties will be quantified. Dimensions of the $\langle 100 \rangle$ solid wires and nanoboxes are given in Table (2), while the $\langle 110 \rangle$ solid wires and nanobox geometries are summarized in Table (3). The nanoboxes are grouped into three categories: constant wall thickness ($(l_o - l_i)/2$), constant outer edge length (l_o) and constant inner edge length (l_i).

The nanoboxes and solid wires were first relaxed to energy minimizing positions; due to the presence of tensile surface stresses [4], the nanowires and nanoboxes as

extracted from the bulk are not in equilibrium, and thus contract in the longitudinal direction. After the energy minimization, the wires and boxes were quasistatically loaded in tension by fixing one end, and elongating the other end using a strain increment of 0.1% while allowing relaxation of the atomic positions in the nanowire interior. The reported Young's modulus in each case was calculated by taking the slope of the stress-strain curve within the small strain regime, $\epsilon <= 0.3\%$.

This work will focus on characterizing the elastic properties of the nanoboxes using three parameters: the Young's modulus, yield stress and yield strain. The modulus is generally defined as the slope of the stress/strain curve for a material under uniaxial tension, and is perhaps the most valuable elastic property as it measures the resistance, or stiffness, of the material to imposed deformation. The yield values are important as they measure how much elastic deformation, in terms of elongation (yield strain), and applied deformation a material can sustain (yield stress) before undergoing irreversible plastic deformation, or yield.

The analysis will utilize engineering strain as the strain measure in this work, while the stresses were calculated using the virial theorem [115, 116], which takes the form

$$\sigma_{ij} = \frac{1}{V}\left(\frac{1}{2}\sum_{\alpha=1}^{N}\sum_{\beta\neq\alpha}^{N} U'(r^{\alpha\beta})\frac{\Delta x_i^{\alpha\beta}\Delta x_j^{\alpha\beta}}{r^{\alpha\beta}}\right) \tag{43}$$

where N is the total number of atoms, $r^{\alpha\beta}$ is the distance between two atoms α and β, $\Delta x_j^{\alpha\beta} = x_j^{\alpha} - x_j^{\beta}$, U is the potential energy function, $r^{\alpha\beta} = \|\Delta x_j^{\alpha\beta}\|$, and V is the current volume. The yield strain and yield stress were both found at the point of initial yield, or when the first defect which typically appears in the form of a partial dislocation nucleates within the nanobox or nanowire.

For a nanobox, the volume was approximated as the initial volume of the solid wire minus the volume of the removed interior; this approximation is viewed as acceptable due to the fact that the modulus values reported here are small strain values, and also because the nanobox geometry is largely undistorted before yield. Due to the

Table 4: Normalized surface area (first value) and volume (second value) of ⟨100⟩ nanoboxes in Table (2).

	1	2	3	4	5
Constant $(l_o - l_i)/2$	1.00/1.00	1.29/1.29	1.86/1.86	2.14/2.14	2.86/2.86
Constant l_o	1.00/1.00	1.11/0.95	1.21/ 0.85	1.27/0.76	1.36/0.58
Constant l_i	0.60/0.31	0.68/0.42	0.83/0.68	0.92/0.83	1.00/1.00

Table 5: Normalized surface area (first value) and volume (second value) of ⟨110⟩ nanoboxes in Table (3).

	1	2	3	4	5
Constant $(l_o - l_i)/2$	1.00/1.00	1.25/1.25	1.50/1.50	1.75/1.75	2.00/2.00
Constant l_o	1.00/1.00	1.08/0.94	1.16/0.86	1.23/0.74	1.27/0.68
Constant l_i	0.64/0.35	0.73/0.48	0.82/0.63	0.91/0.81	1.00/1.00

quasistatic nature of the simulations, there are no dynamic terms that are dependent on atomic velocities in (43). The simulation time, or computational cost, depends on the size of nanowires. The longest simulation time is around three days for the largest wire, while is around several hours for the small wires. The simulations were accomplished at two paralleled processors, Intel 2.0 GHz.

IV.3 Simulation results and discussions

This section presents simulation results obtained through the tensile loading of ⟨100⟩ and ⟨110⟩ copper nanoboxes, while comparing the results obtained from the tensile loading of the corresponding solid wires of cross sectional length l_o. Because the elastic properties of solid wires have been reported in various other publications [26, 27, 153, 154], this section will focus on the elastic properties of the nanoboxes, while normalizing the quantities by those of the corresponding solid wires.

As various nanobox geometries have been considered in this work, this chapter presents the nanobox modulus, yield stress and yield strain in terms of the VR/TV ratio, where VR is the volume of (bulk) atoms removed to create the nanobox, and

TV is the volume of the corresponding solid nanowire with cross sectional length l_o. This ratio was calculated for nanoboxes with constant outer edge length (l_o), inner edge length (l_i) and constant nanobox wall thickness ($(l_o - l_i)/2$), and is utilized as it allows us to quantify the effects of removing increasing amounts of bulk material on the nanobox elastic properties.

For nanoboxes with a constant wall thickness, an increasing VR/TV ratio indicates an identical increase in both l_o and l_i, though the surface area to volume ratio does not change. For nanoboxes with constant outer edge length l_o, an increase in the VR/TV ratio implies a decreasing wall thickness brought on by an increase of the inner edge length l_i, while an increasing VR/TV ratio for nanoboxes with constant inner edge length l_i corresponds to a decrease in wall thickness and outer edge length l_o. To enable future discussions on the effects of surface area and volume on the elastic properties of the nanoboxes, normalized values are presented for surface area size and volume for the nanoboxes considered in Tables (4) and (5).

IV.3.1 Modulus of $\langle 100 \rangle$ nanoboxes

Figure (39) illustrates both the actual and normalized modulus values for the $\langle 100 \rangle$ nanoboxes, which are plotted against the VR/TV ratio. Here, the values in Figure (39B) are normalized by the computed moduli of the corresponding solid nanowires of cross sectional length l_o.

Figure (39A) shows variations in the measured nanobox moduli as dependent on the variations in the three different geometries considered in this work. For constant l_o and l_i nanoboxes, the modulus decreases as more of the bulk material is removed. The decrease in strength is most dramatic for the case in which the inner length l_i is kept constant, while the outer length l_o is increased. Indeed, Figure (39A) indicates that the strongest effect on the modulus comes from altering the nanobox wall thicknesses through l_o or l_i. This effect occurs due to rapid changes in surface area to volume

ratio for the constant l_o or l_i. This effect occurs due to rapid changes in surface area to volume ratio for the constant l_o and l_i nanoboxes with varying VR/TV ratio, resulting in a varying contribution to the nanobox modulus from both the bulk and surface elastic stiffnesses.

Figure (39B) also shows variations in the nanobox modulus when normalized by the modulus for the corresponding solid wires with square cross section of length l_o. When comparing normalized values, it is clear from Figure (39B) that the $\langle 100 \rangle$ nanoboxes are elastically softer than the corresponding solid $\langle 100 \rangle$ nanowires for all nanobox geometries; furthermore, it is evident that as more bulk material is removed in creating $\langle 100 \rangle$ nanoboxes with increasing VR/TV ratio, all nanoboxes show a corresponding decrease in modulus.

These results make a great deal of sense when analyzed in the context of recent results on the relative elastic strength of bulk versus surfaces [26, 27]. In those works, it was found that as solid $\langle 100 \rangle$ wires were gradually made smaller and smaller, their elastic modulus decreased due to the fact that the $\langle 100 \rangle$ bulk is stiffer than the $\{100\}$ surfaces. The softening of the elastic properties as more bulk is removed thus matches those predictions [26, 27], and indicates that $\langle 100 \rangle$ nanoboxes will offer no stiffness enhancements as compared to the corresponding $\langle 100 \rangle$ solid wires.

Interestingly, the nanobox modulus increases slightly as seen in Figure (39A) if its wall thickness $((l_o - l_i)/2)$ is kept constant but its overall cross sectional length including both l_i and l_o, increases; this is unexpected as this implies that more bulk material is being removed to create the nanoboxes, which would, for the $\langle 100 \rangle$ orientation, imply a decrease in modulus. Figure (39B) thus shows that while the modulus of the constant wall thickness nanoboxes increases slightly with increasing cross sectional length, the rate of stiffness increase is still lower than that of the corresponding solid wires. While similar behavior is observed and understandable for the modulus of constant thickness $\langle 110 \rangle$ nanoboxes as discussed later, it is currently unclear as

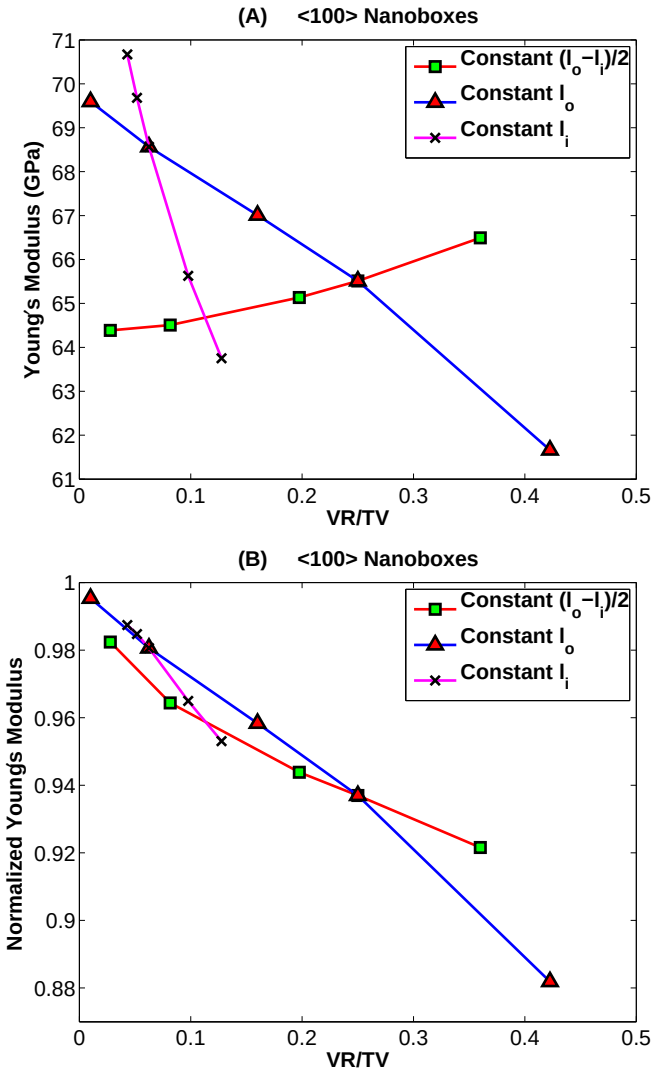

Figure 39: Variation in (A) Young's modulus and (B) Normalized Young's modulus for $\langle 100 \rangle$ nanoboxes with VR/TV.

to why the modulus of the constant thickness ⟨100⟩ nanoboxes increases with VR/TV.

IV.3.2 Yield stress and strain of ⟨100⟩ nanoboxes

The yield stresses and yield strains for the various ⟨100⟩ nanoboxes are plotted in Figure (40). As can be seen, for the nanoboxes with constant outer edge length l_o, both the yield stress and yield strain show a decreasing trend with increasing VR/TV ratio. The reason this occurs is because the increasing VR/TV ratio corresponds to decreasing the wall thickness by gradually increasing the inner edge length l_i. Decreasing the wall thickness corresponds to effectively removing more bulk material to create the nanoboxes; because the ⟨100⟩ bulk is stronger than the {100} surfaces, this as observed in Figure (39A) leads to a reduction in modulus.

The yield strain decreases as VR/TV increases for the constant l_o nanoboxes because this leads to an increase in the overall surface area of the nanoboxes, as seen in Table (4). This factor is critical because defects in surface-dominant nanomaterials such as nanowires tend to nucleate exclusively from surfaces, due to the fact that surfaces exist at an energetic equilibrium that is larger than that of the underlying bulk [79, 82]. Thus, the greater availability of surface area increases the likelihood of defect nucleation and initial yield, leading to reductions in yield strain and also yield stress (due to the decrease in modulus as discussed above) with increasing VR/TV for the constant l_o nanoboxes.

Similar logic can be utilized to explain the yield behavior of the constant thickness nanoboxes. The increasing VR/TV ratio occurs due to the increase of both l_i and l_o; this increase leads to an increase of total surface area, thus resulting in the decrease in yield strain seen in Figure (40B). Although the Young's modulus increases slightly over the same range of VR/TV, the faster decrease in yield strain leads to an overall decrease in yield stress, as observed in Figure (40A).

In contrast, the constant l_i nanoboxes show a slightly different response. In an-

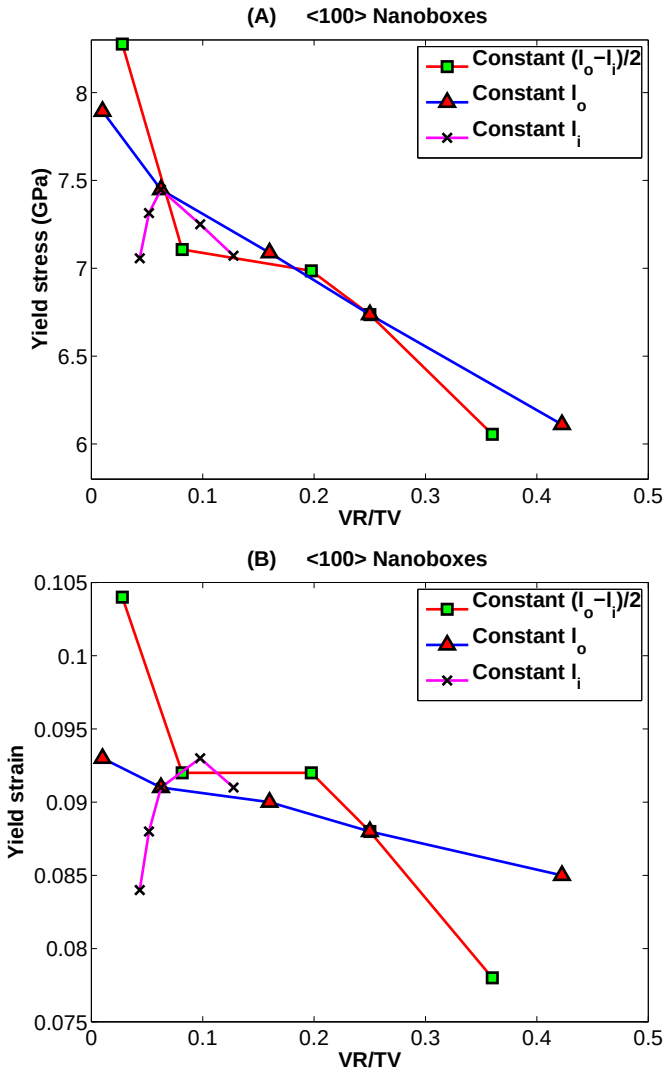

Figure 40: Variation of the (A) yield stress and (B) yield strain for $\langle 100 \rangle$ nanoboxes with VR/TV.

alyzing the yield strain for the constant l_i nanoboxes, it is observed in Figure (40) that it shows an inconsistent trend with decreasing VR/TV ratio. In particular, with decreasing VR/TV ratio, the nanoboxes show a general decrease in yield strain; this makes sense as the nanobox wall thickness, and thus the surface area increases with decreasing VR/TV, leading to enhanced opportunities for initial defect nucleation, and thus reduced yield strains.

Interestingly, the constant l_i nanoboxes with the smallest wall thicknesses and thus the largest VR/TV ratios exhibited disparate yield properties, which is consistent with previous research [81] indicating that nanoboxes with ultrasmall wall thicknesses or l_i less than about 1 nm exhibit different inelastic yield behavior. However, for larger wall thicknesses, the nanoboxes behave more like solid nanowires and the yield strain decreases as the surface area increases due to increasing l_o.

The yield stress for the constant l_i nanoboxes also shows an inconsistent trend; note that from Figure (39A), the modulus for the constant l_i nanoboxes increases with decreasing VR/TV ratio. However, because of the rapid increase in surface area with decreasing VR/TV, and thus the rapid decrease in yield strain, the increase in modulus is offset, and the yield stress for the constant l_i nanoboxes begins to decrease in Figure (40A) with decreasing VR/TV.

In general, it is found that not only the modulus of the $\langle 100 \rangle$ nanoboxes, but also the yield stresses and yield strains, as observed in Figure (41), are reduced as compared to the corresponding solid $\langle 100 \rangle$ solid nanowires. The reduced yield strains result due to the increase in available surface area afforded to the nanoboxes; this fact, when combined with the decrease in modulus that the nanoboxes experience, explains the corresponding reductions in yield stresses for the $\langle 100 \rangle$ nanoboxes as compared to the solid $\langle 100 \rangle$ nanowires.

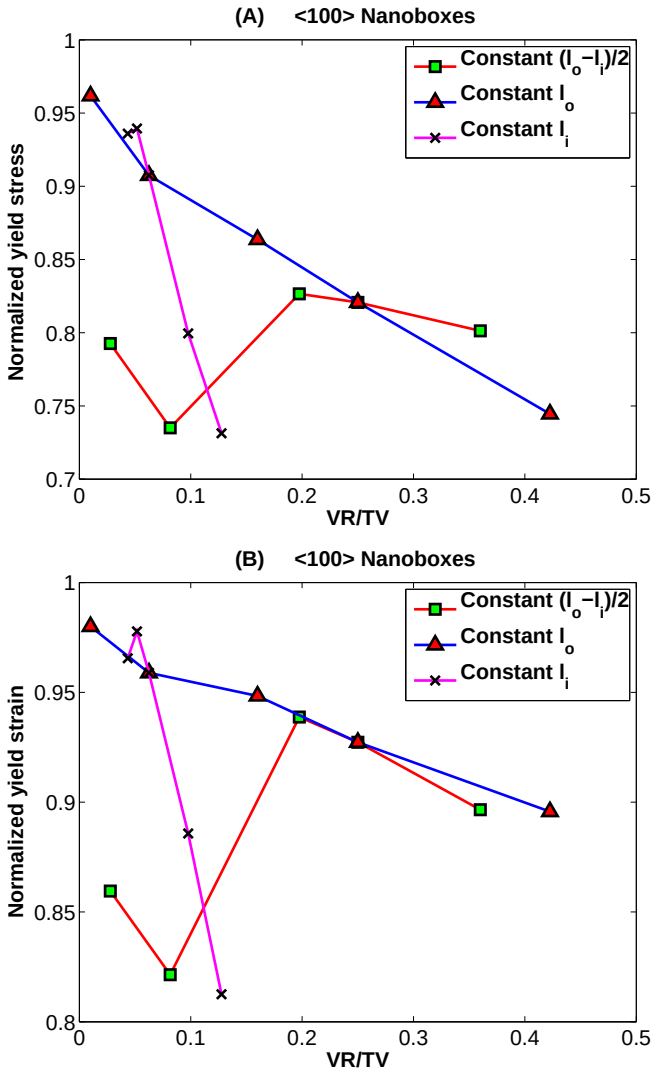

Figure 41: Variation in (A) normalized yield stress and (B) normalized yield strain (b) of $\langle 100 \rangle$ nanoboxes with VR/TV ratio.

IV.3.3 Modulus of ⟨110⟩ nanoboxes

The variations in modulus of the ⟨110⟩ nanoboxes for constant l_o, l_i and wall thickness are summarized in Figure (42A). As is illustrated, the modulus in all cases increases with increasing VR/TV ratio. The increase is largest for the nanoboxes with either constant l_o or l_i, while the modulus for the constant wall thickness nanoboxes increased only slightly.

The results are more dramatic when the moduli of the ⟨110⟩ nanoboxes are normalized by those of the corresponding ⟨110⟩ solid wires with cross section of length l_o, as shown in Figure (42B). As can be seen, the modulus increases in all cases compared to the corresponding solid wires with increasing VR/TV ratio. For the relatively small nanobox sizes considered in this work, modulus increases approaching 20% are observed as compared to the corresponding solid ⟨110⟩ wires. Furthermore, the increases are attainable for all the geometries considered, while Figure (42B) indicates that even greater strength increases with respect to the solid ⟨110⟩ wires may be achievable for nanoboxes that are considerably larger than those considered in this work due to computational limitations.

The fundamental idea underlying the notion that nanostructures can be strengthened through mass removal works because it is known that the ⟨110⟩ bulk is weaker than both the {100} and {110} surfaces [26, 27] that surround the ⟨110⟩ nanoboxes and nanowires considered in this work. Therefore, because increasing the VR/TV ratio represents, in all cases, nanoboxes that are composed of decreasing amounts of bulk material, all cases show corresponding increases in modulus. In this context, it is understandable why the constant thickness ⟨110⟩ nanoboxes show a slight increase in modulus with increasing VR/TV ratio as seen in Figure (42), because an increase of VR/TV corresponds to the removal of more bulk material, leading to a greater dependence on the surface for strength, and thus a strength increase.

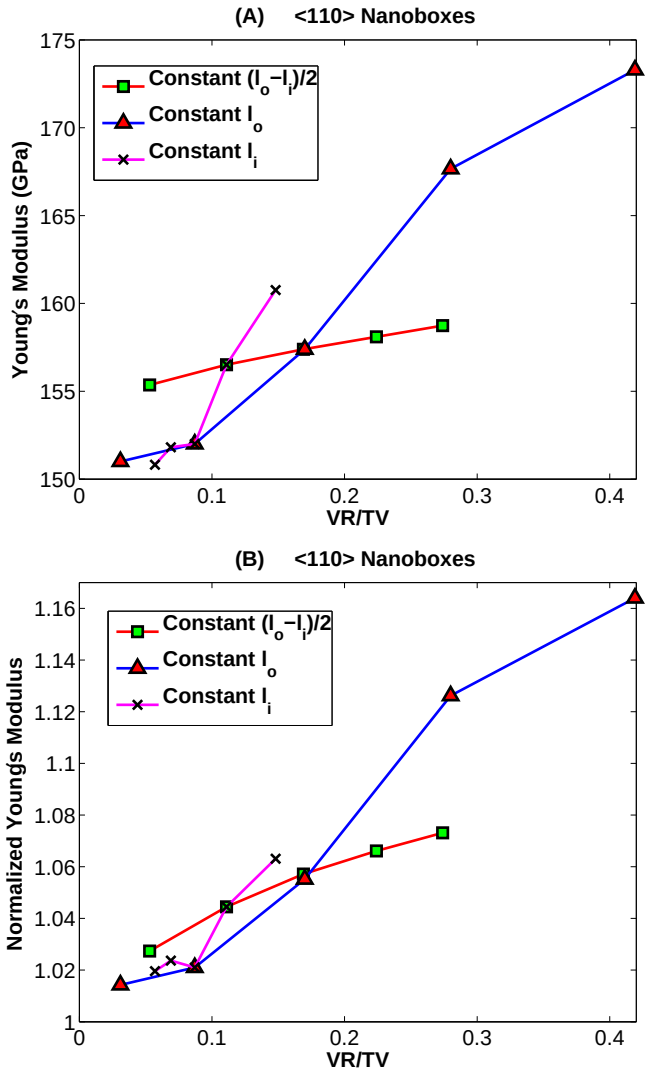

Figure 42: Variation of (A) Young's modulus and (B) Normalized Young's modulus for $\langle 110 \rangle$ nanoboxes with VR/TV.

IV.3.4 Yield stress and strain of ⟨110⟩ nanoboxes

The yield stresses and strains for the ⟨110⟩ nanoboxes are plotted in Figure (43). As can be seen, the observed trends for the yield stresses differ somewhat from those already discussed for the ⟨100⟩ nanoboxes, while the ⟨110⟩ nanobox yield strains show similar behavior as those of the ⟨100⟩ nanoboxes.

Unlike the ⟨100⟩ nanoboxes with constant l_o, the ⟨110⟩ nanoboxes with constant l_o show a distinct increase in yield stresses with increasing VR/TV, while the yield strain decreases; the yield strain decrease is tied to the increase in surface area with increasing VR/TV. It would also be expected that the yield stress for the constant l_o nanoboxes would similarly decrease; however, due to the sharp increase in modulus with increasing VR/TV as seen in Figure (42A) with increasing VR/TV, the yield stress increases with increasing VR/TV.

For ⟨110⟩ nanoboxes with constant l_i, the trend mirrors that seen for the constant l_o ⟨110⟩ nanoboxes. For constant l_i nanoboxes, an increase in VR/TV indicates decreasing nanobox wall thickness. Correspondingly, Figure (43A) illustrates that the yield stress for the constant l_i ⟨110⟩ nanoboxes increases rapidly as l_o is reduced. Similarly, increasing VR/TV for the constant l_i nanoboxes leads to reduced wall thicknesses and thus reduced surface area, leading to an increase in the yield strain, as seen in Figure (43B).

Interestingly, the yield stress for constant l_i nanoboxes increases more rapidly with VR/TV than does the yield stress for constant l_o nanoboxes. The reason for this can be inferred from Table (5), which illustrates that the volume decreases much more rapidly over the same VR/TV ratio for the constant l_i nanoboxes than for the constant l_o nanoboxes; this manifests itself in the faster increase in the modulus as seen in Figure (42A). More importantly, the surface area for constant l_i nanoboxes decreases with increasing VR/TV ratio, leading to the increase in yield strain observed in Figure (43B). Thus, the increase in modulus and yield strain with VR/TV leads

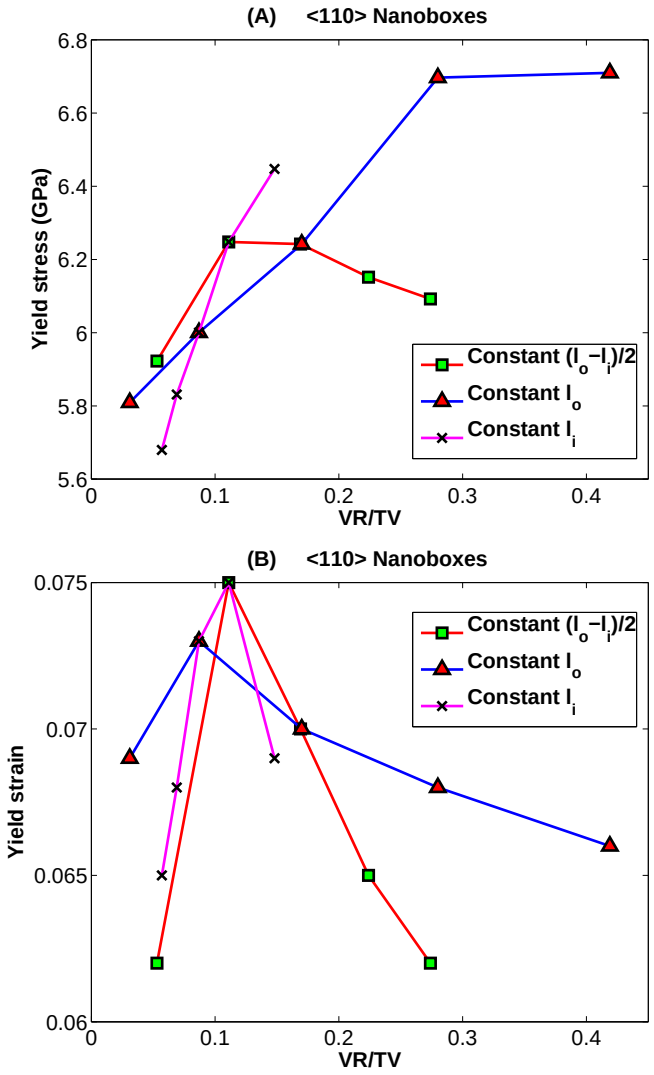

Figure 43: Variation of (A) yield stress and (B) yield strain for ⟨110⟩ nanoboxes with VR/TV.

the constant l_i nanoboxes to exhibit a rapid increase in yield stress.

Similar to the constant l_i $\langle 100 \rangle$ nanoboxes, the $\langle 110 \rangle$ nanoboxes with the smallest wall thicknesses or l_i (constant l_o with VR/TV=0.031, constant l_i with VR/TV=0.148, constant thickness with VR/TV=0.053) also show unusual yield properties [81]. The small wall thicknesses of approximately 1 nm or the small l_i cause the anomalies in the yield strain trends seen in Figure (43B). As the wall thickness increases for all three cases (constant l_o, l_i, wall thickness), each nanobox exhibits the expected trend with varying VR/TV.

For the constant wall thickness nanoboxes, both the yield stress and yield strain show a decreasing trend with increasing VR/TV. The yield strain again decreases due to an increase in surface area with increasing VR/TV. The modulus for the constant thickness $\langle 110 \rangle$ nanoboxes is fairly constant over the range of VR/TV considered in this work, as seen in Figure (42A); thus, the rapid decline in yield strain overrides the slight increase in modulus with VR/TV, leading to the decreasing trend in yield stress as seen in Figure (43A).

As observed in Figure (44), the yield strains for the $\langle 110 \rangle$ nanoboxes are lower than those of the corresponding solid $\langle 110 \rangle$ nanowires; this is attributed to the larger surface area exposed by the nanoboxes. In contrast, the yield stresses of the $\langle 110 \rangle$ nanoboxes are generally greater than those of the corresponding solid $\langle 110 \rangle$ nanowires. While the yield strains are reduced, the elevated stiffness exhibited by the $\langle 110 \rangle$ nanoboxes enables the nanoboxes to sustain larger stresses before initial yield.

IV.4 Some results on the elastic properties of solid metal nanowires

This section will present the elastic properties of rectangular solid $\langle 100 \rangle / \{100\}$ and $\langle 110 \rangle / \{100\}\{110\}$ metal nanowires for comparison. The dimensions of these nanowires are listed in Tables (6) and (7). Due to the different side surface facets, $\{100\}$ and $\{110\}$, in $\langle 110 \rangle$ nanowires, this section will perform simulations on rect-

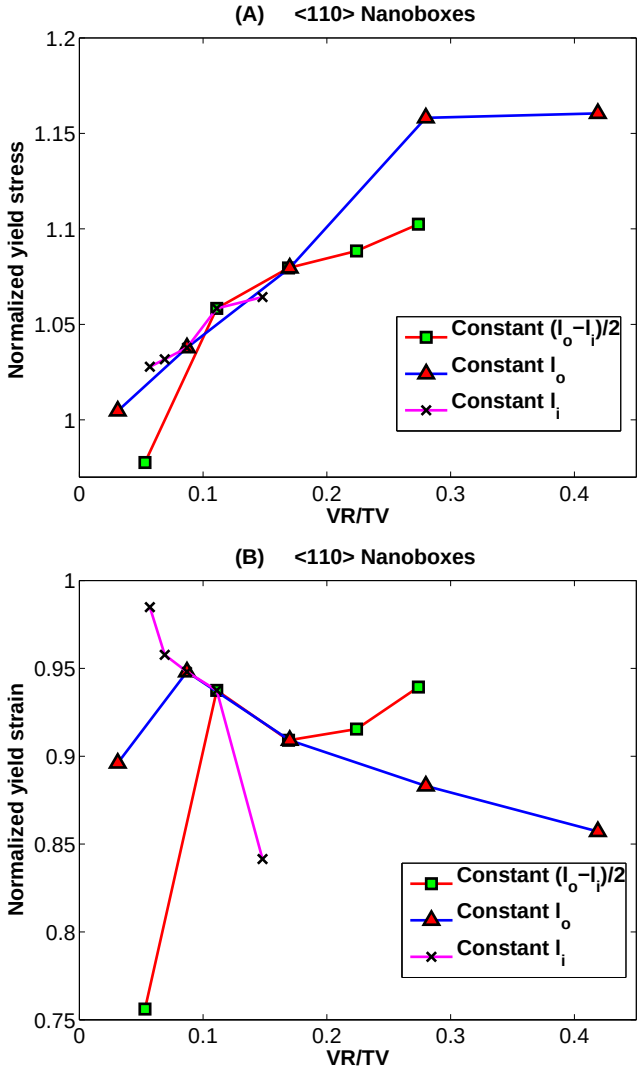

Figure 44: Variation of the (A) normalized yield stress and (B) normalized yield strain (b) for ⟨110⟩ nanoboxes with VR/TV ratio.

Table 6: Dimensions of simulated ⟨100⟩ solid copper nanowires. The first number in the table is one cross sectional edge length, the second one is the other edge length. The axial length of all the nanowires is 50. All the numbers used in this table are in units of bulk copper FCC cubic lattices, 3.615 nm.

	1	2	3	4	5
Rectangular wires	4×4	8×4	12×4	16×4	20×4
Square wires	4×4	8×8	12×12	16×16	20×20

Table 7: Dimensions of simulated solid ⟨110⟩ copper nanoplates. The length of the nanowires is 50. The meaning of the numbers in the table is as follows: the first number is edge length for {100} side surfaces; the second one is for {110} side surfaces. All the numbers used in this table are in units of bulk copper FCC cubic lattices, 3.615 nm.

	1	2	3	4	5
Square wires	4×4	8×8	12×12	16×16	20×20
Rectangular with larger {100}	4×4	8×4	12×4	16×4	20×4
Rectangular with larger {110}	4×4	4×8	4×12	4×16	4×20

angular wires with different side facets to illustrate the influence of side surfaces by biasing the size ratio of side surfaces.

The variation of the magnitude of Young's modulus is presented in Figure(45). As is shown, the magnitude of modulus increases with the increase of cross section size for both square and rectangular nanowires. The modulus of the rectangular nanowire is smaller compared to that of the corresponding square wire. The physical mechanism that leads to the variation of Young's modulus has been provided by several researchers [26, 27]. In that work, they correlated the variation in Young's moduli to nonlinear elasticity of bulk copper coupled with the equilibrium strain, which was resulted from the high surface to volume ratio of nanowires.

One interesting thing observed in solid nanowires is the variation trend of the normalized Young's moduli of nanoplates. The normalized Young's moduli are obtained by normalizing the the modulus by that of the corresponding solid nanowires. The normalized volume difference is utilized to characterize the weight difference between

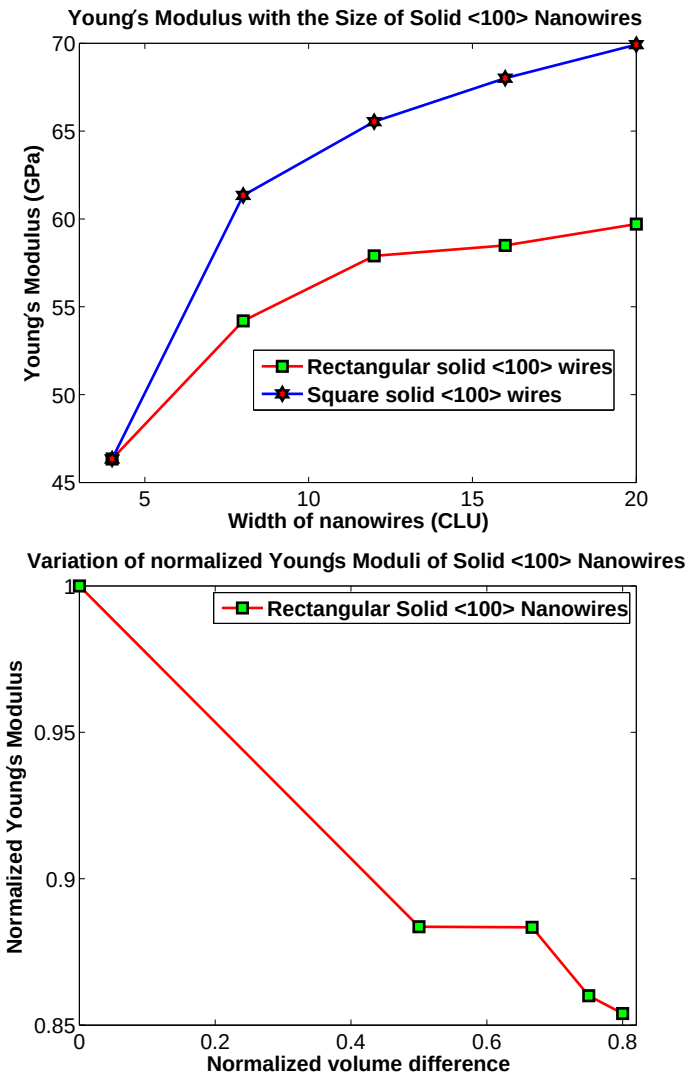

Figure 45: Variation of the magnitude of Young's moduli and normalized Young's moduli of $\langle 100 \rangle$ of solid nanowires with their cross sectional sizes, whose dimensions are listed in Tables (6). The unit of wires dimension is in cubic lattice unit of bulk copper, 3.615nm.

square and rectangular nanowires. It is noticed that the normalized values exhibit a decreasing trend with the increase of cross section edge length. This illustrates that the Young's moduli of $\langle 100 \rangle$ nanowires experience a slight drop in magnitude with only one the cross section edge decreases.

The variation of yield stress and yield strain of $\langle 100 \rangle$ nanowires are presented in Figure(46). As is shown, the yield stress and yield strain decrease with the increase of cross section size. The decrease trend of yield stress is tied to the relaxation of nanowires that result from the high surface to volume ratio [82, 153], while the variation trend in yield strain is a result of the decrease trend in yield stress and increase trend in Young's modulus.

The variation in the magnitude of Young's modulus of $\langle 110 \rangle$ solid nanowires is presented in Figure (47). exhibits an opposite trend with respect to that observed in $\langle 100 \rangle$ wires. This is tied to the nonlinear elasticity of bulk copper, which has been observed and discussed by several researchers [26, 27]. One interesting observation in this Figure is that the wire with larger $\{100\}$ surfaces is stiffer than the wire with larger $\{110\}$ surfaces. Thus the $\{100\}$ surface is stiffer compared to $\{110\}$ surface in $\langle 110 \rangle$ wires, which could be utilized to engineer wire mechanical properties in future.

The variation of yield stress and yield strain with wire cross section size is demonstrated in Figure (48). It is shown that yield stress and yield strain exhibit a decrease trend with the cross section edge length of nanowires. It is shown that the wire with larger $\{110\}$ surfaces exhibit a similar yield stress and yield strain in magnitude with corresponding square nanowires, while the wire large $\{100\}$ surfaces has a larger yield stress and yield strain. Thus the $\{100\}$ surface could be utilized to created stiffer and stronger nanocomponents in future nanostructure design.

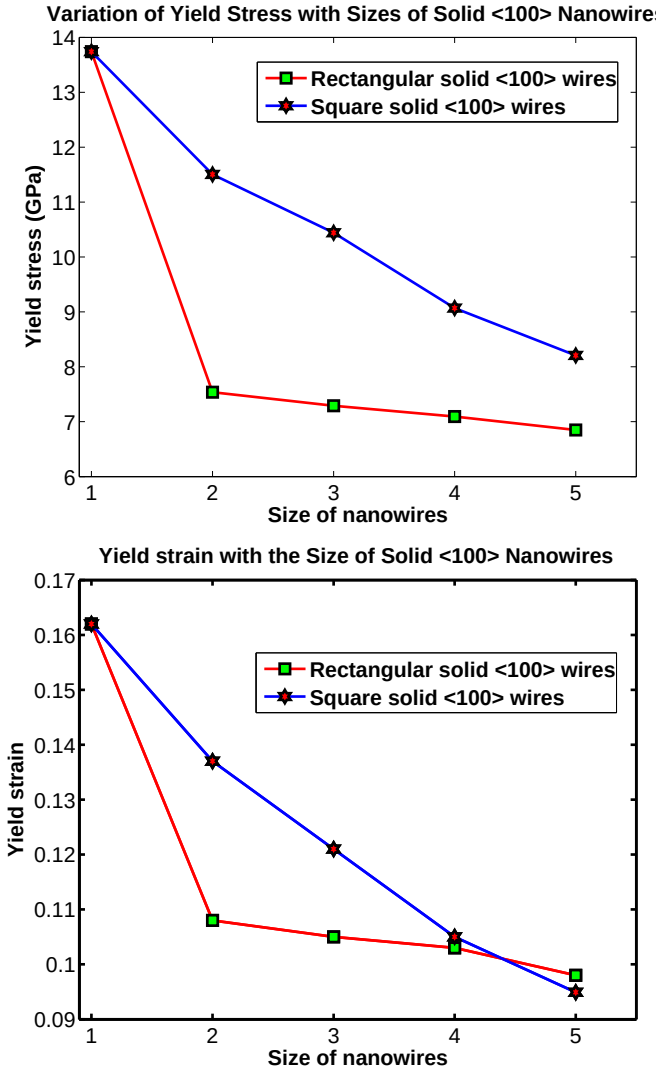

Figure 46: Variation of the magnitude of yield stress and yield strain of $\langle 100 \rangle$ solid nanowires with their cross sectional sizes. The corresponding geometry of nanowires are listed in Table (6). The notation '1' to '5' in this figure corresponds to wire dimensions in in Table (6).

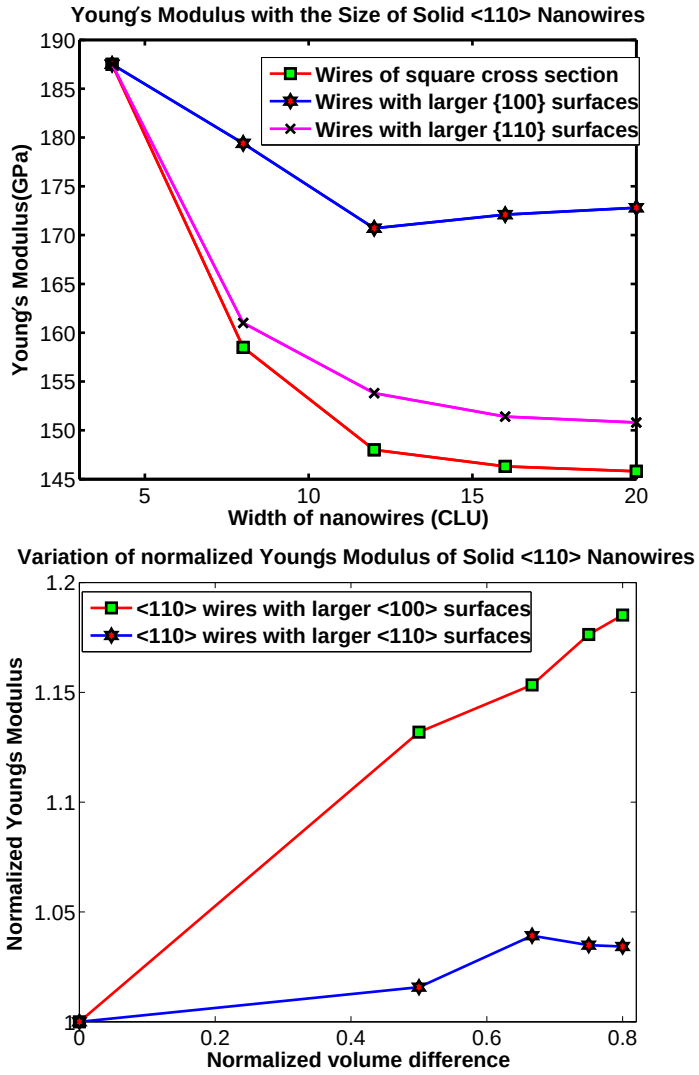

Figure 47: Variation of the magnitude of Young's moduli of $\langle 110 \rangle$ of solid nanowires with their cross sectional sizes, whose dimensions are listed in Table (7).

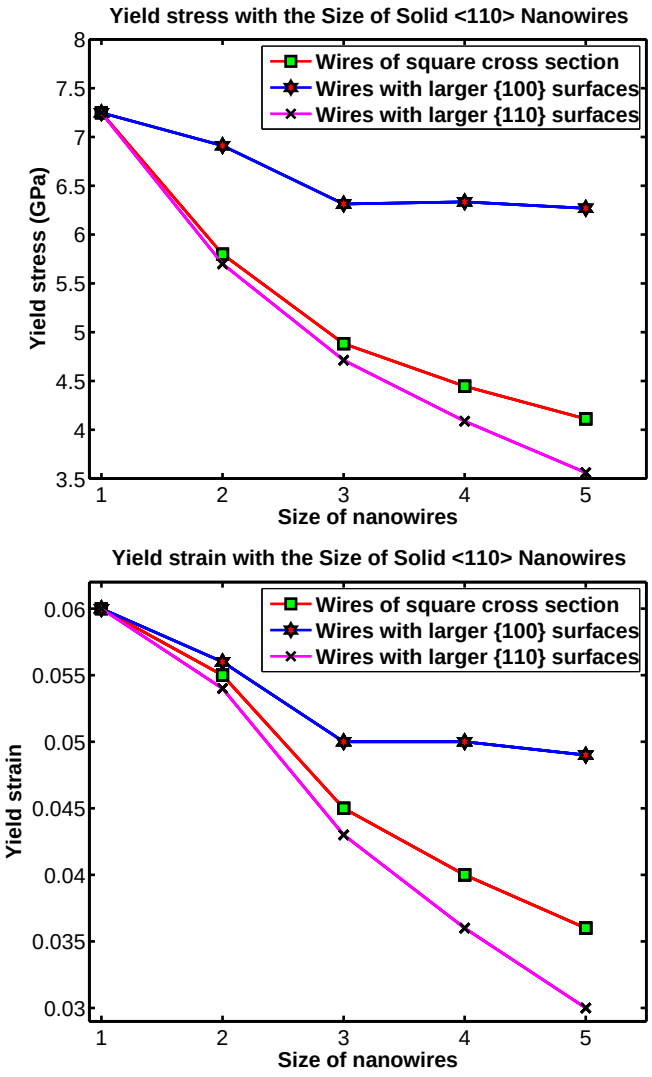

Figure 48: Variation of the magnitude of yield stress and yield strain of $\langle 100 \rangle$ solid nanowires with their cross sectional sizes. The corresponding geometry of nanowires are listed in Table (7). The notation '1' to '5' in this figure corresponds to wire dimensions in in Table (7).

CHAPTER V

THE COUPLED EFFECTS OF GEOMETRY AND SURFACE ORIENTATION ON THE MECHANICAL PROPERTIES OF METAL NANOWIRES

The purpose of this chapter is to investigate the coupled effects of geometry and surface orientation on the deformation behavior and mechanical properties of metal nanowires. By varying the nanowire cross section from square to rectangular, nanowires with dominant surface facets are created that exhibit distinct mechanical properties due to the different inelastic deformation mechanism that are activated. In particular, it is found that non-square nanowires generally exhibit lower yield stresses and strains, lower toughness, elevated fracture strains, and a propensity to deform via twinning; this chapter will quantify the links between the observed deformation mechanisms due to non-square cross section and resulting mechanical properties, while illustrating that geometry can be utilized to tailor mechanical properties of nanowires. The results in this chapter are based on the work of Ji and Park [81, 93].

V.1 Introduction

The mechanical properties of metal nanowires have been extensively studied for two major reasons: (1) To gain fundamental information about the strength of nanomaterials, and how free surfaces, which are prevalent in nanomaterials, contribute to the unique properties of nanowires [4, 25, 26, 50, 87]; (2) Because the physical properties of nanowires are intricately coupled, i.e. electromechanical [17–19] and optomechanical [20–23], it is critical to understand the mechanical properties of deforming nanowires so that highly multifunctional NEMS can be designed.

The current state of understanding on the mechanical behavior and properties of nanowires has come from both experiment [36–39, 61–63, 143, 155] and atomistic

calculations [59, 67, 69, 72, 74–76, 78, 79, 82, 85, 91, 92, 136, 137, 152]. This collection of information has established that, in general, nanowires have significantly higher yield stresses and strains than bulk materials, that single defects can cause catastrophic losses of strength in single crystal nanomaterials, and that the mechanical properties are strongly dependent on the axial orientation of the nanowires.

Most simulations of the mechanical behavior of nanowires have focused on regular geometries (i.e. square cross section) with ⟨100⟩ axial orientations. However, recent experiments have elegantly shown that geometry can distinctly alter the physical properties of nanomaterials. For example, geometry is known to have a large effect on the optical properties of metal nanoparticles [149]. More recent work has analyzed the optical properties of hollow metallic nanostructures [140, 150]; it was found that the optical properties can be altered by hollowing out the nanostructure. While it was recently determined that the transverse surface orientation has a first order effect on the mechanical behavior and properties of nanowires, the effects of geometry have, with few exceptions [81, 92, 152], not been analyzed.

This chapter will first present the analysis on the ⟨100⟩/{100} nanowires based on the work of Ji and Park [81], where it was found that simply changing the cross sectional geometry of ⟨100⟩ copper nanowires with {100} surfaces from square to rectangular changed the tensile deformation mode from distributed plasticity via partial dislocation nucleation and propagation to a twinning-dominated deformation mode which allowed the {100} surfaces to reorient to lower energy {111} surfaces. Then following through on this earlier work, this chapter perform a comprehensive study on the tensile deformation of both ⟨100⟩ and ⟨110⟩ nanowires with various cross sectional geometries and transverse surface orientations. In doing so, it is found that by altering the cross sectional geometry from square to rectangular, the nanowire deformation modes can change from the slip of full and partial dislocations to organized and diffusionless twinning. Accordingly, the mechanical properties of the nanowires

vary greatly depending on the cross sectional geometry, leading to significant disparities in yield stress and strain, fracture strain and toughness. Because varying the geometry results in creating nanowires with multiple surface facets of different size and orientation, it is demonstrated that altering the nanowire cross sectional geometry creates a coupling between geometry and the exposed transverse surface orientations that dictates the observed deformation modes and mechanical properties of the nanowires.

V.2 Geometry effect on the inelastic deformation modes of $\langle 100 \rangle / \{100\}$ wires

This section will address the deformation mechanism by utilizing classic molecular dynamics(MD) simulation to demonstrate that the geometry of nanomaterials can be utilized to control the operant modes of inelastic deformation and thus the mechanical properties of nanometer scale materials. The simulations were performed on hollow copper nanowires, which is called nanoboxes, using the embeded atom method (EAM) [105] with the potential developed by Mishin *et al.* [111]; this potential can accurately represent the stacking fault and twinning energies for copper, which is important in accurately modeling the inelastic deformation behavior. The nanoboxes were created by first cutting a solid wire out of the bulk with a square cross section, then removing atoms from the center of the wire leaving a square hole. All wires had the same length of 40 cubic lattice units (CLU), where 1 CLU = 0.3615 nm for copper, but different cross sectional geometries; variations in outer cross sectional length (l_o), inner cross sectional length (l_i), box wall thickness ($(l_o - l_i)/2$) and constant ratio of wall thickness to inner cross sectional edge length ($(l_o - l_i)/(2l_i)$) were also considered. Solid wires with length and cross sectional dimensions corresponding to the nanobox wall geometries given in Table 8 were also considered for comparative purposes. The MD simulations were performed on two paralleled processors, Intel 2.0 GHz. The simulation time depends on the wire size, which ranges from several hours

Table 8: Dimensions of simulated copper nanoboxes, given as outer cross sectional edge length l_o by the inner cross sectional edge length l_i; all numbers represent cubic lattice units (CLU), where 1 CLU = 0.3615 nm for copper. All nanoboxes have a length of 40 CLU.

Constant $(l_o - l_i)/2$	7×2	10×5	14×9
Constant l_o	14×2	14×5	14×9
Constant l_i	14×9	18×9	25×9
Constant $(l_o - l_i)/(2l_i)$	20×12	30×18	40×24

for small wires to several days for large wires.

The resulting nanoboxes had a $\langle 100 \rangle$ longitudinal orientation, with $\{100\}$ transverse side surfaces. The atoms were first brought to energy minimizing positions, after which a Nosé-Hoover thermostat [100, 102] was applied to thermally equilibrate the atoms at 10 K. The nanoboxes were then loaded in tension in the length direction by fixing one end of the wire, creating a ramp velocity profile which went from zero at the fixed end to a maximum value at the free end, then pulling the free end at the maximum value; the ramp velocity profile was utilized to avoid the emission of shock waves from the loading end. The strain rate in the simulations was $\dot{\epsilon} \approx 10^9$ s^{-1}, which is lower than that at which crystalline defects are precluded due to the high rate of loading [60]. All simulations were performed without periodic boundary conditions to capture the relevant surface effects using the Sandia-developed code Warp [127, 128].

Figure (49) shows snapshots of a twinning-dominated deformation mechanism of a 14×9 shell nanowire under tensile loading. The figures on the left side are constructed based on energy parameter; while corresponding figures on the right side are visualized through centrosymmetry parameter [8]. Centrosymmetry is a measure of local atomic coordination; a value of zero indicates a bulk, full-coordinated atom. Initially, the shell nanowire is in $\langle 100 \rangle / \{100\}$ orientation with 4 line defects formed by the shell structure, and there is no other defects. The four edge lines show a inward deformation due to the strong surface effect under tensile loading, as is illustrated

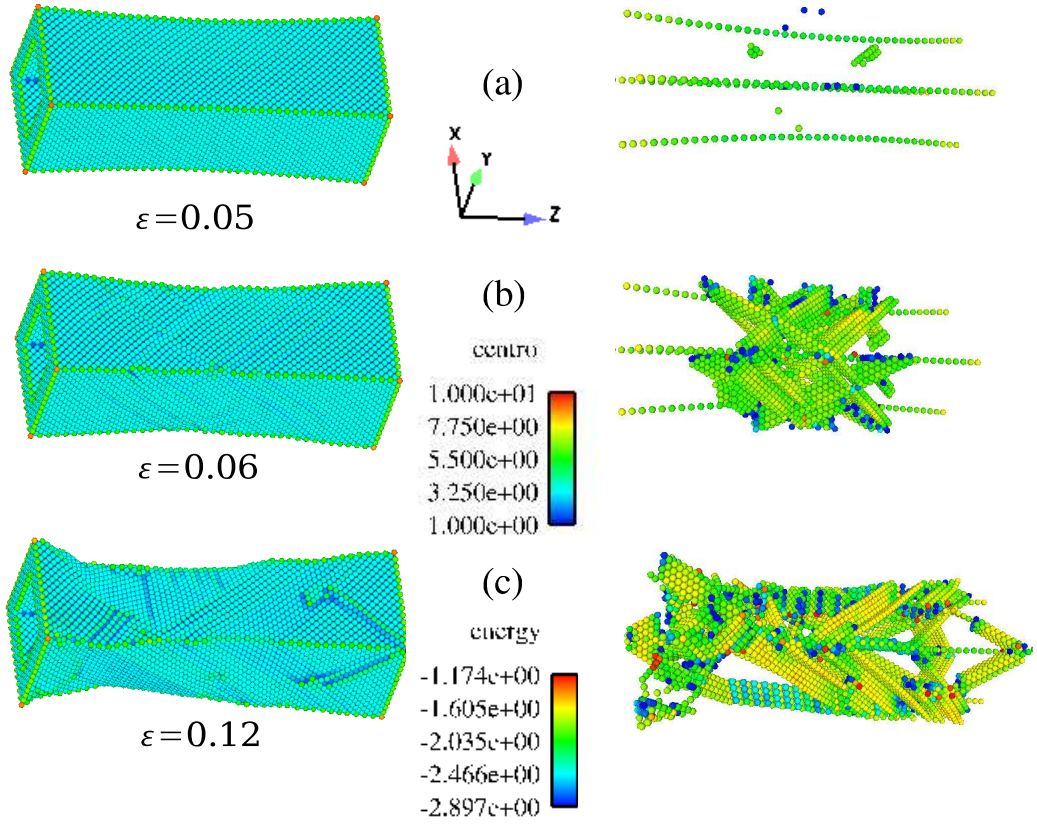

Figure 49: Snapshots of the deformation behavior of a 14×9 silver shell nanowire under tensile loading. The left column is constructed based on potential energy in unit of eV; right side column is visualized through centrosymmetry parameter [8].

.

Table 9: Schmid factors for various wire orientations considering slip (full dislocations), tensile-induced twinning (partial dislocation slip) and compression-induced twinning (partial dislocation slip).

Orientation	Slip	Tensile-twin	Compression-twin
$\langle 100 \rangle$	0.42	0.24	0.47

in Figure (49a). At a strain of ϵ=0.06, stacking faults nucleate at the middle of the nanowire through the movement of partial dislocations. These stacking fault structures are relatively clean and parallel with each other, as is shown in Figure (49b). With the continuation of tensile loading, these parallel stacking faults begin to move and act as twin boundaries, which separate newly formed {111} surfaces and initial {100} surfaces. This twinning-dominated {100} to {111} reorientation behavior is commonly observed in compression of $\langle 100 \rangle$ solid nanowires which is favored by a high Schmid factor, as is shown in Table 9. Related discussions have been addressed by Park *et. al.* [85]. The ability of showing {111} surfaces, resulting from the movement of twin boundaries, may provide additional driving force for further deformations.

A close examination of the tensile loading behavior of $\langle 100 \rangle$ nanowire is presented in Figure(50). As is shown in Figure(50a), the initial twin boundaries are formed from the motion of different slip systems. Under increased tensile loading, the opposing twin boundaries in the box walls annihilate each other, resulting in a clean twin structure composed of twins separated by undeformed {100} surfaces, as seen in Figure (50b). A key indicator that twinning has occured is that the transverse surface orientation, which was initially {100}, has reoriented to the low energy and close packed {111}-type through the lattice rotation caused by the twin boundaries. The rotation of the nanobox transverse surfaces caused by the twin boundaries and the separation of the {100} and {111} surfaces due to the twin boundaries is seen in

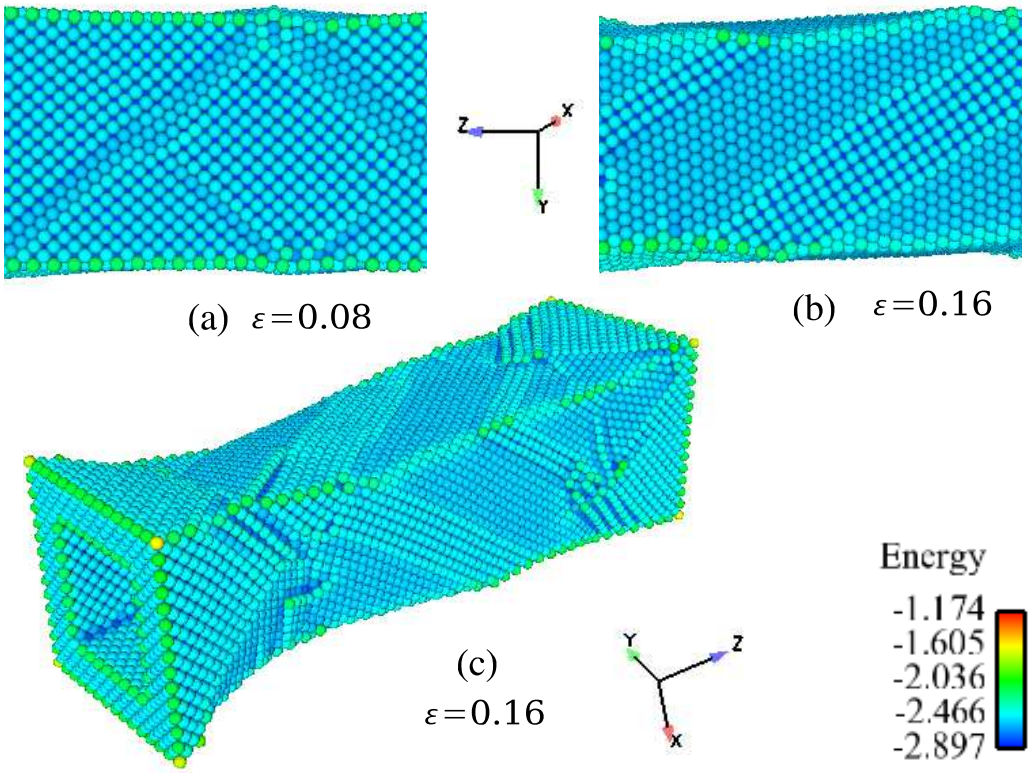

Figure 50: Evolution of the tensile-induced twinning in a 40 CLU long nanoshell with a $l_o = 14$ CLU and $l_i = 9$ CLU, where potential energy is in units of eV. (a) and (b) show the evolution of the twins for an individual surface, while (c) shows the effect of twinning on the entire nanoshell.

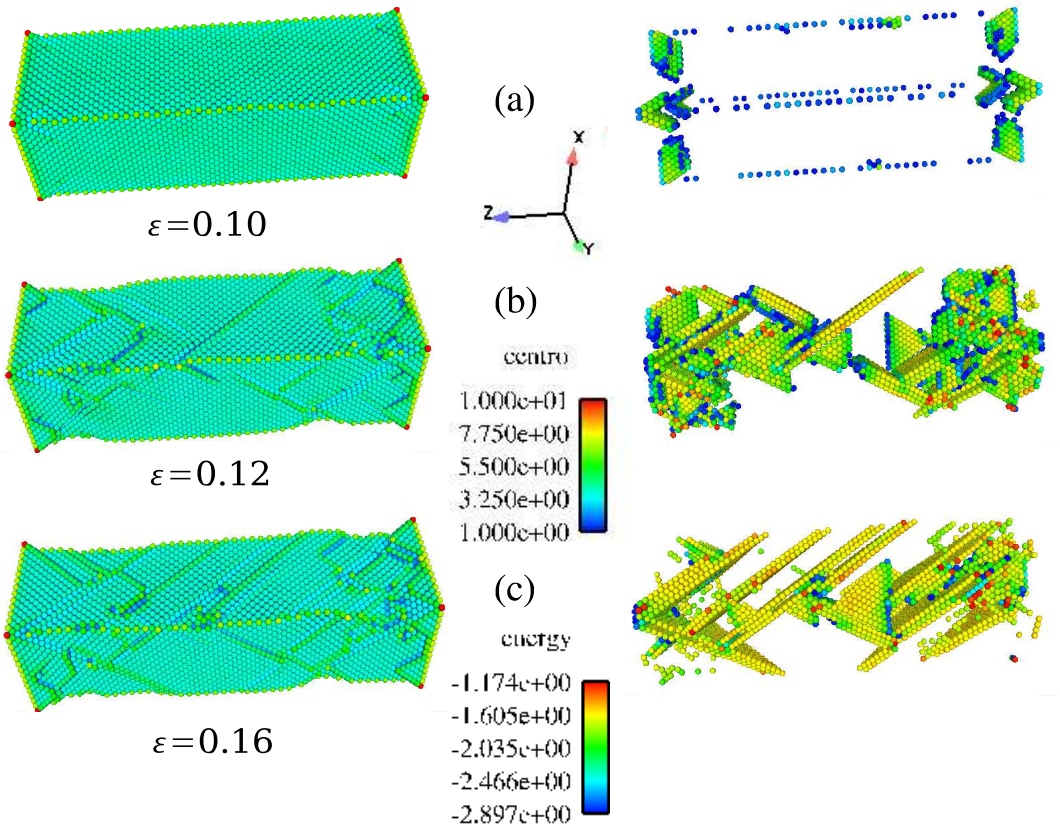

Figure 51: Snapshots of the deformation behavior of a 14×14 silver shell nanowire under tensile loading. The left column is constructed based on potential energy in unit of eV; the column on the right side is visualized through centrosymmetry parameter [8].

.

Figure (50c).

For comparison, Figure(51) presents the snapshots of the corresponding tensile-loaded $\langle 100 \rangle$ copper solid nanowires. At a strain of ϵ =0.10, partial dislocations nucleate at both wire ends instead of from the middle as observed in the 14×9 nanobox. Meanwhile, there is no obvious inward deformation on four edge lines as they did on the nanobox. As the tensile deformation continues, a set of distributed stacking faults are observed along the length direction. These stacking faults interact with each other and result in full dislocations on the wire surfaces, which impede the mobility of stacking faults and lead to necking in the solid nanowire.

To better illustrate the effects of geometry on the operant deformation mechanisms, this section will perform a systematic series of studies on solid nanowires with a constant length of 40 CLU but non-square cross sections of varying aspect ratio. The non-square cross section is the key reason why this behavior has not been observed as most prior simulations of the tensile deformation of $\langle 100 \rangle / \{100\}$ FCC metal nanowires considered those with square or nearly square cross sections [59, 69, 76, 79]. The wires with non-square cross section are utilized as they represent a single wall of a nanobox, while mitigating the influence of other factors such as the adjacent box walls.

The first key factor in influencing the twinning dominated behavior is the aspect ratio of the cross section. This is illustrated in Figure (52), which shows the deformation of solid wires with the same length, but different cross sectional dimensions. Consistent with prior studies [59, 69, 76, 79], the square cross section $\langle 100 \rangle$ wire in Figure (52a) deforms predominantly via the propagation of partial dislocations on alternating slip planes along the wire length. In contrast, the wires shown in Figures (52b) and (52c) have non-square cross sections with aspect ratios of 3 and 4.5, respectively, and exhibit twinning as the dominant deformation mode.

To explain the observed twinning, it needs to emphasize that all transverse surfaces

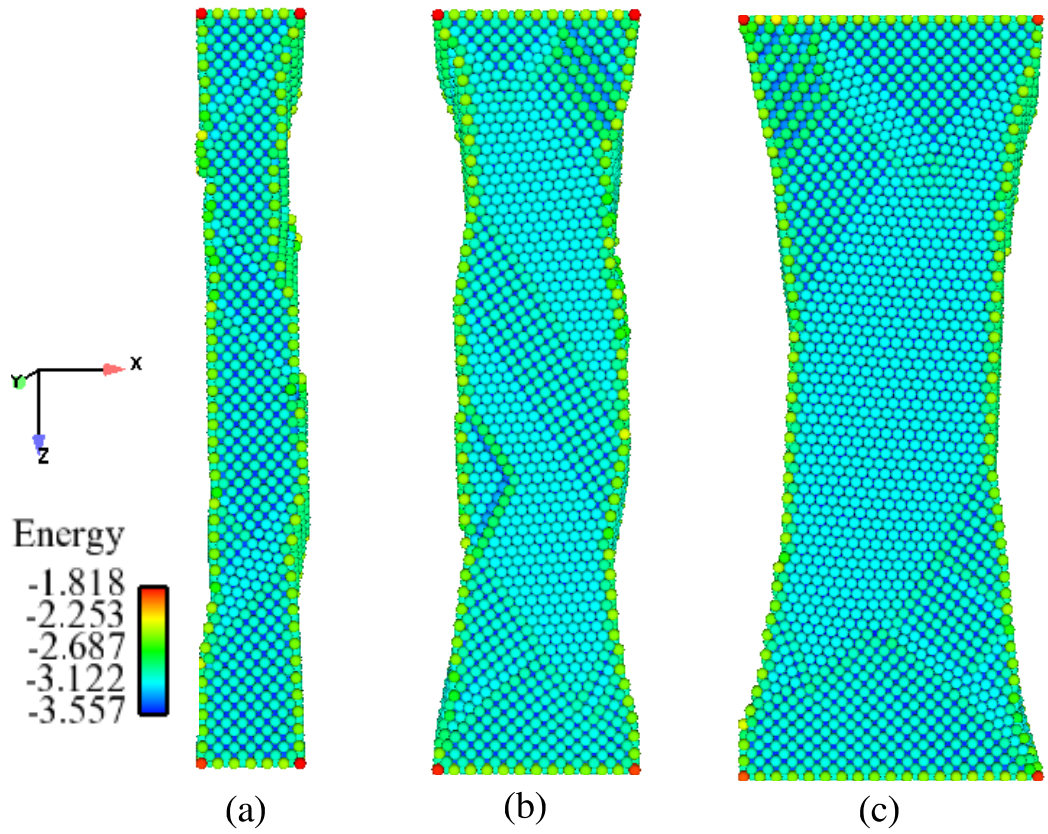

Figure 52: The deformation of 40 CLU long, 4 CLU high copper nanowires at a strain of ϵ =0.18, with varying thickness of (a) 6 CLU; (b) 12 CLU; (c) 18 CLU. Potential energy is in units of eV. Note twinning-dominated deformation for non-square cross sectional wires seen in (b) and (c).

are initially {100}. If the cross section is square, there is no asymmetric energetic driving force; instead, slip systems on alternating {111} planes are activated [79] which keeps the cross section square as shown in Figure (52a). In contrast, wires with a rectangular cross section have two transverse {100} surfaces that have a majority of the available transverse surface area; one thing to be emphasized is that the twinning occurs exclusively on the larger {100} surfaces allowing both to reduce their area by reorienting to the close-packed {111} surface. The asymmetry of the cross sectional geometry thus results in a sufficient driving force for the larger surfaces to reduce their area and therefore their energy through reorientation via twinning-dominated deformation. It is worth noting that Schmid factors [85] predict tensile deformation in the $\langle 100 \rangle$ direction via emission of full dislocations; the current analysis demonstrates that geometry can be used to engineer and bias the observed deformation mechanisms of nanometer scale materials.

For larger cross section nanowires, the thickness begins to have a dominant effect. For nanowire thicknesses that are greater than about 4 nm, the deformation mode changes from twinning to large scale distributed plasticity, with the nucleation and propagation of partial dislocations leading to the eventual entanglement of stacking faults formed on intersecting slip planes; this is illustrated in Figure (53). This size-dependent crossover in deformation mechanism is consistent with what has been reported in the literature [79]; the crossover occurs as plasticity confinement effects disappear with increasing system size, leading to increased opportunities for defect nucleation and propagation.

The nanoboxes that are constructed by utilizing the non-square cross section nanowires thus inherit the deformation mechanisms seen in the individual nanowires, including the thickness effects discussed earlier. It has been found that the nanoboxes behave similarly as the nanowires with one exception; for the nanoboxes with $l_i < 2$ CLU in Table (1), the stacking faults created during the initial stages of plastic de-

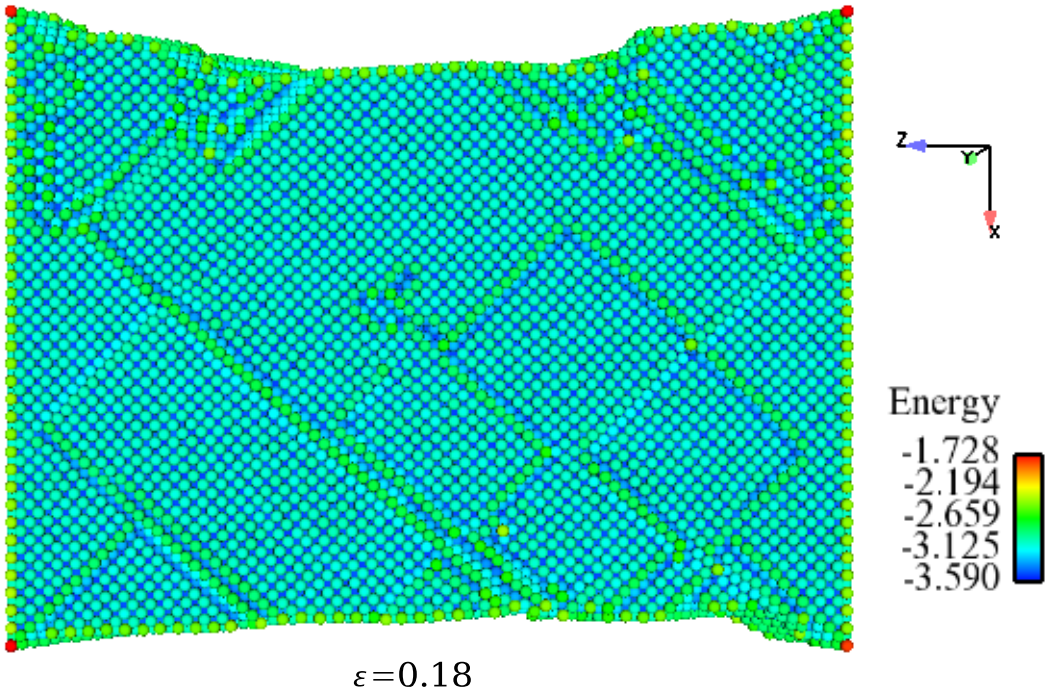

Figure 53: The deformation of a 40 CLU long copper nanowire by partial dislocation nucleation and propagation at a strain of $\epsilon = 0.18$ with cross sectional dimensions of 36 CLU $\times$ 12 CLU. Potential energy is in units of eV.

formation intersect and entangle with those formed in adjacent box walls due to the proximity of the neighboring walls; this entanglement strongly discourages twin formation. All other nanoboxes in Table (1) showed twinning except for the 40×24 and 25×9 nanoboxes, which have the same box wall thickness; for these nanoboxes, the large wall thickness led to distributed plasticity similar to that seen in Figure (53).

In conclusion, this section has utilized molecular dynamics simulations to show unexpected twinning-dominated deformation in $\langle 100 \rangle$ copper nanowires and nanoboxes under tensile loading. The twinning is enabled by biasing the deformation through creation of non-square wire cross sections; because the transverse surfaces of the wire have the same orientation, the twinning allows the box walls with the greatest surface area to reduce this area by exposing close packed and low energy $\{111\}$ transverse surfaces. These observations not only indicate the importance and utility of geometry in engineering the mechanical properties of materials at nanometer scales, but also show that the properties of hierarchical nanostructures can also be controlled through careful tailoring of the properties of the individual building blocks.

V.3 Systematic study on the coupled geometry and surface orientation effect on the mechanical properties of $\langle 100 \rangle$ and $\langle 110 \rangle$ wires

This section will continue my previous analysis in last section and present a systematic study on the coupled geometry and surface orientation on the mechanical properties of metal nanowires. The wires with two axial orientations are selected to demonstrate the influence of axial and side surfaces orientation.

A schematic of the $\langle 100 \rangle$ and $\langle 110 \rangle$ wires is illustrated in Figure(**??**), where the wires are categorized as four groups according to their axial and surface orientations. The $\langle 100 \rangle / \{100\}$ wire has a $\langle 100 \rangle$ axial orientation with four $\{100\}$ side surfaces, while the $\langle 100 \rangle / \{110\}$ wire has the same axial orientation but four $\{110\}$ side surfaces. The $\langle 110 \rangle / \{100\}\{110\}$ wire has a $\langle 110 \rangle$ longitudinal axial with two $\{100\}$ and two $\{110\}$ side surfaces, while the $\langle 110 \rangle / \{111\}\{112\}$ wire has two $\{111\}$ and two

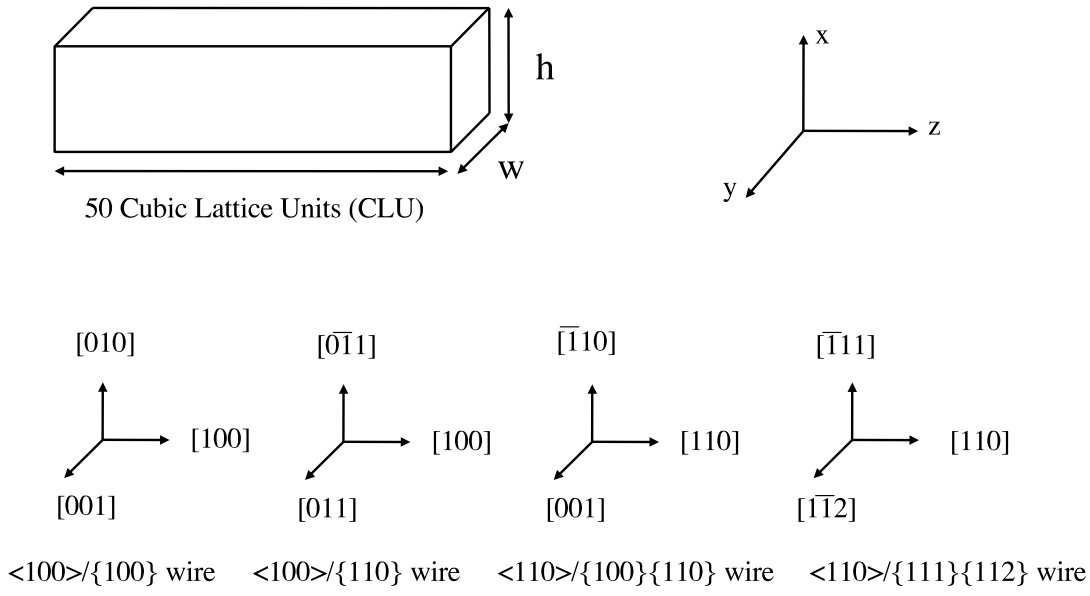

Figure 54: Schematic of the ⟨100⟩ and ⟨110⟩ copper nanowires and the different side surface orientations considered in this work; 1 cubic lattice unit (CLU) = 0.3615 nm for copper.

{112} side surfaces. Of these nanowires, some have been experimentally observed: ⟨100⟩/{100} wires [73,143], ⟨100⟩/{110} wires [156], ⟨110⟩/{100}{110} wires [73,143]. The ⟨110⟩/{111}{112} wire has not been experimentally observed and are presented here for comparative analysis.

This section performed molecular dynamics simulations on copper nanowires using an embeded atom method (EAM) [105,108], as the interatomic interaction model. The potential utilized here was developed by Mishin *et al.* [111]. This potential accurately captures the stacking fault and twinning energies, which is critical in analyzing inelastic deformation.

The ⟨100⟩ and ⟨110⟩ wires were created by slicing a collection of atoms from a

Table 10: Cross sectional dimensions in terms of w × h for ⟨100⟩ copper nanowires, where w and h are defined in Figure (54). All dimensions are in CLU.

Orientation	1	2	3	4
⟨100⟩/{100}	5×5	5×10	5×15	5×20
⟨100⟩/{110}	5×5	5×10	5×15	5×20

Table 11: Cross sectional dimensions in terms of w × h for ⟨110⟩ copper nanowires, where w and h are defined in Figure (54). All dimensions are in CLU.

Orientation	1	2	3	4	5	6	7
⟨110⟩/{100}{110}	20×5	15×5	10 ×5	5×5	5×10	5×15	5×20
⟨110⟩/{112}{111}	20×5	15×5	10 ×5	5×5	5×10	5×15	5×20

bulk FCC copper crystal. The lengths were all 50 cubic lattice units (CLU) in the z-direction, where 1 CLU=0.3615 nm for copper, but with different cross sectional geometries. The various cross sectional dimensions of the nanowires in terms of w × h in Figure (54) are given in Tables (10) and (11). The purpose of varying the cross sectional dimensions from square to rectangular is to bias one of the surface orientations over the other for a given nanowire, and to observe the effects on the nanowire deformation mechanisms and mechanical properties. For example, for the ⟨110⟩/{100}{110} wires, creating a rectangular cross section would enlarge either the {100} or the {110} surface.

The copper nanowires were first relaxed to energy minimizing positions using the conjugate gradient method; the wires were then equilibrated at 10K using a Nosé-Hoover thermostat [100, 102] for 100 ps before being loaded in tension along the z-direction. The loading rate in this work is on the order of $\dot{\epsilon} \approx 10^9$ s^{-1}. During the loading process, no thermostat was applied to ensure adiabatic conditions. The equations of motion were integrated in time using a velocity Verlet algorithm, and all simulations were performed using the Sandia developed code Warp [127, 128]. No periodic boundary conditions were used at any point in the simulations to capture

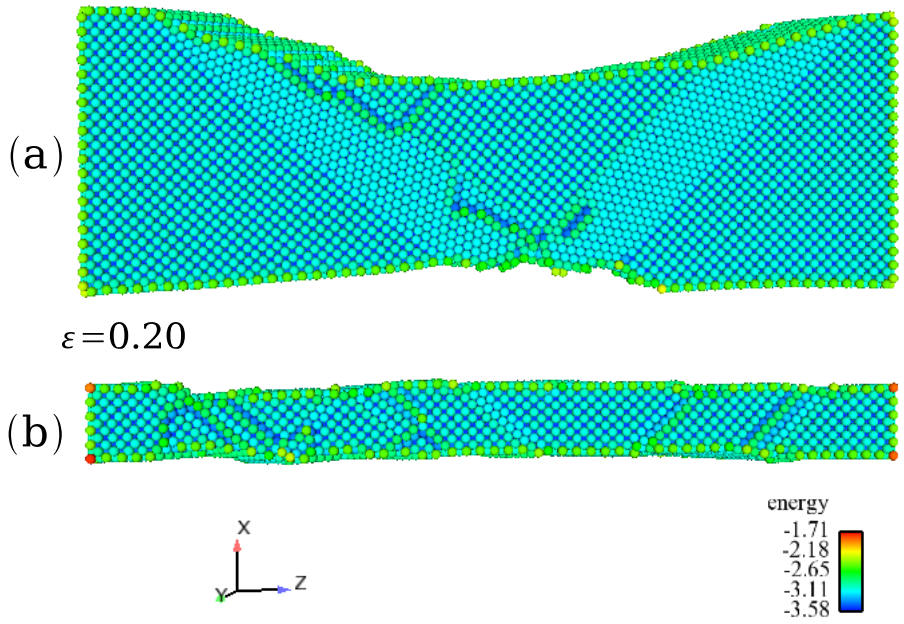

Figure 55: Snapshots of the tensile loaded ⟨100⟩/{100} nanowires at a strain of ϵ=0.20. (a) 20 × 5; (b) 5 × 5. The images are constructed based on potential energy with units of eV

the relevant surface effects.

V.3.1 Tension of ⟨100⟩/{100} and ⟨100⟩/{110} wires

This section now presents the simulation results on the tensile loaded ⟨100⟩ nanowires; the dimensions considered are given in Table (10), while the orientations are shown in Figure (54).

The deformation modes of tensile loaded rectangular ⟨100⟩ nanowires have been evaluated with comparison to square nanowires in last section. As illustrated in Figure (55), the tensile loaded square nanowire exhibits yield and plasticity by the nucleation and propagation of full and partial dislocations, while the rectangular wire shows diffusionless and twinning-dominated reorientation in the post-yield deformation period. Specifically, the larger {100} surfaces reorient to form lower energy {111} surfaces as seen in Figure (54a), while the smaller {100} surfaces reorient to form higher energy

{110} surfaces. Furthermore, the influence of thickness on geometry effect has also been considered in that work: thin wires tend to show twin structures due to the strong surface confinement, while thick nanowires are found to deform with full and partial dislocations.

In addition to the influence of wire thickness, the side surface orientation has been found to have a first order effect on the deformation modes of FCC metal nanowires [85]. The present work is hoping to investigate the coupled effects of side surface orientation and geometry; therefore, I performed atomistic simulations of the tensile deformation of ⟨100⟩/{110} square and rectangular nanowires. The ⟨100⟩/{110} nanowires have the same axial orientation and cross sectional sizes as ⟨100⟩/{100} wires, but with the crystal rotated about the ⟨100⟩ axis by 45 degrees, resulting in exposed {110} side surfaces.

Snapshots of the tensile loaded ⟨100⟩/{110} wires are presented in Figure (56). As is shown, the square ⟨100⟩/{110} nanowire accommodates plastic deformation by showing dispersed full and partial dislocations along the axial direction, which is similar to what has been observed in the square ⟨100⟩/{100} wire. In contrast, the rectangular ⟨100⟩/{110} nanowire, instead of deforming via twinning as observed in rectangular ⟨100⟩/{100} wires, exhibits localized plastic deformation by showing full and partial dislocations. Thus the twinning behavior observed in rectangular ⟨100⟩/{100} wires resulted from the change in cross sectional geometry does not apply to ⟨100⟩/{110} wires due to the inability to cause reorientation of the high energy {110} side surfaces.

The localized plastic deformation observed in ⟨100⟩/{110} nanowires is related to the crystallographic arrangement of the side surfaces. In the rectangular ⟨100⟩/{110} nanowire, the initial stacking fault initiated at the corner of the {100} surface. The stacking fault then moves to the surface and creates a surface step, or full dislocation. The surface step impedes the motion of partial dislocations and their resulting stack-

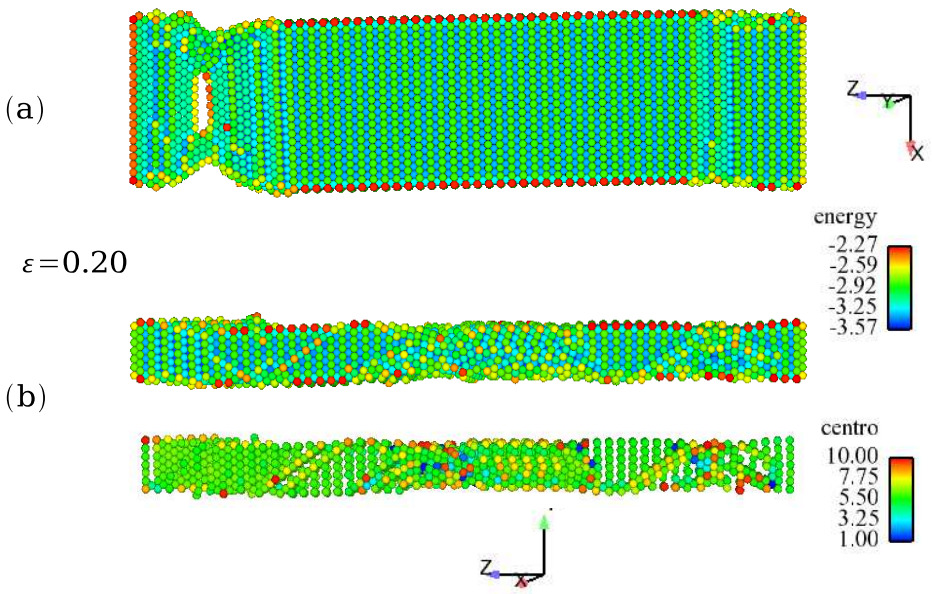

Figure 56: Snapshots of the tension of ⟨100⟩/{110} nanowires at a strain of ϵ=0.20. (a) 15 × 5; (b) 5 × 5. The first two images are constructed in potential energy with units of eV; the bottom image presents the atomic structure in centrosymmetry parameters [8].

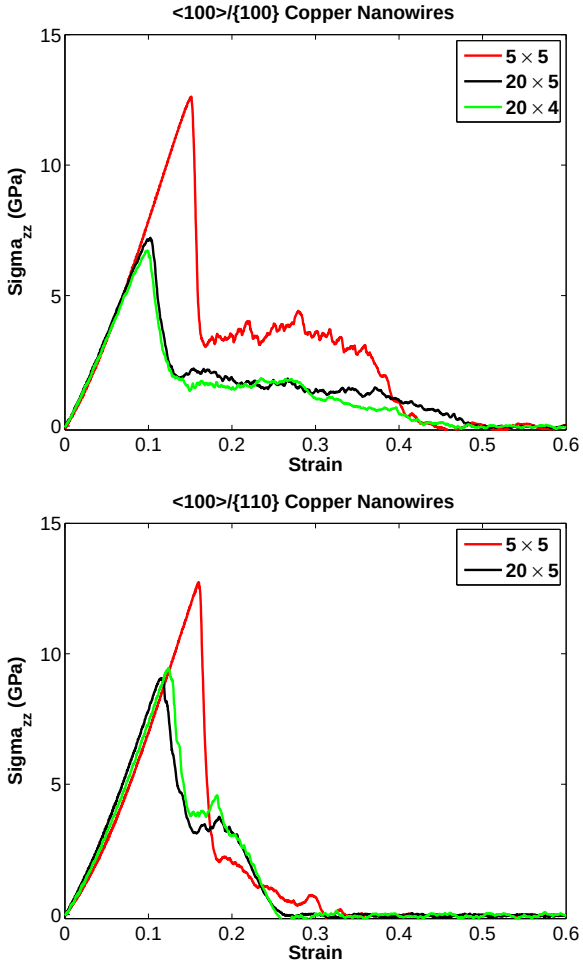

Figure 57: Tensile loaded stress-strain curves of copper nanowires: (a) ⟨100⟩/{100} wires; (b) ⟨100⟩/{110} wires.

ing faults, and thus the further deformation is restricted to a small volume around the surface step, leading to the localized fracture observed in Figure (56a).

The stress-strain curves of the tensile loaded ⟨100⟩ nanowires are presented in Figure (57). As is shown, the square ⟨100⟩/{100} nanowire with a 5 × 5 cross sectional dimension has an extremely large yield stress and strain compared to those of the rectangular ⟨100⟩/{100} nanowire with the 20 × 5 cross section. As shown in Figure (57a), the 5 × 5 wire yields at 12.6 GPa and the 20 × 5 yields at 7.2 GPa. This yields stress and strain disparity occurs for two reasons. First, smaller wires tend to relax/contract more due to surface stresses; therefore, they can sustain larger

Table 12: The toughness (T) of $\langle 100 \rangle$ metal nanowires under tension. The values are in units of GJ/m^3 and correspond to the wires in Table(10).

Orientation	1	2	3	4
$\langle 100 \rangle / \{100\}$	1.69	0.90	1.14	0.94
$\langle 100 \rangle / \{110\}$	1.12	1.02	0.89	0.92

stresses and strains before yielding [82]; It is noted recent work which has shown that surface area to volume ratio cannot explain the amount of relaxation that the nanowires undergo due to surface stresses [24].

The second, and more important reason is that different inelastic deformation mechanisms that cause distinct surface reorientations are active for the rectangular $\langle 100 \rangle / \{100\}$ nanowires. It is noted that the rectangular $\langle 100 \rangle / \{100\}$ nanowires deform via twinning, which occurs by the nucleation and propagation of successive partial dislocations. In contrast, the full dislocations that are observed in the square $\langle 100 \rangle / \{100\}$ nanowires are energetically unfavorable, leading to higher yield stresses in the square $\langle 100 \rangle / \{100\}$ nanowires. Furthermore, the rectangular nanowires lower their surface energy as the $\{100\}$ surfaces reorient to lower energy $\{111\}$ surfaces; the combination of the favorable surface reorientation and the less energetically costly defects result in the dramatically lower yield stress and strain for the rectangular $\langle 100 \rangle / \{100\}$ nanowires as observed in Figure (57a).

After the initial yield, the $\langle 100 \rangle \{100\}$ wires all exhibit a stress plateau of varying length, as shown in Figure (57a). The stress plateau for the 5×5 wire extends for about 18 percent strain, while the stress plateau has a magnitude of nearly 3.5 GPa. In contrast, the stress plateau for the 20×5 wire extends for about 26 percent strain, with a smaller stress magnitude of about 1.6 GPa. The longer stress plateau leads to a larger post-yield ductility, which results from the twinning-dominated behavior. The difference in the stress plateau magnitude is rooted in different deformation mechanisms: the larger stress plateau for the square nanowires occurs due to the

propagation of higher energy full and partial dislocations and the resulting stacking faults, while the lower stress plateau in the rectangular wires is due to relative mobility of the twin boundaries.

Due to the deformation via twinning, the fracture strain is larger in the rectangular $\langle 100 \rangle / \{100\}$ nanowires. As can be seen in Figure(57), the square wire breaks at a strain of around $\epsilon_f = 0.41$ and the rectangular 20×5 wire breaks at a strain of $\epsilon_f = 0.48$. The toughness, which is used to characterize the amount of absorbed energy density at the fracture point, is 0.94 GJ/m^3 for the rectangular 20×5 wire and 1.69 GJ/m^3 for the square 5×5 wire. The toughness of the square wire is larger despite the smaller fracture strain due to the larger yield stress, strain and post-yield stress plateau resulting from the higher energy defects present in the wire.

The stress-strain curves of the $\langle 100 \rangle / \{110\}$ wires are presented in Figure (57b). The square 5×5 wire yields at 12.6 GPa, while the rectangular 20×5 wire yields at 9 GPa. In the post-yield deformation, no propagation of stacking faults is observed and thus there is no obvious stress plateau in $\langle 100 \rangle / \{110\}$ wire, leading to brittle fracture around $\epsilon_f = 0.30$ for both square and rectangular wires. Due to the brittle failure mode, the square $\langle 100 \rangle / \{110\}$ wires have a smaller toughness of 1.12 GJ/m^3 as compared to the corresponding $\langle 100 \rangle / \{100\}$ wires, while the rectangular $\langle 100 \rangle / \{110\}$ wires, due to their elevated yield stress and strain, have a similar toughness of 0.92 GJ/m^3 as compared to the rectangular $\langle 100 \rangle / \{100\}$ wires.

V.3.2 Tension of $\langle 110 \rangle / \{100\}\{110\}$ and $\langle 110 \rangle / \{110\}\{112\}$ Nanowires

This section now presents the simulation results on the tensile loaded $\langle 110 \rangle$ nanowires, including both $\langle 110 \rangle / \{100\}\{110\}$ and $\langle 110 \rangle / \{110\}\{112\}$ configurations. The dimensions of these nanowires are shown in Table (11). Since each wire has two different surface orientations present, two different rectangular configurations are considered for each wire to illustrate the influence of each side surface orientation.

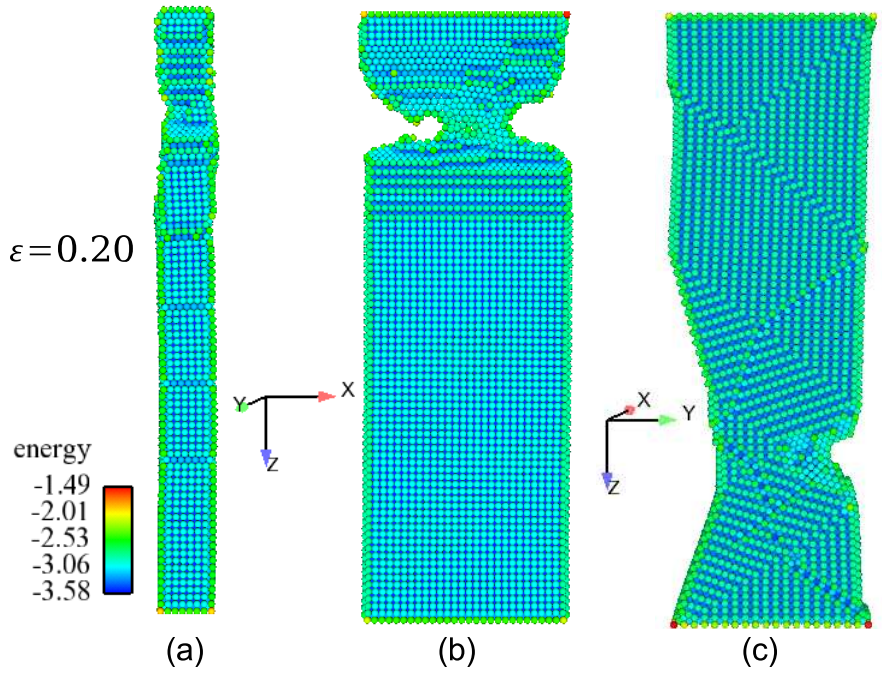

Figure 58: Snapshots of the tensile deformation $\langle 110\rangle/\{100\}\{110\}$ nanowires at a strain of $\epsilon = 0.20$. (a) 5×5 (b) 20×5 (c) 5×20. Potential energy is in units of eV.

Representative snapshots of the inelastic deformation of three $\langle 110\rangle/\{100\}\{110\}$ nanowires are illustrated in Figure (58). The rectangular nanowires depicted in Figure (58b) and (58c) have cross sectional dimensions of 20×5, and thus large $\{100\}$ side surfaces, and 5×20, which has large $\{110\}$ side surfaces. As is shown, the three wires exhibit distinct deformation modes at a strain of $\epsilon = 0.20$. The square nanowire with cross sectional dimensions of 5×5 accommodates the plastic deformation by the slip of full and partial dislocations, resulting in distributed stacking faults along the wire length direction. Unlike the deformation seen in the square cross section $\langle 100\rangle$ nanowires, these distributed stacking faults are immobile along the wire length, leading to localized necking in the post-yield deformation period and thus a small fracture strain.

The rectangular nanowire with large $\{100\}$ side surfaces, 20×5, exhibits localized plastic deformation. As is shown in Figure (58b), at the strain of ϵ=0.20, the wire has

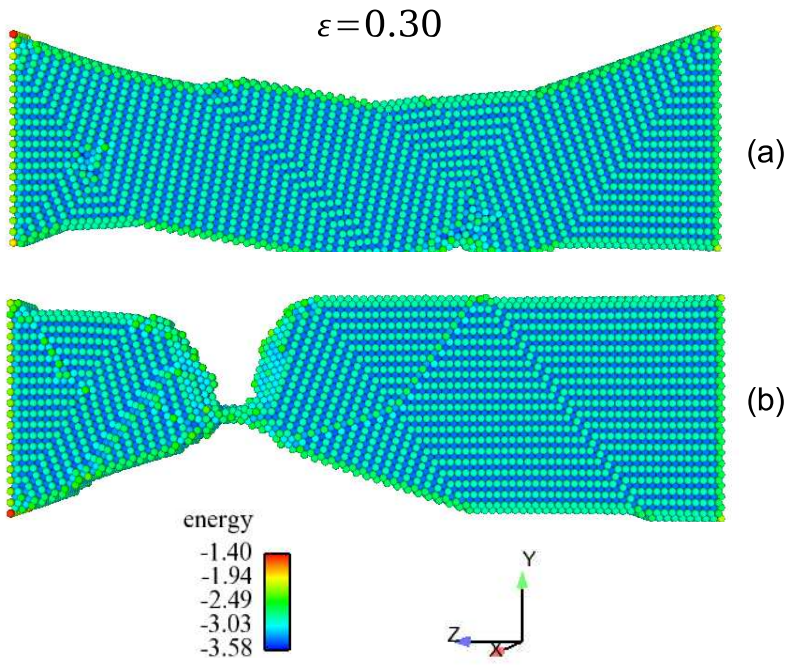

Figure 59: Snapshots of two tensile loaded ⟨110⟩/{100}{110} nanowires with large {110} surfaces. (a) 4 × 20; (b) 5 × 20. Potential energy is in units of eV.

a perfect crystal structure everywhere except at region of local deformation, resulting in a small fracture strain. By examining the deformation process, it is found that the stacking faults that nucleate from the {100} surfaces move and annihilate due to the surface crystallographic structure, results in a surface step on {100} surfaces. This surface step decreases the mobility of stacking faults and results in a localized deformation. Thus the low ductility property of this rectangular wire is attributed to the side surface crystallographic structure.

The 5 × 20 rectangular wire with large {110} side surfaces exhibits a different deformation behavior under tensile loading. As shown in Figure (58c), portions of the large {110} side surface rotate due to the tensile loading and form a new {110} facet on a different crystal variant. This newly-formed {110} facet is separated from the initial facet by a twin boundary, as shown in Figure (58c). The rotation of the {110} surface causes a reorientation of the small {100} side surfaces to become {110}

surfaces. Overall, due to the influence of small {100} side surfaces, the twinning-dominated reorientation was interrupted by a localized fracture in the post-yield period, as shown in Figure (58c). To further reduce the influence of {100} side surfaces, another simulation is performed on a rectangular ⟨110⟩/{100}{110} nanowire with a dimension of 4×20, one layer thinner than the 5×20 nanowire. As is shown in Figure(59), the thin wire displayed a more organized twinning, leading to a fracture strain as high as $\epsilon_f = 0.6$. Thus the thickness reduction does have a great influence on the deformation modes of metal nanowires by minimizing the influence of the {100} surfaces.

The stress-strain curves of the ⟨110⟩/{100}{110} wires are presented in Figure (60a). As is shown, the rectangular 20×5 wire with large {100} surfaces has a high yield stress, 6.3 GPa, which is similar to that of the square nanowire, 6.0 GPa, while the 5×20 wire with large {110} surfaces exhibits a small yield stress, 4.1GPa. The similar yield stress of the square nanowire and the rectangular wires with large {100} surfaces can be attributed to the same yield mechanism, slip of higher energy full and lower energy partial dislocations, and the small difference in relaxation strain along the ⟨110⟩ orientation. In contrast, the the lower yield stress of the rectangular wires with large {110} surfaces is due to the twinning-dominated deformation, which is characterized by the nucleation and propagation of energetically favorable partial dislocations.

In the post-yield period of ⟨110⟩/{100}{110} wires, the 5×5 and 20×5 wires exhibit a fracture strain of $\epsilon_f = 0.25$ due to the localized deformation, while the fracture strain of the 20×5 wire is around $\epsilon_f = 0.32$, where the increase in fracture strain is due to the twinning-dominated deformation, as shown in Figure (58c). The magnitude of fracture strain can be further improved by reducing the wire thickness, which minimizes the influence of the {100} surfaces. As shown in Table (13), the toughness is low for the rectangular 20×5 wire due to the small fracture strain re-

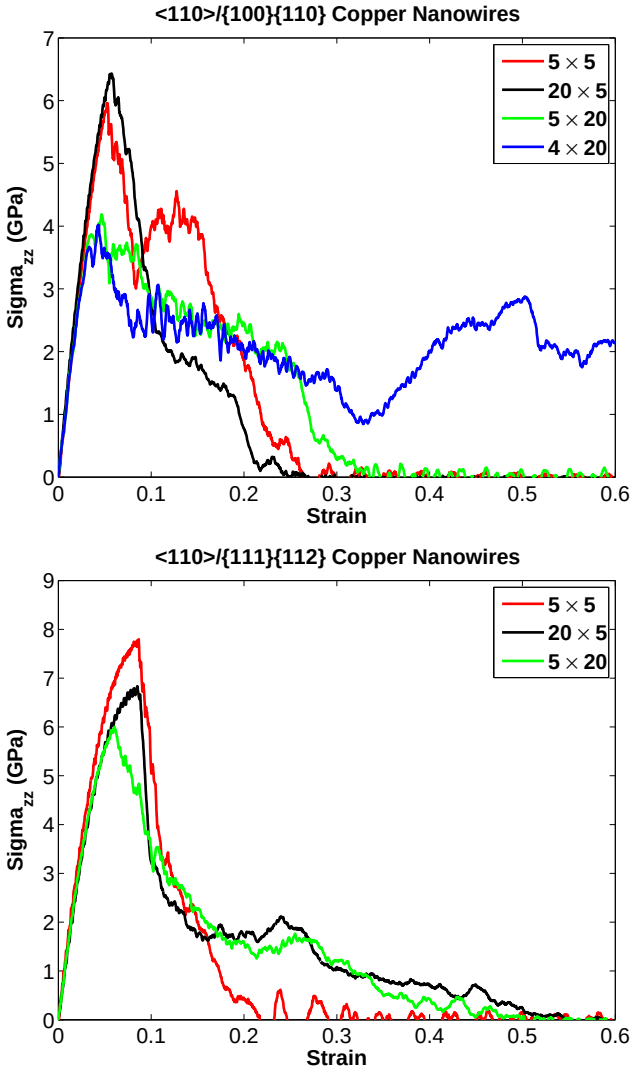

Figure 60: Stress-strain curves of tensile loaded ⟨110⟩ copper nanowires: (a) ⟨110⟩/{100}{110} wires; (b) ⟨110⟩/{111}{112} wires.

Table 13: Strain energy absorbed by the nanowires at fracture. The values correspond to the wires in Table (11).

Orientation	1	2	3	4	5	6	7
⟨110⟩/{100}{110}	0.58	0.96	0.78	0.75	1.35	0.68	0.71
⟨110⟩/{112}{111}	0.94	0.81	0.76	0.72	0.68	0.80	0.87

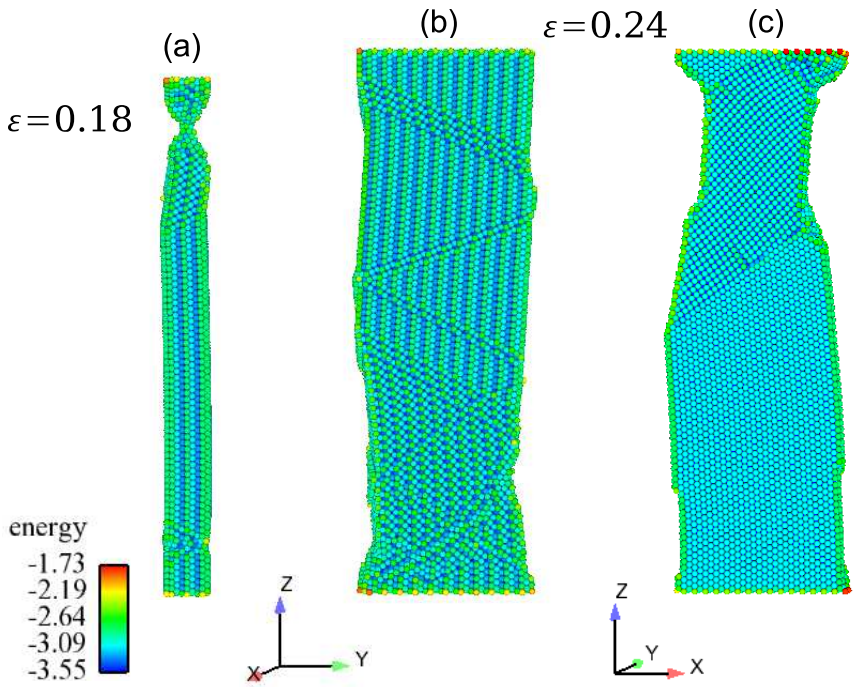

Figure 61: Snapshots of the tensile deformation of ⟨110⟩/{111}{112} nanowires: (a) 5 × 5; (b) 20 × 5; (c) 5 × 20. Potential energy is in units of eV.

sulting from the localized deformation, while for the 5 × 20 wire, the high toughness is due to the large fracture strain resulted from the twinning deformation. In general, the toughness does not appear to vary greatly between square and rectangular geometries for ⟨110⟩/{100}{110} nanowires.

This section now considers the inelastic deformation modes of the tensile loaded ⟨110⟩/{111}{112} nanowires. Representative snapshots of these nanowires are displayed in Figure (61). As is shown, these three nanowires exhibit three distinct inelastic deformation modes. The square nanowire deforms plastically by showing localized

deformation which leads to a small fracture strain. The rectangular 20 × 5 nanowire with large {112} side surfaces exhibits a loading-induced surface reorientation from {111} to {100} on the small side surfaces and {112} to a high index orientation on large side surfaces as shown in Figure (61b). The rectangular 5 × 20 nanowire with large {111} surfaces exhibits a surface reorientation with the {111} surfaces reorienting to {100} surfaces due to the tensile loading; a similar reorientation has been shown to lead to shape memory and pseudoelastic properties in rhombic ⟨110⟩/{111} nanowires [50, 87]. As shown in Figure (61c), at a strain of ϵ =0.18, the nanowire show a reoriented {100} facet, which is separated from the remaining {111} surface by a twin boundary layer. Thus the two rectangular ⟨110⟩/{111}{112} nanowires exhibit deformation twins under tension.

Stress-strain curves of ⟨110⟩/{111}{112} nanowires are presented in Figure (60b). As is shown, the square nanowire has a high yield stress, 7.8GPa, followed by the rectangular 20 × 5 wire with large {112} surfaces, 6.8GPa, and the 5 × 20 wire with large {111} surface has the smallest yield stress, 6.0GPa. The high yield stress in the square nanowire is related to the slip of energetically unfavorable full dislocations. More interestingly, the rectangular ⟨110⟩/{111}{112} nanowires have yield strengths that are similar to that of the square nanowire, as shown in Figure (60b). The reason for this is that the tensile-induced surface reorientation is from a lower energy {111} surface to a higher energy {100} surface; despite the low stress needed to nucleate and propagate the twin boundaries in those wires, the fact that the surface orientation changes from a low energy and extremely stable structure to a higher energy enables the rectangular ⟨110⟩/{111}{112} nanowires to have yield stresses, 6.8GPa, which is comparable to the value of the square ⟨110⟩/{111}{112} nanowire, 7.8GPa.

In the post-yield period, the localized deformation behavior in the square nanowire leads to a small fracture strain of about $\epsilon_f = 0.22$, while the two rectangular wires fracture at a strain of about ϵ_f=0.45 due to the twinning-dominated reorientation.

The toughness of these nanowires is summarized in Table (13), which shows that the toughness of the square nanowire is 0.72 GJ/m^3, while the toughness of the rectangular wires is much higher. Again, the high toughness is due to the energetically unfavorable reorientation of low energy {111} surfaces to {100} surfaces in conjunction with the ductile failure due to the nucleation and propagation of mobile twin boundaries.

V.3.3 Inelastic behavior of ⟨100⟩ wires under compression

Deformation modes of square ⟨100⟩/{100} and ⟨100⟩/{110} metal nanowires under compression have been documented in the literature [85]. It has been demonstrated that under compression, the ⟨100⟩/{100} nanowire accommodates plastic deformation by nucleation and propagation of twin boundary layers, resulting in a ⟨110⟩ wire with exposed {111} side surfaces; while the square ⟨100⟩/{110} wire shows parallel stacking fault structures during compressive deformation with spatially distributed stacking faults.

As is shown in Figure(62), the rectangular ⟨100⟩/{110} nanowire accommodes plastic deformation with the nucleation and propagation of twin boundaries, which leads to {100} facets on large side surfaces and {110} on small side surfaces. In the reorientation, the resultant {100} facet is exclusively on large side surfaces. This can be attributed to the fact, $E_{100} < E_{110}$, and thus the exposure of {100} surfaces provides additional driving force for the continuation of plastic deformation. The rectangular ⟨100⟩/{100} wire exhibits twinning-dominated reorientation, resulting in {111} facets on all side surfaces. The difference in deformation modes of rectangular nanowires under the compressive loading is mainly attributed to the crystallographic confinement of side surfaces.

The stress curves of compressively-loaded ⟨100⟩ nanowires are presented in Figure(63). As is shown, the square nanowire has a lower yield stress and yield strain compared to the corresponding rectangular nanowire due to the small cross sectional size and thus

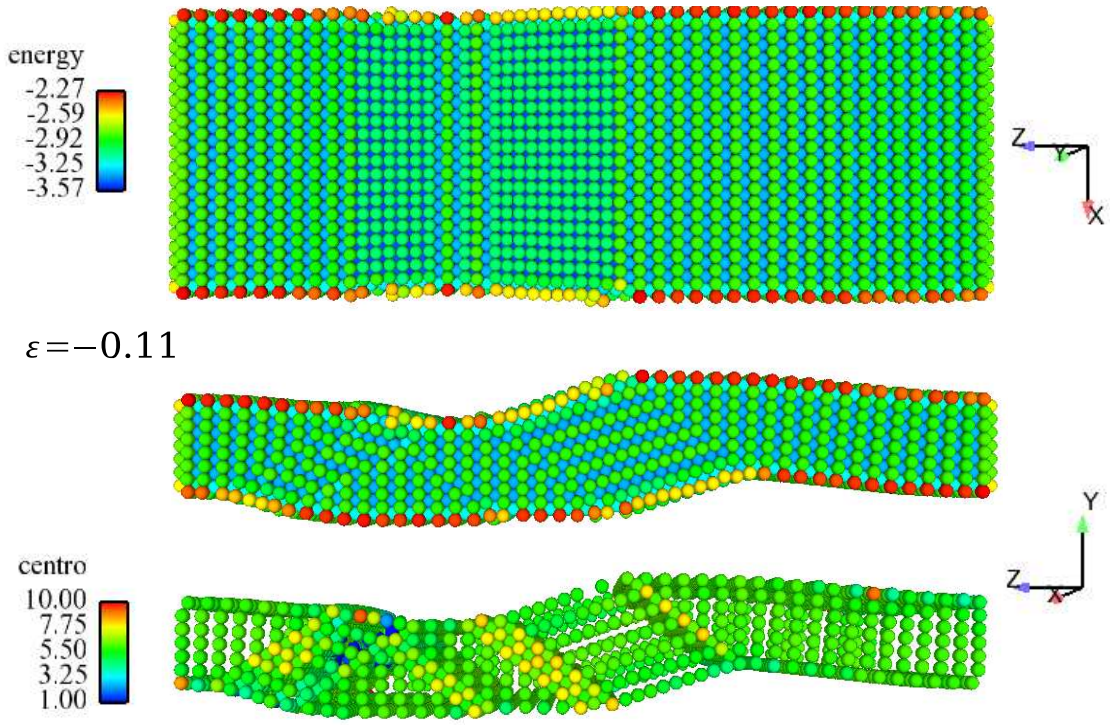

Figure 62: Snapshots of the compression of a 20 × 5 ⟨100⟩/{110} nanowires at a strain of ϵ=-0.11. The upper one is on potential energy in units of eV, and the lower one is in centrosymmetry parameter [8].

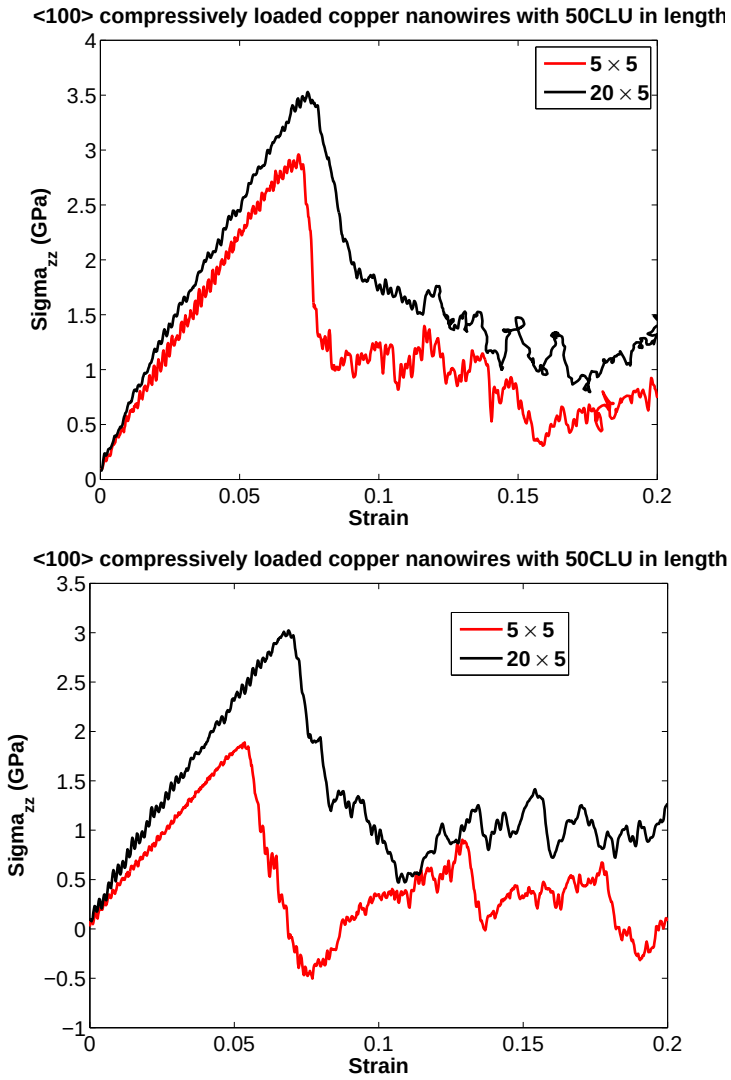

Figure 63: Compressively loaded stress-strain curves of copper nanowires: (a) $\langle 100 \rangle / \{100\}$ wires; (b) $\langle 100 \rangle / \{110\}$ wires.

the large relaxation strain. By comparing the magnitude of yield stress and strain in compression and tension, it can be found the asymmetry property in uniaxial loaded nanowire, which is resulted from the large relaxation strain at nanoscale. Another observation that needs to mention is that for the square nanowires, the wire with {100} yields at 2.9GPa, while the wire with {110} yields at 1.8GPa. The difference can be attributed to the different relaxation strain resulted from different side surface facets.

CHAPTER VI

CONCLUSIONS AND FUTURE RESEARCH DIRECTIONS

In this chapter, a summary of the research conclusions of this thesis will be presented, including SMNWs, surface elasticity, and coupled effects of geometry and surface orientations. Then several suggestions on future research topics will be given as a conclusion of this chapter.

VI.1 Summary and conclusions

In this thesis, the emphasis is laid on the influence of free surfaces on the mechanical properties and deformation mechanisms of FCC metal nanowires. By using atomistic simulations with EAM potentials, the impact of the wire surface orientations and loading conditions on the deformation mechanisms has been studied and characterized. The loading conditions include various loading rates, different heat transfer conditions and testing temperature for the analysis of the SMNWs. Four different side surface combinations were used when analyzing the surface elasticity and coupled effects.

In the discussions of SMNWs in Chapter 3, two groups of wires, including defect-free and defective nanowires, were studied and compared to polycrystalline SMAs. Several key findings in the defect-free nanowires are : (1) The shape memory and pseudoelasticity behavior in SMNWs are realized through the reversibility of twin boundaries between the high energy $\langle 100\rangle/\{100\}$ and the low energy $\langle 110\rangle/\{111\}$ orientations. (2) The SMNWs exhibit superior mechanical properties as compared to polycrystalline SMAs, including elevated transformation stresses, higher tensile stresses, and larger reversible strains. (3) The quality of heat transfer with ambi-

ent environment will be critical for the practical usage of SMNWs because of the large temperature increase during the uniaxial loading. The wire with constant testing temperature is more stable. (4) The SMNW thermomechanical properties are fundamentally different in certain key respects to those observed previously in bulk, polycrystalline SMAs, such as the transformation stress variation trend with loading temperatures, endothermic and exothermic states in loading and unloading processes.

The major findings in defective SMNWs in Chapter 3 can be summarized as : (1) Though the reorientation was shown to be precluded in certain situations, notably at deformation temperatures approaching the critical reorientation temperature T_c and high applied strain rates, the defective nanowires in general demonstrated reversibility at lower strain rates and deformation temperatures. (2) Due to the existence of the initial $\{111\}$ stacking faults, reversibility between the $\langle 110\rangle/\{111\}$ and $\langle 100\rangle$ orientations was shown to occur by the propagation and annihilation of multiple twin boundaries. (3) While the transformation stresses and strains of the initially defective $\langle 110\rangle/\{111\}$ wires was reduced as compared to initially defect free $\langle 110\rangle/\{111\}$ wires, the formation and evolution of multiple twin boundaries during tensile loading led to non-constant and increased plateau stresses as compared to previous investigations of initially defect-free $\langle 110\rangle/\{111\}$ nanowires with a single propagating twin boundary. (4) If reorientation to the $\langle 100\rangle$ configuration occurred, the nanowires with initial defects showed no degradation in mechanical properties as compared to those without initial defects. (5) The interior defects in defective nanowires work like grain boundaries in bulk, polycrystalline SMAs.

A summary of the results on the surface elasticity of nanoboxes in Chapter 4 is presented as follows : (1) Knowledge of the relative strength of bulk material as compared to the surface can be utilized to create high strength, light weight nanostructures by removing the bulk material from the nanowires. The $\langle 100\rangle$ nanoboxes were found to be elastically softer than the corresponding solid $\langle 100\rangle$ nanowires; while

the ⟨110⟩ nanoboxes were elastically stronger than the corresponding solid nanowires. (2) The Young's modulus of ⟨110⟩ nanoboxes was found a 20% increase as compared to the corresponding solid nanowires, which is resulted from the fact that the ⟨110⟩ bulk is weaker than the corresponding ⟨110⟩ surfaces. (3) The yield strains for both ⟨100⟩ and ⟨110⟩ orientations were found to be lower than those of the corresponding solid nanowires. This is attributed to the larger amounts of surface area of nanoboxes as compared to solid wires, which contributes to a larger possibility of defect generation from surfaces and thus a lower yield strain. (4) The yield stress was found enhanced in ⟨110⟩ nanoboxes, while was reduced in ⟨100⟩ nanoboxes.

The work on the inelastic deformation of metal nanowires discussed in Chapter 5 has revealed the link of the deformation behavior, mechanical properties, and the wire geometry and surface orientations. The specific findings in this work can be summarized as : (1) Non-square nanowires generally exhibit lower yield stresses and strains, lower fracture toughness, elevated fracture strains and a propensity to deform via twinning. (2) The lower yield stresses and strains of rectangular nanowires generally arise due to the fact that they deform via twinning, which is due to the nucleation and propagation of mobile partial dislocations. In contrast, square nanowires tend to deform via both energetically favorable partial dislocations and energetically unfavorable full dislocations, which increases their yield properties. In ⟨100⟩ wires, the initial relaxation is another contribution to the high yield properties in square nanowires. (3) Rectangular wires that undergo a tensile-induced surface reorientation from a lower energy ({111}) to higher energy ({100}) surface tend to have yield properties that are comparable to the corresponding square wires; this occurs due to the work necessary to convert low energy surfaces to less stable and thus higher energy surfaces. Furthermore, this leads to those rectangular wires having fracture toughnesses and fracture strains that exceed those seen in the square nanowires.

VI.2 Future research topics

Several possible research topics deserve to be studied as a continuation of the thesis. In SMNWs, this work has revealed the main mechanisms of the uniaxial deformation behavior of SMNWs and the influence of initial interior defects on the mechanical properties of the nanowires. However, the practical use of the 1-D shape memory material may require repeated loading and unloading process, as observed in 1-D SMAs. Thus the fatigue properties of 1-D SMNWs should be characterized and studied for future. Also in the synthesis process, nanowires are vulnerable and easily to be oxidized, resulting in oxygen vacancies on nanowires [157]. This oxidation has been demonstrated to have a great impact on the performance of nanowire field effect [158]. First principle/ *ab initio* MD should be performed to study the possible influence on the mechanical properties of SMNWs.

The surface elasticity has revealed that the metal nanoboxes can exhibit reduced or enhanced mechanical properties compared to the corresponding solid nanowires. The thickness of the nanoboxes also has a strong impact on the mechanical properties. The method can be used to characterize the mechanical properties of metal nanotubes, which have attracted intense research activities recently [159–163]. In the synthesis of Ni nanotubes, it has been shown that the geometric parameter, such as length and thickness, can be controlled with experimental techniques [164]. Thus future work on surface elasticity can be focused on characterizing the influence of the geometry parameters, such as tube thickness, on mechanical properties of metal nanotubes.

The work of the coupled effects of geometry and surface facets has demonstrated several possible influences on the inelastic deformation behavior of metal nanowires. The discussions are mainly focused on the $\langle 100 \rangle$ and $\langle 110 \rangle$ nanowires. However, besides the $\langle 100 \rangle$ and $\langle 110 \rangle$ nanowires, $\langle 111 \rangle$ wires have also been observed in experiments, where the coupled effects on the inelastic mechanical properties should be characterized as well in future.

A very promising research direction is to study the influence of free surfaces on the mechanical properties of semiconductor nanomaterials, such as Si. Similar to the metal nanowires discussed in this thesis, the surface atomic structure governs the intrinsic stress in semiconductor materials and the influence of the intrinsic stress becomes increasingly prominent as the material size becomes smaller. The research on the semiconductor nanomaterials are of importance because they are compatible with current silicon technology utilized in chip industries and thus leads into the NMES from the current MEMS technology. Also the semiconductor materials have many more surface atomic structures compared to metals due to the surface reconstruction [165, 166] and then the surface influence on mechanical properties is more complicated. For example, the Si {100} surface has five common surface structures, ideal 1×1, symmetric 2×1, asymmetric 2×1, 2×2, and 4×2 [166]. More interestingly, it has been shown that a semiconductor nanofilm can be self-rolled into a tube structure due to the intrinsic surface stress [165]. Thus, the characterization on the surface stress effect in semiconductor nanomaterials will be an interesting research topic in future.

BIBLIOGRAPHY

[1] A F Voter. Embedded atom method potentials for seven fcc metals: Ni, Pd, Pt, Cu, Ag, Au, and Al. *Los Alamos Unclassified Technical Report*, LA-UR 93-3901, 1993.

[2] *www.cchem.berkeley.edu/ pdygrp/nanowire.htm.*

[3] *www.nature.com/physics/highlights/6996-2.html.*

[4] R C Cammarata. Surface and interface stress effects in thin films. *Progress in Surface Science*, 46(1):1–38, 1994.

[5] F H Streitz, R C Cammarata, and K Sieradzki. Surface-stress effects on elastic properties. I. Thin metal films. *Physical Review B*, 49(15):10699–10706, 1994.

[6] J Diao, K Gall, and M L Dunn. Surface stress driven reorientation of gold nanowires. *Physical Review B*, 70:075413, 2004.

[7] *www.tf.uni-kiel.de/matwis/amat/def_en/index.html.*

[8] C L Kelchner, S J Plimpton, and J C Hamilton. Dislocation nucleation and defect structure during surface indentation. *Physical Review B*, 58(17):11085–11088, 1998.

[9] J Y Luo, L M Tong, and Z Z Ye. Modeling of silica nanowires for optical sensing. *International Electronic Journal of Optics*, 13(6):2315–2140, 2005.

[10] A Graff, D Wagner, H Ditlbacher, and U Kreibig. Silver nanowires. *The European Physical Journal D*, 34:263–269, 2005.

[11] C M Lieber. Nanoscale science and technology: Building a big future from small things. *MRS Bulletin*, 28(7):486–491, 2003.

[12] Z L Wang. *Nanowires and Nanobelts, Materials, Properties and Devices. Volume I.* Kluwer Academic Publishers, 2003.

[13] L Tong, R R Gattass, J B Ashcom, S He, J Lou M Shen, I Maxwell, and E Mazur. subwavelength-diameter silica wires for low-loss optical wave guiding. *Nature*, 426(6968):816–819, 2003.

[14] N I Kovtyukhova and T E Mallouk. Nanowires and building blocks for self-assembling logic and memory circuits. *Chemistry-A European Journal*, 8(9):4355–4363, 2002.

[15] H Ditlbacher, A Hohenau, D Wagner, U Kreibig, M Rogers, F Hofer, F R Aussenegg, and J R Krenn. Silver nanowires as surface plasmon resonators. *Physical review letters*, 95:257403, 2005.

[16] F Patolsky and C M Lieber. Nanowires nanosensors. *Materials today*, pages 20–28, 2005.

[17] B J Wiley, Z Wang, J Wei, Y Yin, D H Cobden, and Y Xia. Surface step effects on nanoindentation. *Nano Letters*, 6(10):2273–2278, 2006.

[18] G Rubio, N Agrait, and S Vieira. Atomic-sized metallic contacts: Mechanical properties and electronic transport. *Physical Review Letters*, 76(13):2302–2305, 1996.

[19] H Ohnishi, Y Kondo, and K Takayanagi. Quantized conductance through individual rows of suspended gold atoms. *Nature*, 395:780–783, 1998.

[20] D M Lyons, K M Ryan, M A Morris, and J D Holmes. Tailoring the optical properties of silicon nanowire arrays through strain. *Nano Letters*, 2(8):811–816, 2002.

[21] G Audoit, E N Mhuircheartaigh, S M Lipson, M A Morris, W J Blau, and J D Holmes. Strain induced photoluminescence from silicon and germanium nanowire arrays. *Journal of Materials Chemistry*, 15:4809–4815, 2005.

[22] F Buda, J Kohanoff, and M Parrinello. Optical properties of porous silicon: a first-principles study. *Physical Review Letters*, 69(8):1272–1275, 1992.

[23] L E Brus, P F Szajowski, W L Wilson, T D Harris, S Schuppler, and P H Citrin. Electronic spectroscopy and photophysics of Si nanocrystals: relationship to bulk c-Si and porous Si. *Journal of the American Chemical Society*, 117:2915–2922, 1995.

[24] H S Park and P A Klein. A surface cauchy-born model for FCC metal nanostructures. *Physical Review B*, 75:085408, 2007.

[25] J Diao, K Gall, and M L Dunn. Surface-stress-induced phase transformation in metal nanowires. *Nature Materials*, 2(10):656–660, 2003.

[26] L G Zhou and H Huang. Are surfaces elastically softer or stiffer? *Applied Physics Letters*, 84(11):1940–1942, 2004.

[27] H Liang, M Upmanyu, and H Huang. Size-dependent elasticity of nanowires: nonlinear effects. *Physical Review B*, 71:241403(R), 2005.

[28] H S Park and P A Klein. Surface stress effects on the resonant properties of fixed/fixed metal nanowires. *Physical Review B*, 2007. Submitted.

[29] J W Gibbs. *The scientific papers of J. Willard Gibbs*. Longmans-Green, London, 1906.

[30] R Shuttleworth. The surface tension of solids. *Proc. Phys. Soc.*, 63:444–457, 1950.

[31] F Spaepen. Interfaces and stresses in thin films. *Acta Materialia*, 48:31–42, 2000.

[32] D W Carr, S Evoy, L Sekaric, H G Craighead, and J M Parpia. Measurement of mechanical resonance and losses in nanometer scale silicon wires. *Applied Physics Letters*, 75(7):920–922, 1999.

[33] T D Stowe, K Yasumura, T W Kenny, D Botkin, K Wago, and D Rugar. Attonewton force detection using ultrathin silicon cantilevers. *Applied Physics Letters*, 71(2):288–290, 1997.

[34] J Yang, T Ono, and M Esashi. Surface effects and high quality factors in ultrathin single-crystal silicon cantilevers. *Applied Physics Letters*, 77(23):3860–3862, 2000.

[35] D Li, Y Wu, P Kim, L Shi, P Yang, and A Majumdar. Thermal conductivity of individual silicon nanowires. *Applied Physics Letters*, 83(14):2934–2936, 2003.

[36] E W Wong, P E Sheehan, and C M Lieber. Nanobeam mechanics: elasticity, strength, and toughness of nanorods and nanotubes. *Science*, 277:1971–1975, 1997.

[37] S Cuenot, C Frétigny, S Demoustier-Champagne, and B Nysten. Surface tension effect on the mechanical properties of nanomaterials measured by atomic force microscopy. *Physical Review B*, 69:165410, 2004.

[38] B Wu, A Heidelberg, and J J Boland. Mechanical properties of ultrahigh-strength gold nanowires. *Nature Materials*, 4:525–529, 2005.

[39] G Y Jing, H L Duan, X M Sun, Z S Zhang, J Xu, Y D Li, J X Wang, and D P Yu. Surface effects on elastic properties of silver nanowires: contact atomic-force microscopy. *Physical Review B*, 73:235409, 2006.

[40] V B Shenoy. Atomistic calculations of elastic properties of metallic FCC crystal surfaces. *Physical Review B*, 71:094104, 2005.

[41] G Gioia and X Dai. Surface stress and reversing size effect in the initial yielding of ultrathin films. *Journal of Applied Mechanics*, 73:254, 2006.

[42] S J Zhou, A E Carlsson, and R Thomson. Crack blunting effects on dislocation emission from cracks. *Physical Review Letters*, 72(6):852, 1994.

[43] K Sieradzki and R C Cammarata. Surface stress effects on the ductile to brittle transition. *Physical Review Letters*, 73(7):1049, 1994.

[44] J A Zimmerman, C. L. Kelchner, P. A. Klein, J. C. Hamilton, and S. M. Foiles. Surface step effects on nanoindentation. *Physical Review Letters*, 87(16):165507, 2001.

[45] W W Mullins. Solid surface morphologies governed by capillarity. *in Metal Surfaces: Structure, Energetics and Kinetics*, page 17, 1963.

[46] S P Chen, A F Voter, and D J Srolovitz. Oscillatory surface relaxations in Ni, Al, and their ordered alloys. *Physical Review Letters*, 57(11):1308–1311, 1986.

[47] R Dingreville, J Qu, and M Cherkaoui. Surface free energy and its effect on the elastic behavior of nano-sized particles, wires and films. *Journal of the Mechanics and Physics of Solids*, 53:1827–1854, 2005.

[48] Y Kondo, Q Ru, and K Takayanagi. Thickness induced structural phase transition of gold nanofilm. *Physical Review Letters*, 82(4):751–754, 1999.

[49] A Hasmy and E Medina. Thickness induced structural transition in suspended FCC metal nanofilms. *Physical Review Letters*, 88(9):096103, 2002.

[50] H S Park, K Gall, and J A Zimmerman. Shape memory and pseudoelasticity in metal nanowires. *Physical Review Letters*, 95:255504, 2005.

[51] L Vitos, A V Ruban, H L Skriver, and J Kollar. The surface energy of metals. *Surface Science*, 411:186–202, 1998.

[52] J Diao, K Gall, and M L Dunn. Yield asymmetry in metal nanowires. *Nano Letters*, 4(10):1863–1867, 2004.

[53] K Gall, J Diao, M L Dunn, M Haftel, N Bernstein, and M J Mehl. Tetragonal phase transformation in gold nanowires. *Journal of Engineering Materials and Technology*, 127:417–422, 2005.

[54] Y Wang, S Teitel, and C Dellago. Surface-driven bulk reorientation of gold nanorods. *Nano Letters*, 5(11):2174–2178, 2005.

[55] W Liang and M Zhou. Atomistic simulations reveal shape memory of fcc metal nanowires. *Physical Review B*, 73:115409, 2006.

[56] J Diao. Atomistic and continuum modeling of the structure and mechanical properties of metal nanowires. *Ph.D. Thesis*, page University of Colorado at Boulder, 2004.

[57] G Brambilla, F Xu, and X Feng. Fabrication of optical fibre nanowires and their optical and mechanical characterization. *Electronics Letters*, 42(9):517–519, 2006.

[58] A Shik, H E Ruda, and I G Currie. Electromechanical and electro-optical properties of nanowires. *Journal of Applied Physics*, 98:094306, 2005.

[59] H Mehrez and S Ciraci. Yielding and fracture mechanisms of nanowires. *Physical Review B*, 56(19):12632–12642, 1997.

[60] H Ikeda, Y Qi, T Cagin, K Samwer, W L Johnson, and W A Goddard III. Strain rate induced amorphization in metallic nanowires. *Physical Review Letters*, 82(14):2900–2903, 1999.

[61] E C C M Silva, L Tong, S Yip, and K J Van Vliet. Size effects on the stiffness of silica nanowires. *Small*, 2(2):239–243, 2006.

[62] A Heidelberg, LT Ngo, B Wu, M A Phillips, S Sharma, T I Kamins, J E Sader, and J J Boland. A generalized description of the elastic properties of nanowires. *Nano Letters*, 6(6):1101–1106, 2006.

[63] M T Azar, M Nassirou, R Wang, S Sharma, T I Kamins, M S Islam, and R S Williams. Mechanical properties of self-welded silicon nanobridges. *Applied Physics Letters*, 87:113102, 2005.

[64] D A Dikin, X Chen, W Ding, G Wagner, and R S Ruoff. Resonance vibration of amorphous sio2 nanowires driven by mechanical or electrical field excitation. *Journal of Applied Physics*, 93(1):226–230, 2002.

[65] NA Stalder and U Durig. Study of yielding mechanics in nanometer-sized au contacts. *Applied physics letters*, 68:637–639, 1996.

[66] A I Yanson, G R Bollinger, H E van der Borm, N Agrait, and J M van Ruitenbeek. Formation and manipulation of a metallic wire of single gold atoms. *Nature*, 395:783–785, 1998.

[67] D Sanchez-Portal, E Artacho, J Junquera, P Ordejon, A Garcia, and J M Soler. Stiff monatomic gold wires with a spinning zigzag geometry. *Physical Review Letters*, 83(19):3884–3887, 1999.

[68] C-H Zhang, F Kassubek, and C A Stafford. Surface fluctuations and the stability of metal nanowires. *Physical Review B*, 68:165414, 2003.

[69] H S Park and J A Zimmerman. Modeling inelasticity and failure in gold nanowires. *Physical Review B*, 72:054106, 2005.

[70] J A Torres, E Tosatti, A Dal Corso, F Ercolessi, J J Kohanoff, F D Di Tolla, and J M Soler. The puzzling stability of monatomic gold wires. *Surface Science Letters*, 426:L441–L446, 1999.

[71] E A Jagla and E Tosatti. Structure and evolution of a metallic nanowire-tip junction. *Physical Review B*, 64:205412, 2001.

[72] E Z da Silva, A J R da Silva, and A Fazzio. How do gold nanowires break? *Physical Review Letters*, 87(25):256102, 2001.

[73] Y Kondo and K Takayanagi. Gold nanobridge stabilized by surface structure. *Physical Review Letters*, 79(18):3455–3458, 1997.

[74] P Z Coura, S G Legoas, A S Moreira, F Sato, V Rodrigues, S O Dantas, D Ugarte, and D S Galvao. On the structural and stability features of linear atomic suspended chains formed from gold nanowires stretching. *Nano Letters*, 4(7):1187–1191, 2004.

[75] P S Branicio and J P Rino. Large deformation and amorphization or Ni nanowires under uniaxial strain: a molecular dynamics study. *Physical Review B*, 62(24):16950–16955, 2000.

[76] J-W Kang and H-J Hwang. Mechanical deformation study of copper nanowires using atomistic simulation. *Nanotechnology*, 12:295–300, 2001.

[77] B Wang, D Shi, J Jia, G Wang, X Chen, and J Zhao. Elastic and plastic deformations of nickel nanowires under uniaxial compression. *Physica E*, 30:45–50, 2005.

[78] H A Wu, A K Soh, X X Wang, and Z H Sun. Strength and fracture of single crystal metal nanowire. *Key Engineering Materials*, 261-263:33–38, 2004.

[79] W Liang and M Zhou. Response of copper nanowires in dynamic tensile deformation. *Proceedings of the Institution of Mechanical Engineers, Part C: Journal of Mechanical Engineering Science*, 218(6):599–606, 2004.

[80] S J A Koh, H P Lee, and Q H Cheng. Molecular dynamics simulation of s solid platinum nanowire under uniaxial tensile strain: temperature and strain rate effects. *Physical Review B*, 72:085414–085424, 2005.

[81] C Ji and H S Park. Geometric effects on the inelastic deformation of metal nanowires. *Applied Physics Letters*, 89:181916, 2006.

[82] K Gall, J Diao, and M L Dunn. The strength of gold nanowires. *Nano Letters*, 4(12):2431–2436, 2004.

[83] P Walsh, W Li, R K Kalia, A Nakano, P Vashista, and S Saini. Structural transformation, amorphization, and fracture in nanowires: A multimillion-atom molecular dynamics study. *Applied Physics Letters*, 78(21):3328–3330, 2001.

[84] H S Park and J A Zimmerman. Stable nanobridge formation in $\langle 110 \rangle$ gold nanowires under tensile deformation. *Scripta Materialia*, 54(6):1127–1132, 2006.

[85] H S Park, K Gall, and J A Zimmerman. Deformation of FCC nanowires by twinning and slip. *Journal of the Mechanics and Physics of Solids*, 54(9):1862–1881, 2006.

[86] W Liang and M Zhou. Pseudoelasticity of single crystalline Cu nanowires through reversible lattice reorientations. *Journal of Engineering Materials and Technology*, 127(4):423–433, 2005.

[87] W Liang, M Zhou, and F Ke. Shape memory effect in Cu nanowires. *Nano Letters*, 5(10):2039–2043, 2005.

[88] H S Park and C Ji. On the thermomechanical deformation of silver shape memory nanowires. *Acta Materialia*, 54(10):2645–2654, 2006.

[89] C Ji and H S Park. On the role of defects on the uniaxial tensile deformation of silver shape memory nanowires. *Journal of Computational and Theoretical Nanoscience*, 4:578–587, 2007.

[90] M I Haftel and K Gall. Density functional theory investigation of surface-stress-induced phase transformations in fcc metal nanowires. *Physical Review B*, 74:035420, 2006.

[91] H S Park. Stress-induced martensitic phase transformation in intermetallic nickel aluminum nanowires. *Nano Letters*, 6(5):958–962, 2006.

[92] C Ji and H Park. Characterizing the elasticity of hollow metal nanowires. *Nanotechnology*, 18:115707, 2007.

[93] C Ji and H Park. The coupled effects of geometry and surface orientation on the mechanical properties of metal nanowires. *Nanotechnology*, 18:305704, 2007.

[94] J P Hirthe and J Lothe. *Theory of Dislocations - Second Edition*. Krieger Publishing Company, 1982.

[95] D Frenkel and B Smit. *Understanding Molecular Simulation: From Algorithms to Applications*. Academic Press, 2001.

[96] L Verlet. Computer experiment on classical fluids. i thermodynamicall properties of lennard-jones molecules. *Physics Review*, 159:98–103, 1967.

[97] J A Zimmerman. Continuum and atomistic modeling of dislocation nucleation at crystal surface ledges. *Ph.D. Thesis*, page Stanford University, 1999.

[98] J M Haile. *Molecular Dynamics Simulations*. Wiley and Sons, 1992.

[99] Jonathan Richard Shewchuk. An introduction to the conjugate gradient method without the agonizing pain. 1994.

[100] S Nosé. A unified formulation of the constant temperature molecular dynamics methods. *Journal of Chemical Physics*, 81:511–519, 1984.

[101] S Nosé. A molecular dynamics method for simulation in the canonical ensemble. *Molecular Physics*, 52(9):225–268, 1984.

[102] W G Hoover. Canonical dynamics: Equilibrium phase-space distributions. *Physical Review A*, 31:1695–1697, 1985.

[103] W G Hoover. Constant pressure equation of motion. *Physical Review A*, 34:2499–2500, 1986.

[104] M S Daw and M I Baskes. Semi-empirical, quantum mechanical calculation of hydrogen embrittlement in metals. *Physical Review Letters*, 50:1285–1288, 1983.

[105] M S Daw and M I Baskes. Embedded-atom method: Derivation and application to impurities, surfaces, and other defects in metals. *Physical Review B*, 29(12):6443–6453, 1984.

[106] S M Foiles, M L Baskes, and M S Daw. Embedded-atom-method functions for the FCC metals Cu, Ag, Au, Ni, Pd, Pt, and their alloys. *Physical Review B*, 33(12):7893–7991, 1986.

[107] M S Daw. Model of metallic cohesion: The embedded-atom method. *Physical Review B*, 39:7441–7452, 1989.

[108] M S Daw, S M Foiles, and M I Baskes. The embedded-atom method: a review of theory and applications. *Materials Science Reports*, 9:251–310, 1993.

[109] M I Baskes. Modified embedded-atom potentials for cubic materials and impurities. *Physical Review B*, 45(5):2727–2742, 1992.

[110] A F Voter and S P Chen. Accurate interatomic potentials for Ni, Al and Ni_3Al. *Materials Research Society Symposium Proceedings*, 82:175–180, 1987.

[111] Y Mishin, M J Mehl, D A Papaconstantopoulos, A F Voter, and J D Kress. Structural stability and lattice defects in copper: *ab initio*, tight-binding, and embedded-atom calculations. *Physical Review B*, 63:224106, 2001.

[112] J A Zimmerman, H Gao, and F F Abraham. Generalized stacking fault energies for embedded atom FCC metals. *Modelling and Simulation in Materials Science and Engineering*, 8:103–115, 2000.

[113] R Clausium. On a mechanical theory applicable to heat. *Philosophical Magazine*, 40:122–127, 1870.

[114] J A Zimmerman, R E Jones, P A Klein, D J Bamann, E B Webb III, and J J Hoyt. Continuum definitions for stress in atomistic simulation. *Sandia National Lab Report*, SAND2002-8608, 2002.

[115] M Zhou. A new look at the atomic level virial stress: on continuum-molecular equivalence. *Proceedings of the Royal Society of London Series A-Mathematical, Physical and Engineering Sciences*, 459:2347–2392, 2003.

[116] J A Zimmerman, E B Web III, J J Hoyt, R E Jones, P A Klein, and D J Bammann. Calculation of stress in atomistic simulation. *Modelling and Simulation in Materials Science and Engineering*, 12:S319–S332, 2004.

[117] J A Shaw and S Kyriakides. Thermomechanical aspects of NiTi. *Journal of the Mechanics and Physics of Solids*, 43(8):1243–1281, 1995.

[118] D A Hebda and S R White. Effect of training conditions and extended thermal cycling on nitinol two-way shape memory behavior. *Smart Materials and Structures*, 4:298–304, 1995.

[119] J A Shaw and S Kyriakides. On the nucleation and propagation of phase transformation fronts in a NiTi alloy. *Acta Materialia*, 45(2):683–700, 1997.

[120] H Tobushi, Y Shimeno, T Hachisuka, and K Tanaka. Influence of strain rate on superelastic properties of TiNi shape memory alloy. *Mechanics of Materials*, 30:141–150, 1998.

[121] Y Liu, Y Li, K T Ramesh, and J Van Humbeeck. High strain rate deformation of martensitic NiTi shape memory alloy. *Scripta Materialia*, 41(1):89–95, 1999.

[122] D A Miller and D C Lagoudas. Thermomechanical characterization of NiTiCu and NiTi SMA actuators: influence of plastic strains. *Smart Materials and Structures*, 9:640–652, 2000.

[123] L C Brinson, I Schmidt, and R Lammering. Micro and macromechanical investigations of CuAlNi single crystal and CuAlMnZn polycrystalline shape memory alloys. *Journal of Intelligent Material Systems and Structures*, 13:761–772, 2002.

[124] L C Brinson, I Schmidt, and R Lammering. Stress-induced transformation behavior of a polycrystalline NiTi shape memory alloy: micro and macromechanical investigations via in situ optical microscopy. *Journal of the Mechanics and Physics of Solids*, 52:1549–1571, 2004.

[125] K Otsuka and X Ren. Physical metallurgy of Ti-Ni-based shape memory alloys. *Progress in Materials Science*, 50:511–678, 2005.

[126] P H Leo, T W Shield, and O P Bruno. Transient heat transfer effects on the pseudoelastic behavior of shape-memory wires. *Acta Metallurgica et Materialia*, 41(8):2477–2485, 1993.

[127] S J Plimpton. Fast parallel algorithms for short-range molecular dynamics. *Journal of Computational Physics*, 117:1–19, 1995.

[128] Warp. *http://www.cs.sandia.gov/∼sjplimp/lammps.html*, 2006.

[129] M F Horstemeyer, J C Hamilton, A Thompson, M I Baskes, S J Plimpton, I Daruka, M R Sorenson, A F Voter, D M Ford, P S Rallabandi, and C Tunca. From atom-picoseconds to centimeter-years in simulation and experiment. *Sandia Technical Report*, SAND2001-8111, 2001.

[130] Z Liu, Y Yang, J Liang, Z Hu, S Li, S Peng, and Y Qian. Synthesis of copper nanowires via complex-surfactant-assisted hydrothermal reduction process. *Journal of Physical Chemistry B*, 107:12658–12661, 2003.

[131] M F Horstemeyer, M I Baskes, and S J Plimpton. Length scale and time scale effects on the plastic flow of FCC metals. *Acta Materialia*, 49:4363–4374, 2001.

[132] D L Olmsted, L G Hector, W A Curtin, and R J Clifton. Atomistic simulations of dislocation mobility in Al, Ni, and Al/Mg alloys. *Modelling and Simulation in Materials Science and Engineering*, 13:371–388, 2005.

[133] M P Allen and D J Tildesley. *Computer Simulation of Liquids*. Oxford University Press, 1987.

[134] Andrew Leach. *Molecular modelling: principles and applications*. Pearson Education Limited, 2001.

[135] P Sittner, Y Liu, and V Novak. On the origin of Luders-like deformation of NiTi shape memory alloys. *Journal of the Mechanics and Physics of Solids*, 53:1719–1746, 2005.

[136] U Landman, W D Luedtke, N A Burnham, and R J Colton. Atomistic mechanisms and dynamics of adhesion, nanoindentation, and fracture. *Science*, 248:454–461, 1990.

[137] A S J Koh and H P Lee. Shock-induced localized amorphization in metallic nanorods with strain-rate-dependent characteristics. *Nano Letters*, 6:2260–2267, 2006.

[138] Y Xia, P Yang, Y Sun, Y Wu, B Mayers, B Gates, Y Yin, F Kim, and H Yan. One-dimensional nanostructures: synthesis, characterization, and applications. *Advanced Materials*, 15(5):353–389, 2003.

[139] P L Gai and M A Harmer. Surface atomic defect structures and growth of gold nanorods. *Nano Letters*, 2(7):771–774, 2002.

[140] Y Sun and Y Xia. Alloying and dealloying processes involved in the preparation of metal nanoshells through a galvanic replacement reaction. *Nano Letters*, 3(11):1569–1572, 2003.

[141] Y Sun, B Mayers, T Herricks, and Y Xia. Polyol synthesis of uniform silver nanowires: a plausible growth mechanism and the supporting evidence. *Nano Letters*, 3(7):955–960, 2003.

[142] Y Gao, P Jiang, D F Liu, H J Yuan, X Q Yan, Z P Zhou, J X Wang, L Song, L F Liu, W Y Zhou, G Wang, C Y Wang, and S S Xie. Synthesis, characterization and self-assembly of silver nanowires. *Chemical Physics Letters*, 380:149–149, 2003.

[143] V Rodrigues, T Fuhrer, and D Ugarte. Signature of atomic structure in the quantum conductance of gold nanowires. *Physical Review Letters*, 85(19):4124–4127, 2000.

[144] G E Tommei, F Baletto, R Ferrando, R Spadacini, and A Danani. Energetics of fcc and decahedral nanowires of Ag, Cu, Ni, and C_{60}: a quenched molecular dynamics study. *Physical Review B*, 69:115426, 2004.

[145] K K Caswell, C M Bender, and C J Murphy. Seedless, surfactantless wet chemical synthesis of silver nanowires. *Nano Letters*, 3(5):667–669, 2003.

[146] H Chen, Y Gao, H Zhang, L Liu, H Yu, H Tian, S Xie, and J Li. Transmission-electron-microscopy study on fivefold twinned silver nanowires. *Journal of Physical Chemistry B*, 108:12038–12043, 2004.

[147] W Lee, R Scholz, K Nielsch, and U Gosele. A template based electrochemical method the synthesis of multisegmented metallic nanotubes. *Angew. Chem. Int. Ed.*, 44:6050–6054, 2005.

[148] H J Fan, M Knez, R Scholz, K Nielsch, E Pippel, D Hesse, M Zacharias, and U Gsele. Monocrystalline spinel nanotube fabrication based on the kirkendall effect. *Nature Materials*, 5(8):627, 2006.

[149] K L Kelly, E Coronado, L L Zhao, and G C Schatz. The optical properties of metal nanoparticles: the influence of size, shape, and dielectric environment. *Journal of Physical Chemistry B*, 107:668–677, 2003.

[150] B Wiley, Y Sun, B Mayers, and Y Xia. Shape-controlled synthesis of metal nanostructures: the case of silver. *Chemistry-A European Journal*, 11(2):454–463, 2005.

[151] W M Mook, J J Jungk, M J Cordill, N R Moody, Y Sun, Y Xia, and W W Gerberich. Geometry and surface state effects on the mechanical response of Au nanostructures. *Zeitschrift fur Metallkunde*, 95(6):416–424, 2004.

[152] A M Leach, M McDowell, and K Gall. Deformation of top-down and bottom-up silver nanowires. *Advanced Functional Materials*, 17:43–53, 2007.

[153] J Diao, K Gall, M L Dunn, and J A Zimmerman. Atomistic simulations of the yielding of gold nanowires. *Acta Materialia*, 54:643–653, 2006.

[154] J Diao, K Gall, and M L Dunn. Atomistic simulation of the structure and elastic properties of gold nanowires. *Journal of the Mechanics and Physics of Solids*, 52:1935–1962, 2004.

[155] T Kizuka, Y Takatani, K Asaka, and R Yoshizaki. Measurements of the atomistic mechanics of single crystalline silicon wires of nanometer width. *Physical Review B*, 72:035333, 2005.

[156] Z L Wang, R P Gao, B Nikoobakht, and MA El-Sayed. Surface reconstruction of the unstable {110} surface in gold nanorods. *The Journal of Physical Chemistry B*, 104:5417–5420, 2000.

[157] Y Zhang, A Kolmakov, S Chretien, H Metiu, and M Moskovits. Control of catalytic reactions at the surface of a metal oxide nanowire by manipulating electron density inside it. *Nano Letters*, 4(3):403–407, 2004.

[158] Z Fan, D Wang, P Chang, W Tseng, and J G Liu. Zno nanowire field-effect transistor and oxygen sensing property. *Applied Physics Letters*, 85(24):5923–5925, 2004.

[159] Z Hua, S Yang, H Huang, L Lv, M Lu, B Gu, and Y Du. Metal nanotubes prepared by a sol-gel method followed a hydrogen reduction procedure. *Nanotechnology*, 17:5106–5110, 2006.

[160] C Mu, Y X Yu, R M Wang, K Wu, D S Xu, and G L Guo. Uniform metal nanotube arrays by multistep template replication and electrodeposition. *Advanced Materials*, 16(17):1550–1553, 2004.

[161] J C Bao, C Y Tie, Z Xu, Q F Zhou, D Shen, and Q Ma. Template synthesis of an array of nickel nanotubules and its magnetic behavior. *Advanced Materials*, 13(21):1631, 2001.

[162] W C Yoo and J K Lee. Field-dependent growth patterns of metals electroplated in nanoporous alumina membranes. *Advanced Materials*, 16(13):1097, 2004.

[163] Y C Sui, R Skomski, K D Sorge, and D J Sellmyer. Nanotube magnetism. *Applied Physics Letters*, 84(9):1525–1527, 2004.

[164] Q T Wang, G Z Wang, X H Han, X P Wang, and J G Hou. Controllable template synthesis of ni/cu nanocable and ni nanotube arrays: A one-step coelectrodeposition and electrochemical etching method. *Journal of Physical Chemistry*, 109(49):23326–23329, 2005.

[165] J Zang, M Huang, and F Liu. Mechanism for nanotube formation from self-bending nanofilms driven by atomic-scale surface-stress imbalance. *Physical Review Letters*, 98(14):146102–146105, 2007.

[166] A Ramstad, G Brocks, and P J Kelly. Theoretical study of the Si (100) surface reconstruction. *Physical Review B*, 51(20):14504–14523, 1995.